



Aerodynamic Design and Analysis of a Two Stage to Orbit Winged semi-Reusable Launching Vehicle

Thesis report

Victor Sonneveld

Aerodynamic Design and Analysis of a Two Stage to Orbit Winged semi-Reusable Launching Vehicle

Thesis report

by

Victor Sonneveld

to obtain the degree of Master of Science
at the Delft University of Technology,
to be defended publicly on Friday October 1, 2021 at 13:30.

Student number: 4218426
Project duration: September 19, 2020 – October 1, 2021
Thesis committee: Dr. ir. M. F. M. Hoogreef, TU Delft, Supervisor
Dr. ir. G. la Rocca, TU Delft, Chair
Ir. R. Noomen, TU Delft, Examiner
Ir. T. R. Knop, Dawn Aerospace, Supervisor

This thesis is confidential and cannot be made public until October 1, 2023.

An electronic version of this thesis is available at <http://repository.tudelft.nl/>.

Cover photo credit: SpaceX¹

¹Arevalo, E., *SpaceX sends Dragon on a final mission to the space station and conducts a successful 50th Falcon 9 rocket landing*, The Tesmanian, March 2020, <https://www.tesmanian.com/blogs/tesmanian-blog/spacex-crs-20-50th-falcon>, Date Accessed: 7-1-2021

Preface

Last year September, I started working on this thesis under the supervision of Maurice and Tobi. At the time, it was difficult to find a professor to supervise me, as the university was closed as a result of a lockdown and thus everybody was hidden away in their home office. When I called Maurice to be my supervisor, he never hesitated, and gave me the support I needed throughout the thesis. Tobi provided me the opportunity to work on Dawn Aerospace's spaceplane project, offered all his knowledge on this topic and gave me the space to research a part of it. A big round of applause to Maurice and Tobi.

I would like to thank my parents and sister, for their encouragement and (financial) support, during the entire time of my studies in Delft. I literally could not have done it without you. Thank you to my girlfriend, Roxanne, for your mental support and patience.

During this past year I have had some welcome distraction working with Ralph, Thom, Frederik, Ruben and Quint. I look forward to continue our project with full dedication. My thanks to Niz, an excellent listener to my frustrations on thesis and life in lockdown, and great organizer of Formula 1 parties. Shout-out to Alex, with whom I enjoyed working on the Silverwing and our boat project. In 2012 I started studying Aerospace Engineering and met a group of friends, consisting of Aeilt-Jan, Bart, Benjamin, Floris, Niels and Twan, who pulled me through the BSc phase. After that, we kind of went our separate ways but still had plenty of screw-our-head-off sessions. Also special thanks to my housemates Adriaan and Aegir, who have had to endure me while working on this thesis.

This thesis report marks the end of my time as student, and I am looking forward to new and exciting projects, problems and achievements.

*Victor Sonneveld
Delft, September 2021*

Summary

The commercialization of the space industry has led to a reduction in size and weight of satellites and launching vehicles, which have effectively reduced the cost of space services. The costs of launching these satellites to space can be further reduced, when their launching vehicles are reusable. These vehicles are called semi-Reusable Launching Vehicles (sRLV) and they include various concepts.

As vertical take-off and landings require special infrastructure from space ports, the concept of semi-Reusable Launching Vehicles may be improved by employing a runway for a horizontal take-off and landing. The first stage vehicle, after separating from the second stage, returns to the runway to perform a horizontal landing. This is referred to as a two stage to orbit (TSTO), horizontal take-off horizontal landing (HTHL) launching vehicle. The first stage is a winged vehicle, called a spaceplane, and it features operational flexibility, in the sense that it can be flown from a runway.

Dawn Aerospace is pursuing development of the winged semi-Reusable Launching Vehicle with horizontal take-off and landing capabilities in the Mk-III concept. Before this research, work has been done on a preliminary design study of the Mk-III concept. However, the aerodynamic design has not been addressed in the previous work, and the aerodynamic design and performance of the Orbital Sciences X-34 were assumed for the Mk-III concept.

It is important that the aerodynamic design is already considered in the conceptual design, as the large variations in flight conditions during the mission pose conflicting requirements on the aerodynamic design. The aerodynamic design that would be best for the gliding phase does not necessarily work well for the ascent or re-entry phases.

A performance analysis model of the launching vehicle must be developed, in which the aerodynamic discipline is integrated. This vehicle model must be sensitive to design parameters of the aerodynamic design, such as the wing planform parameters. The development of this integrated aerodynamic model is the goal of the research performed in this thesis.

The performance of the launching vehicle can only be deduced from an analysis of the trajectory to be flown. Therefore, the model is split up in two parts: a vehicle model and a trajectory model.

The vehicle model estimates the characteristics of both stages of the launching vehicle, using a set of input parameters. The launching vehicle experiences three kinds of forces: thrust forces, gravitational forces and aerodynamic forces. Therefore, a propulsion model is necessary to cover the performance of the rocket engines, a mass model estimates the dry mass of the vehicle stages and an aerodynamic model estimates the lift and drag coefficients. The mass model and aerodynamic model require information on the size of the vehicle, which is provided by a geometry model.

The trajectory model receives information on the launching vehicle's characteristics from the vehicle model, in the form of aerodynamic coefficients, masses, and propulsive forces. Using this information, the trajectory model simulates the path that the vehicle travels. Since the vehicle consists of two stages, the trajectory of both stages is simulated.

Using the developed model, sensitivity analyses and case studies were performed to investigate the impact of design changes on the mission performance. These results indicate that the limited gliding range of the first stage vehicle influences the propellant mass fraction of the upper stage through two mechanisms: The gliding range constrains the amount of delta-V delivered by the first stage, and thus the upper stage has to deliver the major part of the orbital velocity. The second mechanism is that the limited gliding range requires a steep ascent trajectory, which inherently results in large gravity losses.

The performed case studies indicate how the propellant mass fraction of the upper stage can be influenced, by changes to the vehicle design. Analysis of an alternative wing concept that improves the gliding performance of the first stage vehicle shows that the propellant mass fraction of the upper stage vehicle can be reduced from 91.5% to 90.3%. This can be achieved as the improved gliding range allows to reduce the delta-V

delivered by the upper stage, and a less steep ascent trajectory that results in 8.9% less gravity losses. Analysis of a changed fuselage configuration indicates a reduction of propellant mass fraction from 91.5% to 90.4%. This was possible due to reduced vehicle dry mass, as a result of the fuselage design change, which increased the effective gliding range for the fact that more altitude was conserved after atmospheric re-entry.

Also changes to the trajectory design were analyzed, and by either reversing the direction of the take-off maneuver or by reserving propellant for the return trajectory, the propellant mass fraction can be reduced. The reductions achieved in the case studies were 0.5% for the reversed take-off direction, and 1.2% for the propelled return trajectory.

Contents

| | |
|--|------|
| Preface | iii |
| Summary | v |
| List of Figures | ix |
| List of Tables | xiii |
| Nomenclature | xv |
| Abbreviations | xix |
| 1 Introduction | 1 |
| 2 Vehicle Model | 5 |
| 2.1 Propulsion | 6 |
| 2.2 Geometry | 7 |
| 2.3 Mass | 8 |
| 2.4 Aerodynamics. | 11 |
| 2.4.1 Subsonic conditions | 11 |
| 2.4.2 Supersonic conditions | 14 |
| 2.5 Vehicle model validation | 18 |
| 2.5.1 Validation of Propulsion Model | 18 |
| 2.5.2 Validation of Mass and Geometry Model. | 19 |
| 2.5.3 Validation of Aerodynamic Model | 22 |
| 3 Trajectory Model | 25 |
| 3.1 First stage trajectory model | 25 |
| 3.1.1 Take-off | 26 |
| 3.1.2 Powered ascent | 26 |
| 3.1.3 Parabolic coast. | 27 |
| 3.1.4 Re-entry | 27 |
| 3.1.5 Turn | 28 |
| 3.1.6 Glideback | 28 |
| 3.1.7 Landing | 29 |
| 3.1.8 Environmental models. | 29 |
| 3.1.9 Velocity losses | 30 |
| 3.2 Upper stage trajectory model | 30 |
| 3.3 Trajectory model validation. | 32 |

| | | |
|-------|--|----|
| 4 | Sensitivity analysis | 37 |
| 4.1 | Baseline design | 37 |
| 4.2 | Sensitivity to planform parameters | 39 |
| 4.2.1 | Wing aspect ratio | 39 |
| 4.2.2 | Wing surface area | 40 |
| 4.2.3 | Leading edge sweep angle | 41 |
| 4.3 | Sensitivity to trajectory parameters | 42 |
| 4.3.1 | Flight path angle at staging. | 42 |
| 4.3.2 | Spaceport location | 43 |
| 4.4 | Sensitivity to model uncertainty | 45 |
| 4.4.1 | Uncertainty in mass model | 45 |
| 4.4.2 | Uncertainty in subsonic drag estimation. | 46 |
| 4.4.3 | Uncertainty in supersonic drag estimation. | 48 |
| 5 | Case studies | 51 |
| 5.1 | Alternative Wing Concept | 51 |
| 5.2 | Alternative Fuselage Concept | 53 |
| 5.3 | Reverse take-off. | 55 |
| 5.4 | Boostback. | 56 |
| 6 | Conclusions and Recommendations | 59 |
| 6.1 | Conclusions. | 59 |
| 6.2 | Recommendations | 60 |
| | Bibliography | 64 |
| A | Aerodynamic validation results | 65 |

List of Figures

| | | |
|------|---|----|
| 1.1 | Side boosters of Falcon Heavy performing vertical landing at Kennedy Space Center [2]. | 1 |
| 1.2 | Photo of the Mk-II aircraft, taken at Wigram Airport | 2 |
| 1.3 | FESTIP Sub-Orbital Hopper Concept [3] | 2 |
| 1.4 | Two stage to orbit concept by Tsuchiya and Mori [4], comparing horizontal and vertical take-off. | 2 |
| 1.5 | X-34 Advanced Technological Demonstrator [6] | 3 |
| 1.6 | Maddock, Ricciardi, West, <i>et al.</i> [5] concept, with internal arrangement. | 3 |
| 1.7 | Operational diagram of two stage to orbit, horizontal take-off and landing launching vehicle, indicating the conflicting aerodynamic designs optimal for the mission segments individually. | 4 |
| 2.1 | Overview of model developed in this research. | 5 |
| 2.2 | Flow chart of vehicle model. | 5 |
| 2.3 | Layout definition of second stage vehicle, used for determining length dimension. | 7 |
| 2.4 | Layout definition of first stage vehicle, used for determining length dimension. | 8 |
| 2.5 | Layout definition of first stage vehicle, with alternative packaging of internal components and second stage vehicle. | 8 |
| 2.6 | Flow diagram indicating the iterative process employed in estimating the vehicle mass. | 9 |
| 2.7 | Simulated velocity profile of Dawn Mk-III concept. | 11 |
| 2.8 | Example of aircraft geometry displayed by OpenVSP. | 12 |
| 2.9 | Scheme with methods employed in aerodynamic model for subsonic speeds. | 13 |
| 2.10 | Scheme with methods employed in aerodynamic model for supersonic speeds. | 14 |
| 2.11 | Example of arrow wing geometry, with "notch" in the planform's trailing edge. Dashed lines illustrate shock waves in supersonic conditions. [18] | 16 |
| 2.12 | Logistic functions used to transition between linear and nonlinear methods over the high-supersonic speed regime. | 17 |
| 2.13 | Comparison of estimated rocket engine mass and validation data. | 19 |
| 2.14 | Comparison of estimated mass of modern rocket engines and validation data. | 19 |
| 2.15 | Mass validation results of conventional launching vehicles. | 20 |
| 2.16 | Length validation results of conventional launching vehicles. | 20 |
| 2.17 | Drag estimation of X-34 at $M = 0.8$, including vortex drag estimation using leading-edge suction analogy. | 22 |
| 2.18 | Wind tunnel model used for obtaining experimental data of Orbital Sciences X-34, attached to the sting at its base [23]. | 22 |
| 2.19 | Lift curves of X-34 at $M = 4$, showing the bridging from the linear arrow wing method to the non-linear Newtonian theory. | 23 |
| 2.20 | Drag curves of X-34 at $M = 6$, showing the bridging from the linear arrow wing method to the non-linear Newtonian theory. | 23 |
| 2.21 | PRORA Unmanned Space Vehicle developed by Italian Aerospace Research Center (CIRA) [25]. | 23 |

| | |
|--|----|
| 2.22 Schlieren image of wind tunnel model of the PRORA-USV. [24] | 23 |
| 2.23 Drag estimation of the Dawn Aerospace Mk-II at $M = 0.14$, including vortex drag estimation using leading-edge suction analogy. | 24 |
| 2.24 Components of supersonic zero-lift drag of the Dawn Aerospace Mk-II. | 24 |
| 3.1 Schematic of take-off maneuver, comprising of ground run and aerial phase. | 26 |
| 3.2 Angle of attack profile during take-off maneuver. | 26 |
| 3.3 Illustration of angle of attack vs. time (left) and flight path angle vs. time (right) used to model first stage ascent segment. | 27 |
| 3.4 Profile of angle of attack and stagnation point heat flux vs. time. Phases of re-entry segment are indicated in graphs (1, 2, 3). | 28 |
| 3.5 Simulated altitude vs. downrange profile of Dawn Mk-III concept, shown as an example of the oscillating gliding motion. | 29 |
| 3.6 Angle of attack profile during landing segment, indicating ground run and aerial phase. | 29 |
| 3.7 Velocity triangles used as relation between inertial orbital velocity and delta-V to be delivered by launching vehicle. | 31 |
| 3.8 Illustration indicating the importance of flight path angle parameter at the begin of the upper stage burn. | 32 |
| 3.9 Illustration of angle of attack profile that must be specified for upper stage trajectory. | 32 |
| 3.10 Comparison of altitude over time between the simulated result, the Maddock et al. validation case, and the Haex validation case. | 34 |
| 3.11 Comparison of velocity over time between the simulated result, the Maddock et al. validation case, and the Haex validation case. | 34 |
| 3.12 Comparison of altitude versus downrange between the simulated result, the Maddock et al. validation case, and the Haex validation case. | 35 |
| 4.1 Simulated first and upper stage trajectories of the baseline design, in altitude vs. time. | 38 |
| 4.2 Simulated first and upper stage trajectories of the baseline design, in velocity vs. time. | 38 |
| 4.3 Simulated first stage trajectories of the baseline design, in altitude vs. downrange. | 39 |
| 4.4 Angle of attack profile applied to upper stage trajectory. | 39 |
| 4.5 Altitude vs. time for four different values of wing aspect ratio. | 39 |
| 4.6 Velocity vs. time for four different values of wing aspect ratio. | 39 |
| 4.7 Velocity vs. time for four different values of wing aspect ratio. | 40 |
| 4.8 Delta-V budget of first stage vehicle for four different values of wing aspect ratio. | 40 |
| 4.9 Altitude vs. time for three different values of wing surface area. | 40 |
| 4.10 Velocity vs. time for three different values of wing surface area. | 40 |
| 4.11 Velocity vs. time for three different values of wing surface area. | 41 |
| 4.12 Delta-V budget of first stage vehicle for three different values of wing surface area. | 41 |
| 4.13 Altitude vs. time for three different values of sweep angle. | 41 |
| 4.14 Velocity vs. time for three different values of sweep angle. | 41 |
| 4.15 Velocity vs. time for three different values of sweep angle. | 42 |
| 4.16 Delta-V budget of first stage vehicle for three different values of sweep angle. | 42 |
| 4.17 Altitude vs. time for three different values of staging flight path angle. | 43 |

| | | |
|------|--|----|
| 4.18 | Velocity vs. time for three different values of staging flight path angle. | 43 |
| 4.19 | Delta-V budget of upper stage vehicle for three different values of staging flight path angle. | 43 |
| 4.20 | Altitude vs. time for five different spaceport locations. | 44 |
| 4.21 | Velocity vs. time for five different spaceport locations. | 44 |
| 4.22 | Velocity vs. time for five different spaceport locations. | 44 |
| 4.23 | Delta-V budget of upper stage vehicle for five different spaceport locations. | 44 |
| 4.24 | Altitude vs. time for variations of first stage dry mass. | 46 |
| 4.25 | Velocity vs. time for variations of first stage dry mass. | 46 |
| 4.26 | Altitude vs. downrange for variations of first stage dry mass. | 46 |
| 4.27 | Altitude vs. time for variations of upper stage dry mass. | 46 |
| 4.28 | Velocity vs. time for variations of upper stage dry mass. | 46 |
| 4.29 | Altitude vs. downrange for variations of upper stage dry mass. | 46 |
| 4.30 | Altitude vs. time for variations of subsonic zero-lift drag coefficient. | 47 |
| 4.31 | Velocity vs. time for variation of subsonic zero-lift drag coefficient. | 47 |
| 4.32 | Altitude vs. downrange for variation of subsonic zero-lift drag coefficient. | 47 |
| 4.33 | Altitude vs. time for variation of subsonic lift-induced drag. | 47 |
| 4.34 | Velocity vs. time for variation of subsonic lift-induced drag. | 47 |
| 4.35 | Altitude vs. downrange for variation of subsonic lift-induced drag. | 47 |
| 4.36 | Altitude vs. time for variations of supersonic zero-lift drag coefficient. | 48 |
| 4.37 | Velocity vs. time for variation of supersonic zero-lift drag coefficient. | 48 |
| 4.38 | Altitude vs. time for variation of supersonic lift-induced drag. | 48 |
| 4.39 | Velocity vs. time for variation of supersonic lift-induced drag. | 48 |
| 4.40 | Altitude vs. downrange for variation of supersonic zero-lift drag coefficient. | 49 |
| 4.41 | Altitude vs. downrange for variation of supersonic lift-induced drag. | 49 |
| | | |
| 5.1 | Wing planform of baseline design | 52 |
| 5.2 | Wing planform of alternative design | 52 |
| 5.3 | Altitude vs. time of alternative wing concept. | 52 |
| 5.4 | Velocity vs. time of alternative wing concept. | 53 |
| 5.5 | Altitude vs. downrange of alternative wing concept. | 53 |
| 5.6 | First stage Delta-V budget of alternative wing concept. | 53 |
| 5.7 | Upper stage Delta-V budget of alternative wing concept. | 53 |
| 5.8 | Altitude vs. time of parallel fuselage concept. | 54 |
| 5.9 | Velocity vs. time of parallel fuselage concept. | 54 |
| 5.10 | Altitude vs. downrange of parallel fuselage concept. | 54 |
| 5.11 | First stage Delta-V budget of parallel fuselage concept. | 55 |
| 5.12 | Upper stage Delta-V budget of parallel fuselage concept. | 55 |
| 5.13 | Altitude vs. downrange of reverse take-off concept. | 55 |
| 5.14 | Altitude vs. time of reverse take-off concept. | 56 |
| 5.15 | Velocity vs. time of reverse take-off concept. | 56 |

| | | |
|------|--|----|
| 5.16 | First stage Delta-V budget of reverse take-off concept. | 56 |
| 5.17 | Upper stage Delta-V budget of reverse take-off concept. | 56 |
| 5.18 | Altitude vs. time of boostback concept. | 57 |
| 5.19 | Velocity vs. time of boostback concept. | 57 |
| 5.20 | Altitude vs. downrange of boostback concept. | 57 |
| 5.21 | Velocity vs. time of first stage vehicle of boostback concept. | 57 |
| 5.22 | First stage Delta-V budget of boostback concept. | 58 |
| 5.23 | Upper stage Delta-V budget of boostback concept. | 58 |
| | | |
| A.1 | Aerodynamic model validation results of the Orbital Sciences X-34 lift coefficients. | 65 |
| A.2 | Aerodynamic model validation results of the Orbital Sciences X-34 drag coefficients. | 66 |
| A.3 | Aerodynamic model validation results of the PRORA-USV lift coefficients. | 67 |
| A.4 | Aerodynamic model validation results of the PRORA-USV drag coefficients. | 67 |
| A.5 | Aerodynamic model validation results of the Dawn Aerospace Mk-II lift coefficients. | 68 |
| A.6 | Aerodynamic model validation results of the Dawn Aerospace Mk-II drag coefficients. | 68 |

List of Tables

| | | |
|-----|--|----|
| 2.1 | Components of first and upper stages, used for vehicle dry mass estimation. | 9 |
| 2.2 | Results of propulsion model validation analysis | 18 |
| 2.3 | Statistical parameters of propulsion model validation, including values after correction. | 18 |
| 2.4 | Validation data and model results of rocket engine mass and lengths. | 19 |
| 2.5 | Statistical parameters of rocket engine mass and length validation. | 19 |
| 2.6 | Statistical parameters of launch vehicle stage mass and length validation | 20 |
| 2.7 | Validation data and model results of airplane elements masses | 20 |
| 2.8 | Statistical parameters of airplane elements mass validation | 20 |
| 2.9 | Estimated and validation mass data of North American X-15 aircraft. | 21 |
| 3.1 | Comparison of the vehicle characteristics of the Maddock, Toso, Ricciardi, <i>et al.</i> [29] study and results of the vehicle model, used for the trajectory validation case. | 33 |
| 3.2 | Orbit and trajectory parameters used as inputs for the trajectory model. | 33 |
| 4.1 | Vehicle design and trajectory parameters of the baseline design. | 38 |
| 4.2 | Delta-V budget of first stage vehicle for four different values of wing aspect ratio. | 40 |
| 4.3 | Delta-V budget of first stage vehicle for three different values of wing surface area | 41 |
| 4.4 | Delta-V budget of first stage vehicle for three different values of sweep angle | 42 |
| 4.5 | Delta-V budget of upper stage vehicle for three different values of staging flight path angle | 43 |
| 4.6 | Spaceport locations used in sensitivity analysis. | 43 |
| 4.7 | Delta-V budget of upper stage vehicle for five different spaceport locations. | 44 |
| 5.1 | Mass distribution of alternative wing concept. | 52 |
| 5.2 | Mass distribution of parallel fuselage concept. | 54 |
| 5.3 | Mass distribution of reverse take-off concept. | 55 |
| 5.4 | Mass distribution of boostback concept. | 57 |

Nomenclature

Greek Symbols

| | | |
|----------------|--|-----------------------------------|
| α | Angle of attack | [°] |
| α_T | Thrust vector angle of attack | [°] |
| β_0 | Launch azimuth angle | [°] |
| $\beta_{0,i}$ | Inertial launch azimuth angle | [°] |
| η | Location of airfoil's maximum thickness | [-] |
| Γ | Vandenkerckhove parameter | [-] |
| γ | Flight path angle | [°] |
| γ_c | Specific heat ratio of combustion gasses | [-] |
| λ | Latitude angle | [°] |
| λ | Wing taper ratio | [-] |
| Λ_{LE} | Leading edge sweep angle | [°] |
| Λ_{TE} | Trailing edge sweep angle | [°] |
| μ | Roll angle | [°] |
| μ_b | Braking frictional coefficient | [-] |
| μ_g | Standard gravitational parameter | [m ³ /s ²] |
| ω_E | Earth angular velocity | [rad/s] |
| ω_E | Orbit angular velocity | [rad/s] |
| ϕ | Bank angle | [°] |
| ρ | Air density | [kg/m ³] |
| ρ_f | Fuel density | [kg/m ³] |
| ρ_{ox} | Oxidizer density | [kg/m ³] |
| $\vec{\Omega}$ | Earth rotation vector | [rad/s] |
| ξ | Notch ratio of arrow wing | [-] |
| ζ_F | Thrust quality factor | [-] |

Roman Symbols

| | | |
|---------------|------------------------------------|---------------------|
| \dot{m} | Engine mass flow | [kg/s] |
| A | Wing aspect ratio | [-] |
| a | Semi-major axis | [m] |
| a_c | Coriolis acceleration | [m/s ²] |
| A_e | Engine exit area | [m ²] |
| A_t | Engine throat area | [m ²] |
| A_v | Vertical tail aspect ratio | [-] |
| b_v | Vertical tail span | [m] |
| c | Chord length | [m] |
| c^* | Engine characteristic velocity | [m/s] |
| C_D | Drag coefficient | [-] |
| C_F | Engine thrust coefficient | [-] |
| C_L | Lift coefficient | [-] |
| c_n | Normal section chord length | [m] |
| C_t | Airfoil section thrust coefficient | [-] |
| C_{D_0} | Zero-lift drag coefficient | [-] |
| C_{D_f} | Frictional drag coefficient | [-] |
| C_{D_g} | Drag coefficient on runway | [-] |
| C_{D_i} | Induced drag coefficient | [-] |
| $C_{D_{0,w}}$ | Zero-lift wave drag coefficient | [-] |
| $C_{L_{LOF}}$ | Lift coefficient at lift-off | [-] |
| $C_{p,lim}$ | Pressure coefficient limit | [-] |

| | | |
|----------------|---|--------------------------------------|
| $C_{t,n}$ | Normal section thrust coefficient | [-] |
| D | Drag force | [N] |
| d | Distance from leading edge | [m] |
| D_b | Braking force | [N] |
| D_e | Engine exit diameter | [m] |
| D_{fus} | Fuselage diameter | [m] |
| F_T | Engine thrust force | [N] |
| g | Gravitational acceleration | [m/s ²] |
| g_0 | Gravitational acceleration at sea level | [m/s ²] |
| g_w | Ratio of wall temperature | [-] |
| h | Altitude | [m] |
| i | Orbit inclination angle | [°] |
| I_{sp} | Specific impulse | [s] |
| J_2 | Orbit perturbation due to oblateness of Earth | [-] |
| K_T | Fraction of leading edge suction | [-] |
| L | Lift force | [N] |
| l | length | [m] |
| L/D | Lift to Drag ratio | [-] |
| M | Mach number | [-] |
| m | Leading-edge flow parameter | [-] |
| M_e | Equivalent Mach number | [-] |
| M_f | Fuel mass | [kg] |
| M_m | Mean molar mass | [g · mol ⁻¹] |
| M_n | Mach number normal to leading edge | [-] |
| m_p | Payload mass | [kg] |
| $m_{avionics}$ | Avionics mass | [kg] |
| m_{eng} | Engine mass | [kg] |
| M_{ox} | Oxidizer mass | [kg] |
| m_{pla} | Payload adapter mass | [kg] |
| m_{pres} | Pressurant mass | [kg] |
| m_{str} | Engine thrust structure mass | [kg] |
| m_{tank} | Tank mass | [kg] |
| m_{TO_2} | Second stage vehicle take-off mass | [kg] |
| m_{TO} | Maximum take-off mass | [kg] |
| m_{valves} | Mass of valves | [kg] |
| n | Load factor | [-] |
| n_{ult} | Ultimate load factor | [-] |
| p_a | Ambient pressure | [Pa] |
| p_c | Combustion chamber pressure | [Pa] |
| p_e | Engine exit pressure | [Pa] |
| q_L | Dive dynamic pressure | [Pa] |
| $q_{c,FP}$ | Flat plate stagnation point heat flux | [W/m ²] |
| $q_{c,s}$ | Stagnation point heat flux | [W/m ²] |
| q_{LE} | Leading edge heat flux | [W/m ²] |
| R | Range | [m] |
| r | Leading edge radius | [m] |
| R^* | Universal gas constant | [mol ⁻¹ K ⁻¹] |
| R_E | Radius of Earth | [m] |
| R_n | Nose radius | [m] |
| r_n | Normal section leading edge radius | [m] |
| R_{turn} | Turning radius | [m] |
| RC | Rate of Climb | [m/s] |
| Re | Reynolds number | [-] |
| Re_n | Normal section Reynolds number | [-] |
| S | Wing surface area | [m ²] |
| s | Distance | [m] |

| | | |
|------------|---|-------------------|
| S_r | Rudder surface area | [m ²] |
| S_v | Vertical tail surface area | [m ²] |
| T | Thrust force | [N] |
| t/c | Airfoil thickness to chord ratio | [-] |
| T_c | Combustion chamber temperature | [K] |
| t_n/c_n | Normal section thickness to chord ratio | [-] |
| t_{rv} | Root thickness of vertical tail | [m] |
| V | Velocity | [m/s] |
| V_E | Velocity due to Earth's rotation | [m/s] |
| V_e | Velocity in eastern direction | [m/s] |
| V_f | Fuel volume | [m ³] |
| V_n | Velocity in northern direction | [m/s] |
| V_R | Aircraft's real internal volume | [m ³] |
| V_u | Velocity in upwards direction | [m/s] |
| V_{LOF} | Velocity at lift-off | [m/s] |
| $V_{O,i}$ | Inertial orbital velocity | [m/s] |
| V_{ox} | Oxidizer volume | [m ³] |
| V_{SH} | Volume of Sears-Haack body | [m ³] |
| V_{tank} | Tank volume | [m ³] |
| W_{fus} | Fuselage structural weight | [N] |
| W_{LG} | Landing gear weight | [N] |
| W_{TO} | Maximum take-off weight | [N] |
| W_{VT} | Vertical tail weight | [N] |
| W_{wing} | Wing structural weight | [N] |
| X | Input factor | [-] |
| Y | Performance response | [-] |

Abbreviations

| | |
|------|--|
| CFD | Computational Fluid Dynamics |
| HTHL | Horizontal Take-off and Horizontal Landing |
| LEO | Low Earth Orbit |
| SG | Sub-goal |
| SQ | Sub-question |
| sRLV | semi-Reusable Launching Vehicle |
| SSO | Sun-Synchronous Orbit |
| SSTO | Single Stage to Orbit |
| TPS | Thermal Protection System |
| TSTO | Two Stage to Orbit |
| VLM | Vortex Lattice Method |
| VTHL | Vertical Take-off and Horizontal Landing |

1

Introduction

Satellites play important roles in our daily lives. They provide communication, navigation, weather forecast, tools to research climate change and to respond to natural disaster. Historically, the development of these space applications were carried out by government funded organizations. Over the past decade this has changed to the current situation, where privately held companies fulfill the development of not only satellites, but also the launching vehicles. This commercialization of the space industry has led to a reduction in size and weight of satellites and launching vehicles, which have effectively reduced the cost of space services.

The costs of launching these satellites to space can be further reduced, when their launching vehicles are reusable[1]. These vehicles are called semi-Reusable Launching Vehicles (sRLV) and they include various concepts. One of these concepts is the Falcon 9 or Heavy system by SpaceX, which is a Two Stage to Orbit (TSTO) launching vehicle, famous for its vertical landing of the first stage vehicle on either land or a ship (Figure 1.1).



Figure 1.1: Side boosters of Falcon Heavy performing vertical landing at Kennedy Space Center [2].

As vertical take-off and landings require special infrastructure from space ports, the concept of semi-Reusable Launching Vehicles may be improved by employing a runway for a horizontal take-off and landing. The first stage vehicle, after separating from the second stage, returns back to the runway to perform a horizontal landing. This is referred to as a two stage to orbit (TSTO), horizontal take-off horizontal landing (HTHL) launching vehicle. The first stage is a winged vehicle, called a spaceplane, and it features operational flexibility, in the sense that it can be flown from a runway.

A company that aims to exploit the TSTO, HTHL concept is Dawn Aerospace, whose mission is to provide a

cost-effective and frequently available solution for small satellite launching. The first stage vehicle launches an upper stage at roughly 100 km altitude, which continues the ascent to deliver the payload to space. The first stage is the reusable part of the launching vehicle and returns to the same runway for landing.

Dawn Aerospace is based in Delft, The Netherlands and in Christchurch, New Zealand and already has established itself in the space industry as a producer of propulsion systems for cubesats and small satellites. In parallel to this, the company is developing the technology required for the spaceplane concept, such as the rocket propulsion system, and building scale models to demonstrate the technological readiness. The latest of these models is the Mk-II aircraft, shown in Figure 1.2, intended to prove the sub-orbital flight capabilities. The successor of the Mk-II aircraft is the Mk-III, which is intended as the vehicle that actually takes payload to orbit, as a TSTO HTHL launching vehicle.



Figure 1.2: Photo of the Mk-II aircraft, taken at Wigram Airport

Similar to the Dawn Aerospace Mk-III concept, the FESTIP Hopper was researched at the end of last century[3]. Although its payload capability was a lot larger at 7000 kg, it also featured two stages to orbit, with only the first stage reusable. A major difference is that the landing is not performed at the same runway as the take-off. The FESTIP concept is shown in Fig. 1.3, and it has an interesting way of packaging the upper stage inside the first stage vehicle. By placing the upper stage on top of the propellant tanks of the first stage, a shorter fuselage is achieved, and the upper stage can be released in flight by simply sliding out the back of the vehicle.

Another study performed in Japan by [4], revolved around a two stage to orbit system, with the take-off and landing performed at the same location[4]. In the study, a comparison was made between horizontal and vertical take-offs, and the conclusion was drawn that a horizontal take-off yielded a heavier vehicle, as the landing gear should then also be sized for the take-off weight, which is much greater with all the propellant still present. However, they did recognize that a horizontal take-off can be chosen for criteria other than weight, such as operability and reliability.

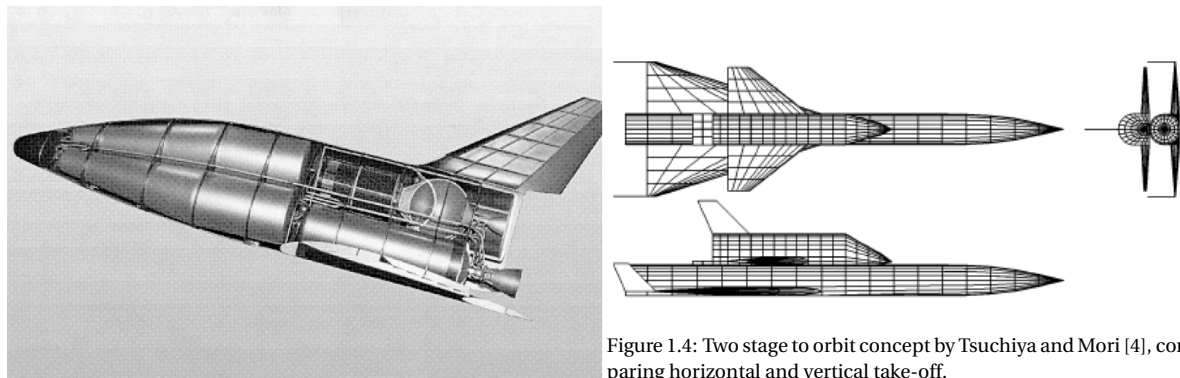


Figure 1.4: Two stage to orbit concept by Tsuchiya and Mori [4], comparing horizontal and vertical take-off.

Figure 1.3: FESTIP Sub-Orbital Hopper Concept [3]

In the USA, the X-34 Advanced Technological Demonstrator project was pursued in an attempt to reduce launch costs. While the first stage vehicle was reusable, it was launched from a carrier aircraft. The vehicle was actually built, but unfortunately it never made it to flight as the program was ended due to exceeding project costs. The interesting thing about the X-34 is that the aerodynamic design is adopted in a number

of other studies. One of these is the concept of Maddock, Ricciardi, West, *et al.* [5], which features a payload capability of 500kg to low earth orbit (LEO). Shown in Figure 1.6, the upper stage is positioned in the middle of the first stage vehicle fuselage, in contrast to the FESTIP vehicle. This results in a longer fuselage, and the structure needs to accommodate the release of the upper stage from the middle of the fuselage, rather than simply sliding out the back.



Figure 1.5: X-34 Advanced Technological Demonstrator [6]

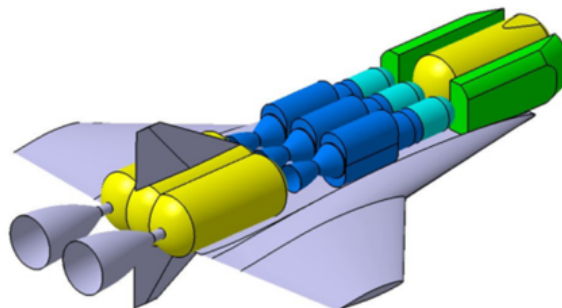


Figure 1.6: Maddock, Ricciardi, West, *et al.* [5] concept, with internal arrangement.

Previous to this study, work has been done on a preliminary design study of the Dawn Aerospace Mk-III concept [7], for which a multi-disciplinary analysis optimization tool was developed to size the first and upper stage of the vehicle. Interestingly, the objective of the optimization was to reduce the cost of the vehicle and of the operation. Different methods to return the first stage vehicle back to the take-off runway were already compared, as well as sensitivity analyses to payload mass and orbit altitude. However, the aerodynamic design has not been addressed in the previous analyses and optimizations and the aerodynamic design and performance of the X-34 were assumed for the Mk-III concept.

It is important that the aerodynamic design is already considered in the conceptual design, as the large variations in flight conditions during the mission pose conflicting requirements on the aerodynamic design, which can be explained as follows. The first stage vehicle must bring the upper stage vehicle to a velocity and altitude, from which the upper stage can ascend further to orbit. While the ascent of the upper stage occurs outside of the atmosphere, the first stage vehicle must traverse the atmosphere. For this reason, the drag of the first stage should be as low as possible as to minimize aerodynamic losses. Increased aerodynamic losses mean that more propellant is required, ultimately leading to a heavier vehicle. As the first stage re-enters the atmosphere, the vehicle must slow down as much as possible before reaching the denser layers of the atmosphere, for which a high drag is required, which is in contrast to the low drag required for the ascent. After re-entry, the first stage must glide back to the take-off and landing runway. For gliding performance a high aerodynamic efficiency, i.e. a high lift to drag ratio, is required. The aerodynamic design that would be best for the gliding phase does not necessarily work well for the ascent or re-entry phases.

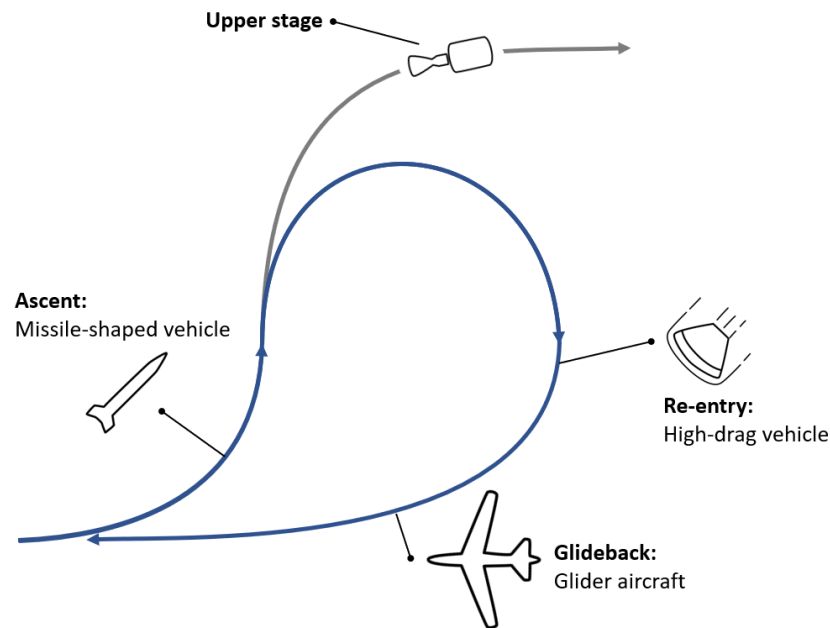


Figure 1.7: Operational diagram of two stage to orbit, horizontal take-off and landing launching vehicle, indicating the conflicting aerodynamic designs optimal for the mission segments individually.

The aerodynamic design is thus driven by these conflicting requirements, and from previous studies on similar vehicles, or on the Dawn Mk-III concept itself, it has not been determined what the best aerodynamic design is. To be able to do this, a performance analysis model of the launching vehicle must be developed, in which the aerodynamic discipline is integrated. This vehicle model must be sensitive to design parameters of the aerodynamic design, such as the wing planform parameters. The development of this integrated aerodynamic model is the goal of the research performed in this thesis, and is summarized in the following Research Objective.

Research Objective: *To develop an integrated aerodynamic model for a reusable launching vehicle, sensitive to wing planform parameters, to identify areas in the vehicle design that have a significant impact on the mission performance.*

In order to achieve this objective, the following Primary Research Question is formulated, further broken down in two Sub Questions (SQ):

Primary Research Question: *What is the performance and design impact of wing planform changes to a reusable launch vehicle with horizontal take-off and landing capability?*

SQ 1: *What areas in the vehicle design have a significant impact on the mission performance?*

SQ 2: *How does the trajectory design impact the mission performance?*

The structure of this thesis report is as follows: The methodology used in developing the analysis model of the launching vehicle, with integrated aerodynamic discipline, is explained in Chapter 2. The mission performance of the launching vehicle cannot be deduced without simulating the trajectory. Chapter 3 discusses the method employed in developing the trajectory model. After the the vehicle and trajectory models were developed and validated, a sensitivity analysis was performed of the input parameters of the vehicle and trajectory design. Furthermore, to find areas in the vehicle design that have an impact on the mission performance, a number of case studies were performed and explained in Chapter 5. Finally, conclusions that were drawn from the research performed on the reusable launching vehicle are listed and discussed in Chapter 6.

2

Vehicle Model

To achieve the objective of this thesis research, a model has to be developed to analyze the performance of a reusable launching vehicle. The performance of the launching vehicle can only be deduced with an analysis of the trajectory to be flown. The model is thus split up in two parts: a vehicle model and a trajectory model.

The vehicle model estimates the characteristics of both stages of the launching vehicle, using a set of input parameters. The resulting vehicle characteristics are fed to the trajectory model, which simulates the motion of the launching vehicle from take-off to landing, and to orbit. The overall model developed for this research is graphically described in Figure 2.1. The methodology for the vehicle model is presented in this chapter, while Chapter 3 discusses the development of the trajectory model.

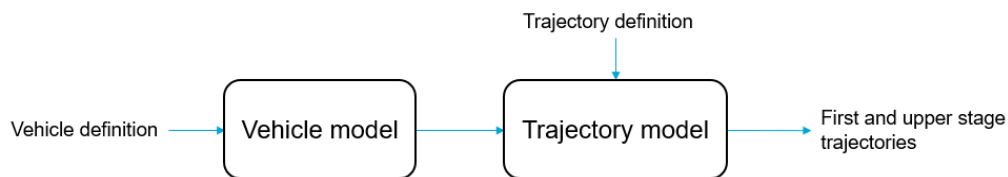


Figure 2.1: Overview of model developed in this research.

The launching vehicle experiences three kinds of forces: thrust forces, gravitational forces and aerodynamic forces. Therefore, a propulsion model is necessary to cover the performance of the rocket engines, a mass model estimates the dry mass of the vehicle stages and an aerodynamic model estimates the lift and drag coefficients. The mass model and aerodynamic model require information on the size of the vehicle, which is provided by a geometry model. In the vehicle model, these models are executed consecutively, with information produced in one model, fed into the next. This process is illustrated in Fig. 2.2. The individual parts of the vehicle model were constructed using the methods explained in Sections 2.1 to 2.4. After construction, the vehicle model was validated as discussed in Section 2.5.

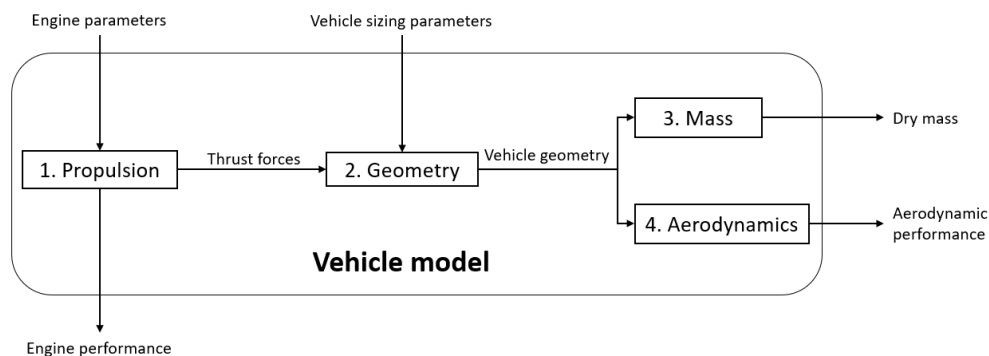


Figure 2.2: Flow chart of vehicle model.

2.1. Propulsion

The approach to modelling the vehicle propulsion is based on the method used in Haex [7], where the performance of the rocket engine is calculated using Ideal Rocket Theory. This method provides a set of equations to estimate the thrust F_T and the specific impulse I_{sp} , using three input parameters: The engine mass flow \dot{m} , the engine exit diameter D_e and the combustion chamber pressure p_c .

A simple equation to describe the thrust of a rocket engine is given as follows:

$$F_T = \dot{m} I_{sp} g_0 \quad (2.1)$$

This equation relates thrust to the mass flow \dot{m} , which is also a factor influencing the engine's mass, and the specific impulse I_{sp} . This specific impulse can be related to the thrust coefficient C_F and the characteristic velocity c^* , in Equation 2.2.

$$I_{sp} = \frac{C_F \cdot c^*}{g_0} \quad (2.2)$$

The characteristic velocity can be computed based on the thermo-chemistry of the oxidizer and fuel mixture, using Eq. 2.3. In this equation, Γ is the Vandekerckhove parameter (defined in Eq. 2.4, R^* is the universal gas constant, M_m is the mean molar mass of the combustion gasses, γ_c the specific heat ratio of the combustion gasses and T_c is the temperature in the combustion chamber. The thermo-chemistry parameters γ_c , M_m and T_c are computed using the Chemical Equilibrium Applications code developed by NASA [8].

$$c^* = \frac{1}{\Gamma} \sqrt{\frac{R^*}{M_m} T_c} \quad (2.3)$$

$$\Gamma(\gamma_c) = \sqrt{\gamma_c \cdot \left(\frac{1 + \gamma_c}{2}\right)^{\frac{1 + \gamma_c}{1 - \gamma_c}}} \quad (2.4)$$

The characteristic velocity can also be related to the combustion chamber pressure p_c and the throat area A_t . With Eq. 2.5, the throat area can now be computed.

$$c^* = \frac{p_c A_t}{\dot{m}} \quad (2.5)$$

Now, with the the following function, relating the area and pressure at the throat and exit, the exit pressure can be calculated:

$$\frac{A_e}{A_t} = \frac{\Gamma}{\sqrt{\frac{2\gamma_c}{\gamma_c - 1} \left(\frac{p_e}{p_c}\right)^{\frac{2}{\gamma_c}} \left(1 - \left(\frac{p_e}{p_c}\right)^{\frac{\gamma_c - 1}{\gamma_c}}\right)}} \quad (2.6)$$

With the exit pressure known, the thrust coefficient can be calculated, using Equation 2.7, where p_a is the ambient pressure. This thrust coefficient can then be entered in Eq. 2.2 to estimate the specific impulse and consequently the engine thrust force F_T .

$$C_F = \Gamma \sqrt{\frac{2\gamma_c}{\gamma_c - 1} \left(1 - \left(\frac{p_e}{p_c}\right)^{\frac{\gamma_c - 1}{\gamma_c}}\right)} + \left(\frac{p_e}{p_c} - \frac{p_a}{p_c}\right) \frac{A_e}{A_t} \quad (2.7)$$

The method explained in this section assumes ideal conditions, whereas in reality also losses occur, reducing the achieved thrust and specific impulse. The amount of losses can be quantified in a thrust quality factor ζ_F , as defined in Equation 2.8.

$$\zeta_F = \frac{F_{T,actual}}{F_{T,real}} = \frac{I_{sp,actual}}{I_{sp,real}} \quad (2.8)$$

2.2. Geometry

The task of the geometry module is to determine the size of the first stage fuselage and the upper stage vehicle, which sits inside the first stage fuselage. This process requires some input parameters of the propellant masses of both stages, and the diameter of the first stage fuselage D_{fus} . Using these, the length of the vehicle can be determined.

Starting with the second stage vehicle, the lay-out as shown in Fig. 2.3 is used. The total length of the second stage vehicle l_{st_2} is the sum of the engine length l_{eng_2} , the oxidizer tank length l_{ox_2} , the fuel tank length l_{fuel_2} and the length of the payload l_p .

$$l_{st_2} = l_{eng_2} + l_{ox_2} + l_{fuel_2} + l_p \quad (2.9)$$

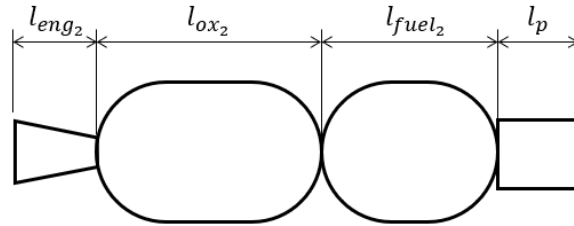


Figure 2.3: Layout definition of second stage vehicle, used for determining length dimension.

For the propellant tanks, the shapes of either cylinders with spherical end caps are assumed, or pure spherical tanks if they fit within the fuselage diameter D_{fus} . First, the volume of the propellant is calculated with their densities, using Eq. 2.10 and 2.11.

$$V_{fuel_2} = M_{fuel_2} \cdot \rho_{fuel} \quad (2.10)$$

$$V_{ox_2} = M_{ox_2} \cdot \rho_{ox} \quad (2.11)$$

Using the geometric relation for the volume of a cylindrical tank with spherical end caps, the length of the fuel and oxidizer tanks can be found:

$$V_{f_2} = \frac{1}{6}\pi D_{fus}^3 + \frac{1}{4}\pi D_{fus}^2 (l_{fuel_2} - D_{fus}) \quad (2.12)$$

$$V_{ox_2} = \frac{1}{6}\pi D_{fus}^3 + \frac{1}{4}\pi D_{fus}^2 (l_{ox_2} - D_{fus}) \quad (2.13)$$

For the length of the engine, a relation from [9] is taken, relating the engine length to the second stage thrust force F_{T_2} (valid for thrust forces between 15 kN and 8000 kN).

$$l_{eng_2} = 0.1362 F_{T_2}^{0.2279} \quad (2.14)$$

The payload mass dimensions are based on the ESPA standards [10] for a 250 kg payload. This specifies a box with a base of 24 times 28 In, and a length of 38 In or 0.97 m.

For the first stage vehicle, the lay-out of Figure 2.4 is used. Of course, the elements can be arranged in a different order, but this does not affect the total first stage length l_{st_1} , defined by Eq. 2.15.

$$l_{st_1} = l_{eng_1} + l_{ox_1} + l_{fuel_1} + l_{st_2} + l_{nose} \quad (2.15)$$

The length of the first stage engine is calculated in the same way as for the second stage (Eq. 2.14, based on its thrust force F_{T_1}). The methods for the upper stage oxidizer and fuel tanks also apply for the first stage tanks (Eq. 2.10 to 2.13, based on the first stage oxidizer mass M_{ox_1} and fuel mass M_{fuel_1}). Finally, the nose is

approximated using a tangent ogive shape with rounded tip. Its length is derived from the X-34 aircraft's nose length to fuselage diameter ratio l_{nose}/D_{fus} of 1.4.

$$l_{nose} = \frac{l_{nose}}{D_{fus}} D_{fus} \quad (2.16)$$

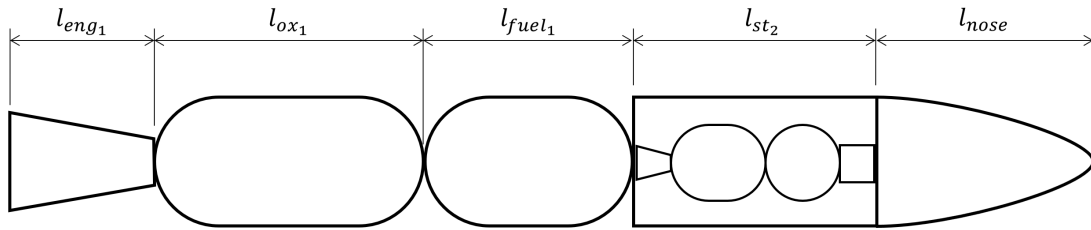


Figure 2.4: Layout definition of first stage vehicle, used for determining length dimension.

Alternatively, the upper stage vehicle and the components of the first stage vehicle can be packaged in different configurations. One such configuration that will be investigated as a case study in Sec. 5.2, and is inspired by the design of the FESTIP study, shown in Figure 1.3. In this alternative fuselage design the upper stage vehicle is packaged on top of the fuel tank of the first stage vehicle, and this configuration may have certain benefits, such as lower wetted surface area, smaller shift of center of gravity during operation and possibly a more simple method of stage separation. To be able to analyze this alternative configuration, the geometry model must also be able to determine the size of this design. An example of the layout, used to construct the geometry model for this alternative design, is shown in Figure 2.5.

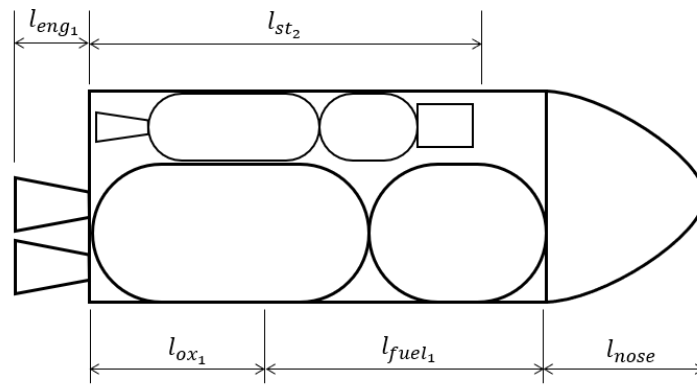


Figure 2.5: Layout definition of first stage vehicle, with alternative packaging of internal components and second stage vehicle.

2.3. Mass

The Mass module is the part of the vehicle model that calculates the dry mass of the first and second stage vehicle, by estimating the masses of their components. The components that build up the total dry mass of the first and upper stage are listed in Table 2.1. The estimation relations for these component masses depend on the total vehicle mass (including the vehicle dry mass), and thus the vehicle dry mass must be calculated in an iterative manner, as described by the diagram of Figure 2.6.

Table 2.1: Components of first and upper stages, used for vehicle dry mass estimation.

| First stage | Upper stage |
|-------------------------|-------------------------|
| Rocket engine | Rocket engine |
| Thrust structure | Thrust structure |
| Fuel tank | Fuel tank |
| Oxidizer tank | Oxidizer tank |
| Tank thermal protection | Tank thermal protection |
| Intertank structure | Intertank structure |
| Pressurant tanks | Pressurant tanks |
| Valves | Valves |
| Avionics | Avionics |
| Electrical power system | Electrical power system |
| Payload bay | Payload adapter |
| Fuselage | |
| Wing | |
| Vertical tail | |
| Landing gear | |

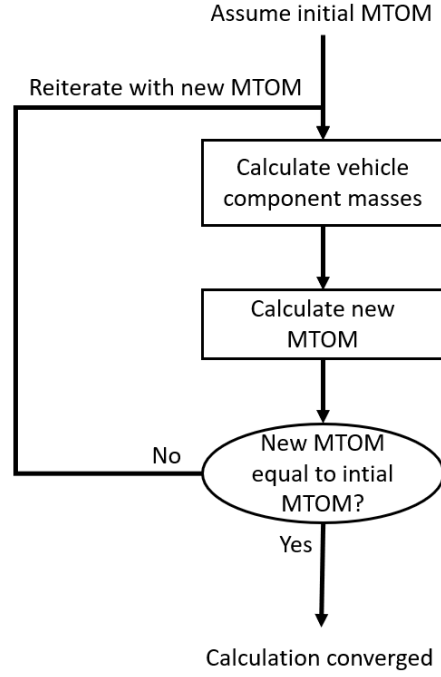


Figure 2.6: Flow diagram indicating the iterative process employed in estimating the vehicle mass.

The engine mass of a kerosene fueled system can be calculated as a function of engine thrust with the following equation, derived by Zandbergen [9]. This engine mass also includes the turbo-pumps group, the propellant feed system and some miscellaneous items.

$$m_{eng} = 1.104 \cdot 10^{-3} F_T + 27.702 \quad (2.17)$$

The thrust structure transfers the engine's thrust to the vehicle's structural frame. Its mass can be estimated using a simple relation, also based on the engine thrust [11].

$$m_{str} = 2.55 \cdot 10^{-4} F_T \quad (2.18)$$

The oxidizer tank and fuel tank masses are estimated as a function of their content's volume (in m^3) and composition [11]:

$$m_{tank} = \begin{cases} 9.09 V_{tank} & \text{if LH2} \\ 12.16 V_{tank} & \text{otherwise} \end{cases} \quad (2.19)$$

If the tanks are to operate at cryogenic temperatures, e.g. with liquid oxygen, thermal protection needs to be applied. The mass of this system is a function of the type of propellant stored in the tank, and can be calculated with Eq. 2.20 [12].

$$m_{TPS,tank} = \begin{cases} 0.9765 (\pi D_{tank} L_{tank} + \pi D_{tank}^2) & \text{if LOx} \\ 1.2695 (\pi D_{tank} L_{tank} + \pi D_{tank}^2) & \text{if LH2} \\ 0 & \text{otherwise} \end{cases} \quad (2.20)$$

The intertank structure connects the oxidizer and fuel tank and its mass can be calculated using Eq. 2.21 [12].

$$m_{inter} = \begin{cases} 5.4015 \pi D_{tank}^2 \cdot (3.2808 D_{tank})^{0.5169} & \text{for first stage} \\ 3.8664 \pi D_{tank}^2 \cdot (3.2808 D_{tank})^{0.6025} & \text{for upper stage} \end{cases} \quad (2.21)$$

Even though the engine is pump-fed, still the propellant tanks need to be pressurized as they are drawn empty. This is usually done by using some pressurant gas, like helium or nitrogen. When the propellant tank is empty, the pressurant has filled the tank volume V_t completely at the same pressure as the initial propellant tank pressure p_t . The mass of the pressurant can then be calculated using Eq. 2.22 [13]. In this equation R_{pres} is the gas constant of the pressurant gas (usually nitrogen or helium), and $T_{pres,1}$ and p_{pres} are the initial temperature and pressure of the pressurant before expansion from the pressurant tank to the propellant tank pressure.

$$m_{pres} = \frac{V_t p_t}{R_{pres} T_{pres,1}} \left(\frac{\gamma_{pres}}{1 - \frac{p_t}{p_{pres}}} \right) \quad (2.22)$$

The volume of the pressurant tank can then be calculated as in Eq. 2.23. The mass of the pressurant tank is found by entering this volume in Eq. 2.24 [11].

$$V_{pres} = \frac{R_{pres} T_{pres,1}}{p_{pres}} m_{pres} \quad (2.23)$$

$$m_{tank,pres} = 115.3 V_{pres} + 3 \quad (2.24)$$

The mass of the valves of the second stage can be estimated using a relationship from Schlingloff [14], based on the engine thrust and chamber pressure.

$$m_{valves} = 0.02 \left(\frac{F_T \cdot p_c}{1000} \right)^{0.71} \quad (2.25)$$

The avionics and electrical power system masses can be estimated using the relations in Eq. 2.26 and Eq. 2.27 from Castellini [12].

$$m_{avionics} = 0.25 \cdot (246.76 + 1.3183 \cdot D_{fus} \cdot L_{fus}) \quad (2.26)$$

$$m_{EPS} = 0.3321 \cdot m_{avionics} \quad (2.27)$$

Finally, the mass of the payload adapter must be estimated, using a function of payload mass m_p [12].

$$m_{pla} = 0.00478 m_p^{1.013} \quad (2.28)$$

The first stage vehicle endures dynamic pressures similar to fighter airplanes, and is likely to have low aspect ratio wings with high sweep angle. Therefore, for the remaining items, a Class II Method is used from Roskam [15], applicable to Fighter and Attack Airplanes. The following expression gives the weight of the wing in lbs, based on the geometric parameters of the wing and the maximum take-off weight W_{TO} of the first stage aircraft. In this equation, λ is the the wing's taper ratio, A is the aspect ratio, S is the wing area in ft, Λ_{LE} is the leading edge sweep angle, t/c is the thickness to chord ratio and n_{ult} is the ultimate load factor.

$$W_{wing} = 3.08 \left[\frac{n_{ult} W_{TO}}{t/c} \left(\left(\tan \Lambda_{LE} - \frac{2(1-\lambda)}{A(1+\lambda)} \right)^2 + 1 \right) \cdot 10^{-6} \right]^{0.593} \cdot (A(1+\lambda))^{0.89} S^{0.741} \quad (2.29)$$

The weight of the fuselage is given by Equation 2.30, which introduces the design dive dynamic pressure q_L . This can be estimated from reference trajectory analyses. Also of note is the fuselage length to diameter ratio l_{st1}/D_{fus} driving the fuselage weight.

$$W_{fus} = 11.03 \left(\frac{q_L}{100} \right)^{0.245} \left(\frac{W_{TO}}{1000} \right)^{0.98} \left(\frac{l_{st1}}{D_{fus}} \right)^{0.61} \quad (2.30)$$

The aircraft's vertical tail is estimated as a function of its surface area S_v in ft^2 , the distance between the quarter chord points of the wing and tail l_v in ft, the ratio of rudder to tail area S_r/S_v , the tail aspect ratio A_v , taper ratio λ_v and the quarter chord sweep angle $\Lambda_{v1/4c}$

$$W_{VT} = 0.19 \left[(W_{TO} \cdot n_{ult})^{0.363} \cdot S_v^{1.089} \cdot M_H^{0.601} \cdot l_v^{-0.726} \left(1 + \frac{S_r}{S_v} \right)^{0.217} A_v^{0.337} (1 + \lambda_v)^{0.363} (\cos \Lambda_{v1/4c})^{-0.484} \right]^{1.014} \quad (2.31)$$

Finally, the landing gear is a function of the aircraft maximum take-off weight only:

$$W_{LG} = 129.1 \left(\frac{W_{TO}}{1000} \right)^{0.66} \quad (2.32)$$

2.4. Aerodynamics

The goal of the aerodynamic module is to provide a parametric model to estimate the lift and drag coefficients, using the airplane's geometry as input. This is only required for the first stage vehicle, as it traverses the atmosphere with the upper stage stored internally and it is assumed that the trajectory of the upper stage is completely outside of the atmosphere. The first stage vehicle experiences a wide range of speeds throughout its mission, reaching into the supersonic domain. The estimated lift and drag coefficients are thus also a function of Mach Number. Since most existing analysis methods are only applicable for a certain range of Mach number, different methods have to be combined.

Although the first stage aircraft experiences subsonic, transonic and supersonic conditions, it should be noted that relative importance between the speed regimes exists. Subsonic conditions occur during the initial part of the ascent segment, and the gliding segment. Supersonic conditions are present in the ascent and re-entry segment. As indicated by Figure 2.7, the transonic speed regime occurs only for a very short time (in a number of seconds) compared to the full duration of the mission, during the ascent and the re-entry. Therefore, the developed aerodynamic model consists of a subsonic part ($M < 1.0$) and a supersonic part ($M > 1.0$) with no correction made for the transonic part.

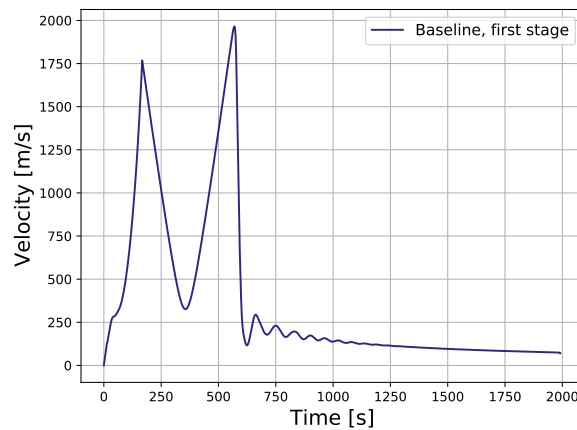


Figure 2.7: Simulated velocity profile of Dawn Mk-III concept.

2.4.1. Subsonic conditions

For the subsonic domain, the lift and drag coefficients versus angle of attack must be estimated at Mach numbers ranging from zero up to sonic conditions. The aerodynamic analysis tool VSPAERO features the capabilities to perform these estimations with only a few minutes of calculation time. VSPAERO is an analysis extension of OpenVSP, in which an aircraft geometry can be created. Using a Python script and a spreadsheet of geometric parameters, the geometry in OpenVSP is generated, containing a fuselage body, wing and tailplane. An example geometry generated with this script and displayed by OpenVSP is shown in Fig. 2.8.

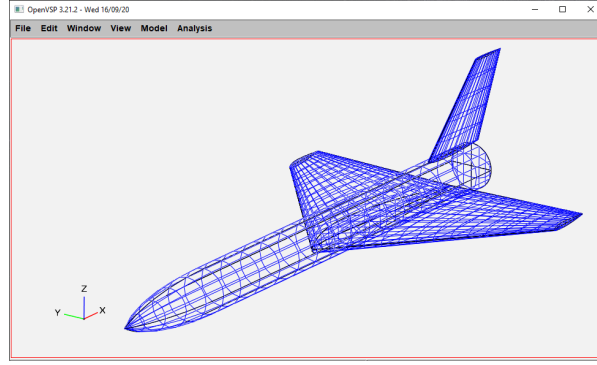


Figure 2.8: Example of aircraft geometry displayed by OpenVSP.

VSPAERO uses a vortex lattice method to estimate the lift of the airplane geometry, for a given angle of attack and Mach number. The drag coefficient C_D , as defined in Eq. 2.33, consists of a zero-lift component C_{D_0} and a lift-induced component C_{D_i} . The zero-lift drag coefficient is calculated as function of the user-specified Reynolds number. OpenVSP also has a Parasite Drag Tool with advanced options and capabilities to estimate the zero-lift drag. In this work however, the default method of VSPAERO was found to give acceptable results. The induced drag coefficient also comes from the vortex lattice solver of VSPAERO, but a second order Karman-Tsien Mach correction accounts for compressibility effects at higher (subsonic) Mach numbers.

$$C_D = C_{D_0} + C_{D_i} \quad (2.33)$$

Wings with large sweep angles form a stable vortex over its leading edge at high angles of attack. This vortex influences the drag of the wing significantly. Using the vortex-lattice method of VSPAERO it is not possible to estimate the vortex drag. To be able estimate the aircraft's drag, including the vortex drag, the equation of 2.33 must be modified to the form of Equation 2.34. In this equation, the term $C_{D_{i,max}}$ is the maximum induced drag value possible, and its definition is given in Equation 2.35 [16].

$$C_D = C_{D_0} + K_T \cdot C_{D_{i,p}} + (1 - K_T) \cdot C_{D_{i,max}} \quad (2.34)$$

$$C_{D_{i,max}} = C_L \tan \alpha \quad (2.35)$$

The minimum induced drag value is given by potential lift theory, as calculated by VSPAERO. The actual value of induced drag that a wing experiences is usually lower than the maximum value, which means that there is a suction force present acting against this drag. The amount of drag that the wing experiences in presence of vortex drag is dependent on the amount of leading-edge suction that is achieved. The parameter K_T is the fraction of leading edge thrust (1 for 100% leading-edge suction and 0 for 0%), and from this it can be inferred where in between the lower and upper limit the experienced induced drag lies. When full leading-edge suction is achieved, the drag coefficient definition from Equation 2.34 is reduced to Equation 2.33.

To include the effect of vortex drag in the aerodynamic model, the value of K_T thus must be obtained. This is done using the method described by Carlson, Mack, and Barger [17]. The method, called the leading-edge suction analogy in this research, estimates the amount of leading-edge suction that can be achieved, based on the flow conditions (Mach number, Reynolds number, angle of attack) and on the wing's geometrical properties, such as the leading-edge's sweep angle and radius, the airfoil's thickness and the chordwise location of this thickness. Thus, for a given wing planform with defined airfoil sections, the fraction of leading-edge suction K_T is calculated for a range of Mach numbers and angles of attack. The method of estimation is explained in the following paragraphs.

First, the Mach number of the flow normal to the leading edge M_n is calculated with the following Equation:

$$M_n = M \cos \Lambda_{LE} \quad (2.36)$$

Then, for each spanwise section of the wing, the normal section chord length c_n as a ratio of the section's

chord c is calculated using Equation 2.37. In this equation, η is the location of the airfoil's maximum thickness, expressed as fraction of the chord.

$$\frac{c_n}{c} = \frac{2\eta}{\sin \Lambda_{LE} [(1-\eta) \tan \Lambda_{LE} + \eta \tan \Lambda_{TE}] + \cos \Lambda_{LE}} \quad (2.37)$$

Also the normal section thickness-to-chord ratio t_n/c_n is calculated, dependent on the streamwise thickness-to-chord ratio t/c , as in Equation 2.38. Also the section's leading edge radius r_n is computed using Eq. 2.39.

$$\frac{t_n}{c_n} = \frac{t}{c} \frac{1}{2\eta \cos \Lambda_{LE}} \quad (2.38)$$

$$\frac{r_n}{c_n} = \frac{r}{c} \frac{1}{2\eta \cos^2 \Lambda_{LE}} \quad (2.39)$$

The section's thrust coefficient C_t , is taken as the theoretical two-dimensional value, defined as in Eq. 2.40. This is dependent on the normal flow Mach number M_n and the angle of attack. With this thrust coefficient of the streamwise section, Equation 2.41 the thrust coefficient of the normal section $C_{t,n}$ can be estimated:

$$C_t = \frac{2\pi\alpha^2}{\sqrt{1-M_n^2}} \quad (2.40)$$

$$\frac{C_{t,n}}{C_t} = \frac{c}{c_n} \frac{1}{\cos^2 \Lambda_{LE}} \quad (2.41)$$

Then a Reynolds number of the flow normal to the leading edge Re_n is estimated with Eq. 2.42, and this corresponds to a limiting pressure coefficient $C_{p,lim}$. This allows for calculation of the equivalent Mach number, needed for the calculation of the fraction of leading edge suction K_T , by solving Equation 2.44 for M_e .

$$Re_n = Re \frac{c_n}{c} \cos \Lambda_{LE} \quad (2.42)$$

$$C_{p,lim} = \frac{-2}{\gamma M_n^2} \left[\frac{R_n \cdot 10^{-6}}{R_n \cdot 10^{-6} + 10^{(4-3M_n)^2}} \right]^{0.05+0.35(1-M_n)^2} \quad (2.43)$$

$$\frac{-2}{\gamma M_e^2} = C_{p,lim} \frac{\sqrt{1-M_n^2}}{\sqrt{1-M_e^2}} \quad (2.44)$$

Finally, the amount leading edge suction as a fraction K_T can be calculated with Equation 2.45. If the calculated value of K_T exceeds 1, simply a value of 1 is taken, as this corresponds to 100% suction.

$$K_T = \frac{2(1-M_e^2)}{M_e} \left[\frac{\frac{t_n}{c_n} \left(\frac{r_n}{c_n}\right)^{0.4}}{c_{t,n} \sqrt{1-M_n^2}} \right]^{0.6} \quad (2.45)$$

To summarize the methods used for the subsonic aerodynamic model, the scheme of Fig. 2.9 is provided.

| Mach range | Lift | Drag | | |
|------------|---------|----------------|-------------------|------------------------------|
| | | Zero-lift drag | Lift-induced drag | Vortex drag |
| $M < 1$ | VSPAERO | VSPAERO | | Leading-edge suction analogy |

Figure 2.9: Scheme with methods employed in aerodynamic model for subsonic speeds.

2.4.2. Supersonic conditions

In supersonic conditions, the estimation of the lift and drag coefficient becomes more challenging. This is because two factors contributing to the zero-lift drag become significant, namely the wave drag due to volume and the base drag, and secondly, because it was found that also in supersonic conditions a distinction must be made in regimes of speed or Mach number. The regimes that were used in the supersonic aerodynamic model are low-supersonic ($1 < M < 3$), high-supersonic ($3 < M < 5$) and hypersonic ($M > 5$). An overview of the methods used for the supersonic aerodynamic model is given in Figure 2.10, and they will be explained in further detail in the rest of this subsection.

| Mach range | Lift | Drag | | | | |
|-------------|---------------------------|---------------|-----------------------------|-----------------------|---------------------------|------------------------------|
| | | Friction drag | Zero-lift drag | | Lift-induced drag | Vortex drag |
| | | | Wave drag | Base drag | | |
| $1 < M < 3$ | Arrow-wing method | VSPAERO | Equivalent Sears-Haack body | Analytical expression | Arrow-wing method | Leading-edge suction analogy |
| $3 < M < 5$ | Bridged method | | | | Bridged method | |
| $M > 5$ | Modified Newtonian theory | | | | Modified Newtonian theory | |

Figure 2.10: Scheme with methods employed in aerodynamic model for supersonic speeds.

The drag coefficient of the aircraft in supersonic conditions is the sum of the zero-lift drag C_{D_0} and lift induced drag C_{D_i} , as in Eq. 2.46. The estimation of zero-lift drag C_{D_0} in supersonic conditions includes the frictional drag component C_{D_f} , the zero-lift wave drag component $C_{D_{0,w}}$, and the base drag component $C_{D_{base}}$, as given in Eq. 2.47.

$$C_D = C_{D_0} + C_{D_i} \quad (2.46)$$

$$C_{D_0} = C_{D_f} + C_{D_{0,w}} + C_{D_{base}} \quad (2.47)$$

The frictional drag C_{D_f} is assumed to be constant with Mach number and subsequently calculated using the subsonic analysis method of VSPAERO. Although in reality at high Mach numbers the frictional drag coefficient decreases with Mach number due to kinetic heating of the boundary layer [18], it was found that this did not provide a significantly better estimation of the zero-lift drag. As can be seen in the validation of the aerodynamic model in Section 2.5, there is room for improvement in the supersonic zero-lift drag modelling and since a more detailed method for the frictional drag did not decrease the discrepancies it was chosen to use the more simple method, constant with Mach number.

To get an accurate estimate of the zero-lift wave drag, a detailed aircraft geometry is required, which is often not available in conceptual design and thus also not available in this research. Therefore, other methods have been considered that can handle different aircraft geometries. The first one that was considered is the linearized area rule, in which the cross-sectional area distribution in streamwise direction yields the wave drag due to volume. This method is a built-in feature of VSPAERO, which intersects the defined geometry with planes inclined at the Mach angle, and was therefore easy to implement. It was however experienced, that it does not provide a meaningful tool for conceptual design, for two reasons. The first being that the resulting wave drag coefficient is greatly influenced by the amount of planes used to intersect the aircraft geometry, which is a setting of the analysis. Increasing the amount of planes did cause the result to converge, but to an excessively high value. This can be explained by the fact that the simplified aircraft geometry is not smoothed or optimized for low drag and thus contains certain jumps in the geometry, e.g. at the transition

from fuselage to wing. With a low number of intersecting planes, these jumps tend to blend away, while with a high number of planes, these jumps amplify the wave drag.

The second reason is that at high Mach numbers the zero-lift wave drag was underestimated, while at low Mach numbers it was greatly overestimated. It is unclear what caused this behavior, and whether it may be in part due to the same sensitivity to the intersection parameters. The Wave Drag module of VSPAERO thus did not provide a robust method for estimating the zero-lift wave drag.

Instead, the zero-lift wave drag (or wave drag due to volume) was estimated using a method derived for axis-symmetric bodies, for which analytical expressions for the wave drag exist. This sort of body is called the Sears-Haack body, which is a smooth geometry from nose to tail. This method estimates the zero-lift wave drag using Eq. 2.48 [19]. In this equation, $M_{C_{D0,max}}$ is the Mach number at which the zero-lift wave drag is maximum, calculated using equation 2.49. The cross-sectional area to length ratio $\frac{A}{L}$ is taken as the average of the cross-sectional area distribution over the total length of the aircraft. The wave drag efficiency parameter E_{WD} indicates how close an aircraft's wave drag value is to a Sears-Haack body with equivalent area distribution. Its value was estimated using the ratio of the real aircraft's internal volume V_R over the volume of the equivalent Sears-Haack body V_{SH} , which is defined in Equation 2.51. In summary, the volume and cross-sectional area distribution of the aircraft geometry is used to estimate the wave drag due to volume, which was used for all defined supersonic speed regimes.

$$C_{D_w} = \frac{4.5\pi}{S_{ref}} \left(\frac{A}{L}\right)^2 \cdot E_{WD} (0.74 + 0.37 \cos \Lambda_{LE}) \cdot \left(1 - 0.3 \sqrt{M - M_{C_{D0,max}}}\right) \quad (2.48)$$

$$M_{C_{D0,max}} = \frac{1}{(\cos \Lambda_{LE})^{0.2}} \quad (2.49)$$

$$E_{WD} = \frac{V_R}{V_{SH}} \quad (2.50)$$

$$V_{SH} = \frac{3\pi}{16} A_{max} L \quad (2.51)$$

The final contributor to the supersonic zero-lift drag is the base drag, which stems from the fact that a rocket-propelled vehicle usually has a flat base on which the engines are mounted. The base drag is caused by a reduced pressure on the base, which is also dependent on the Mach number and expressed as pressure coefficient, shown in Equation 2.52 [18].

$$C_{P_{base}} = \frac{2}{\gamma M^2} \left(\frac{p_{base}}{p_\infty} - 1 \right) \quad (2.52)$$

For estimation of the aircraft's lift and lift-induced drag in low-supersonic conditions, an analytical method was used for arrow-wings. These sort of wings have straight leading and trailing edges and tips ending in points. The arrow wing is similar to the delta wings often used in supersonic aircraft, although for practicality the wing tips are often cropped and the planform may consist out of spanwise section with variations of leading and trailing edge sweep angles. To be able to use the methods for arrow wings on a wings with these planform variations, an equivalent arrow wing planform is constructed.

An example of an arrow-wing is shown in Figure 2.11. An important parameter defining the arrow wing planform is the so-called notch ratio ξ , being the ratio of the streamwise length of the trailing edge l_n over the total streamwise length of the wing l_w , as in Eq. 2.53. For an arrow wing with unswept trailing edge, the notch ratio ξ reduces to zero.

$$\xi = \frac{l_n}{l_w} = \frac{b_w \tan \Lambda_{TE}}{2l_w} \quad (2.53)$$

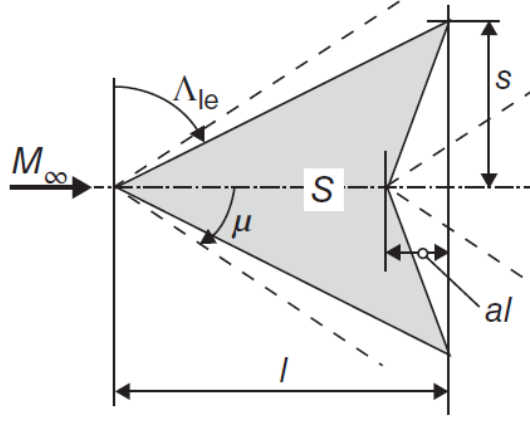


Figure 2.11: Example of arrow wing geometry, with "notch" in the planform's trailing edge. Dashed lines illustrate shock waves in supersonic conditions. [18]

Although the streamwise flow is supersonic, the leading-edge of the wing may be swept to such a degree that it is within the Mach cone formed at the wing-root apex. In this case the flow perpendicular to the leading-edge is subsonic. In determining the lift and drag using the arrow wing method, a distinction is made between the case where the leading-edge is subsonic and the case with supersonic leading-edge. This distinction is made with the parameter m , as defined in Equation 2.54. A subsonic leading-edge is indicated by $m < 1$ and a supersonic leading edge by $m > 1$. The lift curve slope for subsonic and supersonic leading edges are presented in Equation 2.55 [20]. The term $E'(m)$ in this equation is the complete elliptical integral of the second kind with modulus $\sqrt{1-m^2}$. Assuming that at zero angle of attack the lift equals zero, the lift coefficient is found by simply multiplying the lift curve slope by the angle of attack, as in Eq. 2.56.

$$m = \beta \cot \Lambda_{LE} = \sqrt{M^2 - 1} \cdot \cot \Lambda_{LE} \quad (2.54)$$

$$C_{L_\alpha} = \begin{cases} \frac{4m}{\beta E'(m)} \left[\frac{\xi}{1+\xi} + \frac{1-\xi}{(1-\xi^2)^{\frac{3}{2}}} \cos^{-1}(-\xi) \right] & \text{for } m \leq 1 \\ \frac{8m}{\beta\pi(1+\xi)} \left[\frac{1}{\sqrt{m^2-\xi^2}} \cos^{-1}\left(-\frac{\xi}{m}\right) + \frac{\xi}{\sqrt{m^2-1}} \cos^{-1}\frac{1}{m} \right] & \text{for } m \geq 1 \end{cases} \quad (2.55)$$

$$C_L = C_{L_\alpha} \alpha \quad (2.56)$$

The induced drag of the arrow wing is dependent on the amount of leading-edge suction that can be achieved. In general it can be said that a sharp leading edge does not develop suction and as such the induced drag is higher than for a blunt or rounded leading edge. The analysis method for arrow wings produces values for the induced drag coefficient in the case of full leading-edge suction $C_{D_{i,100\%}}$ and in case of zero suction $C_{D_{i,0\%}}$, as given by Equations 2.57 and 2.58. The parameter K_T averages between these two values, as defined in Equation 2.59. If the leading-edge is supersonic, then no suction can be achieved and then the parameters $C_{D_{i,100\%}}$ and K_T reduce to zero.

$$C_{D_{i,100\%}} = \begin{cases} C_L \cdot \alpha - \alpha^2 \frac{\pi m}{\beta(1-\xi)} \frac{\sqrt{1-m^2}}{E'(m)^2} & \text{for } m \leq 1 \\ 0 & \text{for } m \geq 1 \end{cases} \quad (2.57)$$

$$C_{D_{i,0\%}} = C_L \cdot \alpha \quad (2.58)$$

$$C_{D_i} = K_T \cdot C_{D_{i,100\%}} + (1 - K_T) \cdot C_{D_{i,0\%}} \quad (2.59)$$

To estimate the amount of leading-edge suction, quantified in the factor K_T , the same method is used as described for the subsonic aerodynamic model [17] as already explained in Subsection 2.4.1.

For very high Mach numbers, reaching into the hypersonic regime, it was observed from experimental data of the X-34 aircraft that the lift curve becomes nonlinear. To model the lift and the lift-induced drag at these high Mach numbers, a different method was employed, called Modified Newtonian Theory. This method provides two simple expressions for the lift and lift-induced drag coefficients, which are inherently nonlinear with respect to the angle of attack, as shown in Equations 2.60 and 2.61. The parameter $C_{P_{max}}$, the maximum value of pressure coefficient, at the stagnation point behind a normal shock, is evaluated using Equation 2.62, which makes the estimation dependent on the Mach number.

$$C_{L_{Newton}} = C_{P_{max}} \sin^2 \alpha \cos \alpha \quad (2.60)$$

$$C_{D_{i,Newton}} = C_{P_{max}} \sin^3 \alpha \quad (2.61)$$

$$C_{P_{max}} = \frac{2}{\gamma M^2} \left(\left[\frac{(\gamma + 1)^2 M^2}{4\gamma M^2 - 2(\gamma - 1)} \right]^{\frac{\gamma}{\gamma - 1}} \left[\frac{1 - \gamma + 2\gamma M^2}{\gamma + 1} \right] - 1 \right) \quad (2.62)$$

These expressions provide a simple method to evaluate the lift and lift-induced drag at hypersonic Mach numbers. However, it was observed that the lift curve transitions from a linear relation (w.r.t. angle of attack) to this nonlinear relation over a range of Mach numbers between 3 and 7. A method was employed to bridge between the Arrow-wing method at low-supersonic speeds to the Newtonian theory used at hypersonic speeds. The bridging between these methods was performed using two Mach number dependent logistic functions, inspired by the method of transitioning from subsonic to supersonic estimation methods employed in Krus and Abdallah [21].

The logistic functions are defined as in Equation 2.63 and 2.64, where the factors k_N and k_A control the steepness of the curves, and M_{mid} is the Mach number at which the logistic function is 0.5. Through comparison with experimental data, the values of k_N and k_A were estimated at 4 and 2, respectively, with $M_{mid,N}$ and $M_{mid,A}$ set to 4 and 5. The logistic functions are plotted over the range of high-supersonic Mach numbers in Figure 2.12. Equations 2.65 and 2.66 were used to bridge the lift and drag coefficients between the linear arrow-wing method and the Newtonian law, using the logistic functions.

$$f_N(M) = \frac{1}{1 + e^{-k_N(M - M_{mid,N})}} \quad (2.63)$$

$$f_A(M) = 1 - \frac{1}{1 + e^{-k_A(M - M_{mid,A})}} \quad (2.64)$$

$$C_L = f_A \cdot C_{L_{Arrow}} + f_N \cdot C_{L_{Newton}} \quad (2.65)$$

$$C_{D_i} = f_A \cdot C_{D_{i,Arrow}} + f_N \cdot C_{D_{i,Newton}} \quad (2.66)$$

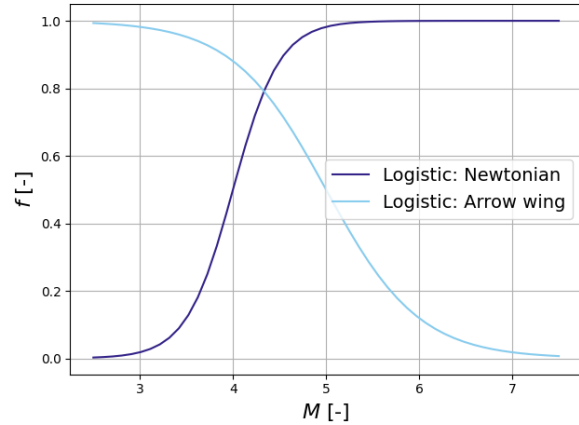


Figure 2.12: Logistic functions used to transition between linear and nonlinear methods over the high-supersonic speed regime.

As can be seen from the graph, the lift and drag from the arrow-wing method is phased out more slowly than the Newtonian method comes into effect. At certain Mach numbers, there are thus two different methods in effect that calculate the lift and drag coefficients and it was observed that this gave the closest approximation to validation data. However, there is no solid physical reasoning behind the determination of the logistic functions' parameters and it should be stated that the bridging between the linear and nonlinear estimation methods deserves more attention. This was left for future research, given the limited time available for this thesis.

One way of looking at this matter is by considering the fact that the Newtonian impact theory calculates lift and drag forces purely from pressure, as if there is a vacuum on the suction side of the body. The linear airfoil method is based on pressure distributions on both the pressure and the suction side of the body. It may be that the suction effect decreases with Mach number more slowly, than that the pressure effect begins to have an effect. It must be emphasized that this is merely philosophical reasoning of the author, without a fundamental understanding of the physical phenomenon, and that more research must be performed on this particular subject to ensure that the developed aerodynamic model is applicable to any aircraft shape.

2.5. Vehicle model validation

Once the vehicle model is developed, validation is necessary to ensure that the results are trustworthy and that the conclusions drawn from these results have any merit. The validation of the vehicle model was done on three parts separately. The propulsion and aerodynamic models were validated individually in Subsections 2.5.1 and 2.5.3. The vehicle mass and geometry models were validated together, as they are constructed using very similar mass and size estimating relations (as described in Sections 2.2 and 2.3), and this is presented in Subsection 2.5.2.

2.5.1. Validation of Propulsion Model

To assess the validity of the propulsion model, the thrust and specific impulse of 7 liquid-propellant rocket engines were estimated and compared to reported values, both in vacuum and in sea level conditions. Because the engine for the Dawn Mk-III vehicle is expected to use kerosene and hydrogen peroxide as propellants, only kerosene fueled engines were included in this analysis, while also liquid oxygen (LOx) as oxidizer was accepted for only one dataset of hydrogen peroxide could be found. The total thrust of the Dawn Mk-III concept is expected to be more similar to the smaller of the 7 validation rocket engines, but since the propulsion model is applicable to any engine size, as the physical principles of rocket engines are the same, also larger rocket engines were included in the validation process. The results of this analysis are summarized in Table 2.2.

The discrepancies between estimated and actual values of individual engines were summarized in statistical parameters, given in Table 2.3. It can be seen that there is good agreement between estimated and actual values of thrust and specific impulse. In general, the estimated values are a bit lower than the real values, which was expected because of the losses in the system. To account for these losses, a thrust quality factor ζ_F of 0.93 was chosen as correction, which minimizes the mean absolute error between the estimated and actual values, which can be seen in the right hand side of Table 2.3.

Table 2.2: Results of propulsion model validation analysis

| Engine | Fuel | Oxidizer | Actual values | | | | Estimated values | | | |
|-----------|------|----------|---------------------|--------------------|---------------------|--------------------|---------------------|--------------------|---------------------|--------------------|
| | | | $F_{T,vac}$ [kN] | $F_{T,SL}$ [kN] | $I_{sp,vac}$ [s] | $I_{sp,SL}$ [s] | $F_{T,vac}$ [kN] | $F_{T,SL}$ [kN] | $I_{sp,vac}$ [s] | $I_{sp,SL}$ [s] |
| Gamma8 | RP-1 | H2O2 | 234.8 | 222.4 | 265.0 | 251.0 | 234.9 | 222.5 | 265.2 | 251.2 |
| Merlin-1D | RP-1 | LOX | 742.4 | 654.3 | 320.0 | 282.0 | 794.8 | 703.6 | 342.5 | 303.2 |
| H-1 | RP-1 | LOX | 947.7 | 836.2 | 289.0 | 255.0 | 1032.6 | 921.0 | 315.0 | 281.0 |
| H-1B | RP-1 | LOX | 1030.2 | 911.9 | 296.0 | 262.0 | 1114.0 | 995.8 | 320.2 | 286.2 |
| RD-120 | RP-1 | LOX | 912.0 | | 350.0 | | 981.9 | | 376.9 | |
| RD191 | RP-1 | LOX | 2090.0 | 1920.0 | 337.5 | 311.2 | 2302.5 | 1951.5 | 371.9 | 315.2 |
| YF100 | RP-1 | LOX | 1339.0 | 1199.0 | 335.0 | 300.0 | 1419.9 | 1277.5 | 355.4 | 319.7 |

Table 2.3: Statistical parameters of propulsion model validation, including values after correction.

| Statistical parameters | Discrepancies before correction | | | | Discrepancies after correction | | | |
|------------------------|---------------------------------|--------------------|---------------------|--------------------|--------------------------------|--------------------|---------------------|--------------------|
| | $F_{T,vac}$ [kN] | $F_{T,SL}$ [kN] | $I_{sp,vac}$ [s] | $I_{sp,SL}$ [s] | $F_{T,vac}$ [kN] | $F_{T,SL}$ [kN] | $I_{sp,vac}$ [s] | $I_{sp,SL}$ [s] |
| Relative mean error | 6.9% | 5.9% | 6.9% | 5.8% | -0.6% | -1.6% | -0.6% | -1.6% |
| Absolute mean error | 6.9% | 5.9% | 6.9% | 5.8% | 1.9% | 2.9% | 1.9% | 2.9% |
| Standard deviation | 3.3% | 4.1% | 3.3% | 4.2% | 3.1% | 3.8% | 3.1% | 3.9% |

2.5.2. Validation of Mass and Geometry Model

Since both the mass and geometry of the vehicle are modelled using empirical data-based estimating relations, they have been validated in the same fashion. First of all, the relationships for length and mass of rocket engines will be compared to published data. The rocket engines are part of a launch vehicle stage and on the level of vehicle stages the mass and geometry models are also validated using data from a range of launching vehicles. Validation of the mass estimating relations for the airplane elements (i.e. wing, fuselage, vertical tail and landing gear) is performed by using data on the operational empty mass of combat aircraft. Finally, bringing all of these elements together, the model is tested on a rocket-propelled, winged vehicle.

The estimated dry masses of 10 rocket engines have been plotted in Fig. 2.13, together with their published dry masses. Similar to the engine of the Dawn Mk-III concept, all the rocket engines used in this analysis use kerosene as fuel, and their estimated and validation data have also been included in Tab. 2.4. The mass estimating relation for the rocket engine mass, presented in Sec. 2.3, is valid for a thrust range from 50 kN to 3500 kN[9], and the expected vacuum thrust of the Dawn Mk-III of 521 kN[7] falls within this range. Table 2.5 shows the calculated statistical parameters, describing the fitness of the model to the validation data. This indicates that for the dry mass on average, the agreement is quite good with a mean relative error of 3%, but there is some spread in the discrepancies with the mean absolute error at 34% and a standard deviation of 45%. Also, the length estimation shows a spread in discrepancies and on average an overestimation of the engine length.

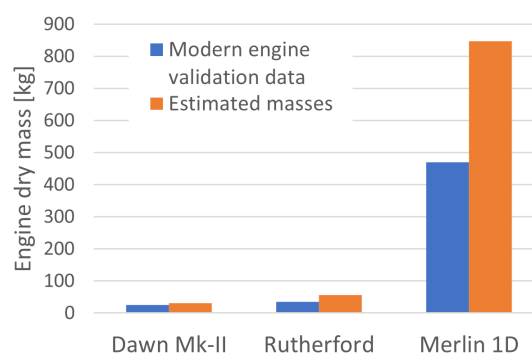
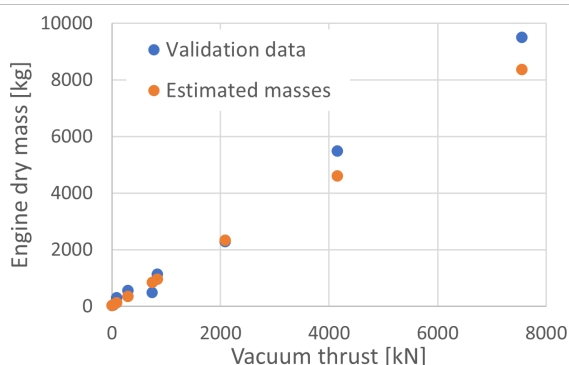


Figure 2.13: Comparison of estimated rocket engine mass and validation data. Figure 2.14: Comparison of estimated mass of modern rocket engines and validation data.

Table 2.4: Validation data and model results of rocket engine mass and lengths.

| Engine name | Source | Validation data | | Estimated data | |
|-------------|--------|------------------|-------------------|------------------|-------------------|
| | | L_{engine} [m] | M_{engine} [kg] | L_{engine} [m] | M_{engine} [kg] |
| RD-171 | | 4.0 | 9500 | 5.03 | 8363 |
| RD-120 | | 3.87 | 1125 | 3.04 | 947 |
| RD-58M | | 2.27 | 300 | 1.80 | 120 |
| Merlin 1D | | 2.92 | 470 | 2.97 | 847 |
| RD-180 | | 3.56 | 5480 | 4.39 | 4609 |
| RD-191 | | 3.78 | 2290 | 3.75 | 2330 |
| RD-0124A | | 1.575 | 548 | 2.40 | 353 |
| Rutherford | | 0.75 | 35 | 1.38 | 56 |
| Dawn Mk-II | | - | 25 | 0.82 | 31 |
| YF-100 | | 2.99 | - | 3.39 | 1507 |

Table 2.5: Statistical parameters of rocket engine mass and length validation.

| Statistical parameter | L_{engine} [%] | M_{engine} [%] |
|-----------------------|------------------|------------------|
| Mean relative error | 20% | 3% |
| Mean absolute error | 28% | 34% |
| Standard deviation | 33% | 45% |

The largest discrepancies are observed for mass in the Merlin 1D engine, and for length in the Rutherford engine, which are both designed and built in more recent times than the other engines used in the comparison. The rocket engines intended for the Mk-III vehicle are expected to use the same technologies and manufacturing techniques as these modern engines. By taking a closer look at the modern engines in Fig. 2.14, one can observe that these are more lightweight than estimated by the historical data-based model. Although there are more modern engines than the three presented here, e.g. the Ursa Major Hadley and Ripley or the Virgin Orbit Newton engines, no credible data could be found. With only a very limited amount of data available for these modern engines, no adjustments could be made to the mass estimating relation for the rocket engine, and the uncertainty is considered acceptable as the engines form only a part of the vehicle for which the mass and geometry is modelled.

The masses and lengths of 8 launching vehicle stages were estimated and compared to empirical data. These reference vehicle are of similar size and dry mass as the Dawn Mk-III concept's first and second stages. The graphs in Fig. 2.15 and 2.16 show the results of these analyses. Statistical parameters describing the agreement between modelled and empirical values are calculated and presented in Tab. 2.6. It can be seen that on average, the estimates are within 6% and 4% for length and mass respectively. However, the mean absolute errors are larger and indicate larger uncertainty of the model. The effects of these uncertainties will be further investigated in the sensitivity analysis in Chapter 4.

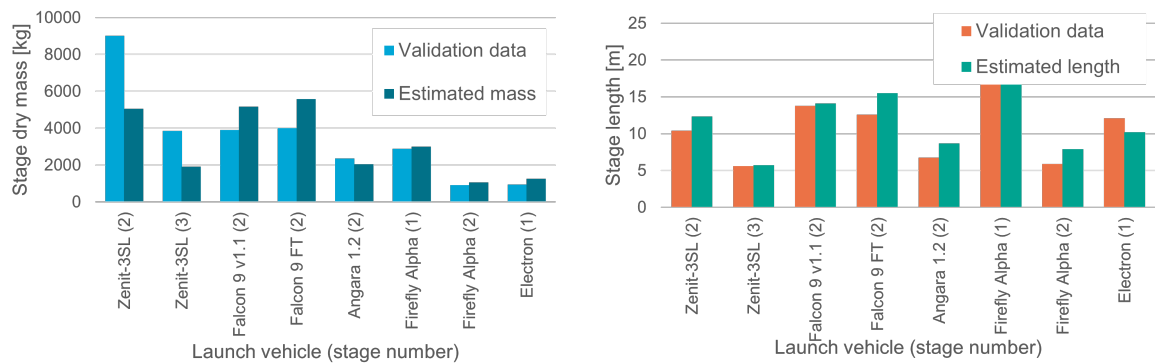


Figure 2.15: Mass validation results of conventional launching vehicles. Figure 2.16: Length validation results of conventional launching vehicles.

Table 2.6: Statistical parameters of launch vehicle stage mass and length validation

| Statistical parameter | l_{stage} [%] | m_{stage} [%] |
|-----------------------|-----------------|-----------------|
| Mean relative error | 6% | -4% |
| Mean absolute error | 18% | 28% |
| Standard deviation | 26% | 33% |

In contrast to regular launching vehicles, the Dawn Mk-III concept also features airplane elements, that allow the vehicle to perform horizontal take-off and landings and return back to the runway. These airplane elements are the wing, fuselage, vertical tail and landing gear. As similar reusable launching vehicles, e.g. those described in Ch. 1, do not have a horizontal tail, it is assumed that this is also not a required element for the Dawn Mk-III. To validate the mass estimating relations of these airplane elements, which are described in Section 2.3, analysis was performed on the four combat aircraft listed in Tab. 2.7, of which values were reported in Roskam [15]. Statistical parameters describing the fit between estimated and actual values are calculated and given in Tab. 2.8.

Table 2.7: Validation data and model results of airplane elements masses

| Aircraft | Validation data | | | | Estimated values | | | |
|----------|-----------------|----------------|----------------|---------------|------------------|----------------|---------------|---------------|
| | m_{wing} [kg] | m_{fus} [kg] | m_{emp} [kg] | m_{LG} [kg] | m_{wing} [kg] | m_{fus} [kg] | m_{VT} [kg] | m_{LG} [kg] |
| F/A-18A | 1723 | 2125 | 429 | 904 | 1651 | 2582 | 203 | 794 |
| F-102A | 1361 | 1546 | 243 | 479 | 1386 | 1396 | 234 | 530 |
| F8U-3 | 1872 | 1746 | 474 | 430 | 1804 | 1578 | 171 | 652 |
| F11F | 989 | 1483 | 303 | 411 | 1006 | 1257 | 103 | 440 |

Table 2.8: Statistical parameters of airplane elements mass validation

| Statistical parameter | m_{wing} [%] | m_{fus} [%] | m_{emp} [%] | m_{LG} [%] |
|------------------------------|----------------|---------------|---------------|--------------|
| Mean relative error | -1% | -3% | -47% | 14% |
| Mean absolute error | 3% | 14% | 47% | 20% |
| Standard deviation | 3% | 17% | 29% | 27% |

For these cases it can be seen there is good agreement on the wing mass estimation, while the fuselage masses show somewhat larger differences. A plausible explanation can be that these differences are because of the uncertainty in the design dive dynamic pressure q_L , which was estimated using either the reported maximum equivalent airspeed, or the cruise equivalent airspeed times a factor 1.25[15]. The wing mass is estimated using geometric parameters and the design gross weight, and the values of these parameters could be obtained with more certainty.

The validation data only provided the mass of the empennage group, and not the individual horizontal or vertical stabilizers. The estimated vertical tail masses are thus much smaller than the reported empennage masses, except for the F102A aircraft. This aircraft only has a vertical stabilizer and it can be seen that the estimated vertical tail mass matches the reported empennage mass.

Finally, the landing gear mass estimation shows reasonable agreement with the validation data. The mass estimating relation of Eq. 2.32 is simply only dependent on the maximum take-off weight. The take-off and landing velocity or the runway conditions that the landing gear is accounted for (e.g. carrier based) likely affect the landing gear mass, but this is not accounted for in the relation. The differences are however small compared to the total vehicle mass and thus are acceptable in the conceptual stage of design.

The last validation effort that was performed on the vehicle mass model is by estimating the mass of a rocket-propelled winged vehicle: The North American X-15. The estimated masses, together with the validation data taken from Roskam [15], are listed in Table 2.9.

Table 2.9: Estimated and validation mass data of North American X-15 aircraft.

| Item | Actual value [kg] | Estimated value [kg] | Discrepancy [%] |
|--------------------|-----------------------------|--------------------------------|---------------------------|
| Wing group | 519 | 592 | 14% |
| Fuselage group | 1726 | 1699 | -2% |
| Empennage group | 575 | | |
| Vertical tail | | 88 | -85% |
| Landing gear group | 176 | 568 | 222% |
| Rocket engine | 308 | 317 | 3% |
| Thrust structure | 85 | 67 | -21% |
| Fuel system | 614 | 307 | -50% |

From these results it can be concluded that the estimation of wing weight and fuselage group has reasonable agreement with the validation data. The estimated vertical tail mass encompasses only 15% of the total empennage mass, which can be explained by the fact that the actual value also covers the mass of the horizontal stabilizer and the ventral fin. Most significant is the overestimation of the landing gear weight by 222%. The X-15 is air-lifted by a B-52 aircraft, and thus does not need its landing gear to perform a take-off maneuver. The landing gear is thus only needed for landing, when the aircraft's weight is significantly reduced by fuel burn. When the landing gear mass is estimated using the aircraft's empty weight, rather than the maximum take-off weight, the overestimation is reduced to 7%. From this it can be deduced that the mass estimating relation for the landing gear is accurate if used for a vehicle that performs a horizontal take-off. As the discrepancies can be explained by the dissimilarity of the X-15 aircraft to the Dawn Mk-III concept, no adjustments were made to the estimating relations in the mass model.

As for the rocket propulsion weights, the discrepancies for the engine and thrust structure masses are acceptable. The mass of the fuel system (tanks, valves, pressurants) on the other hand is underestimated by 50%. Unaccounted for are the hydrogen peroxide tanks, powering the reaction control system and two auxiliary power units. Although the masses of these systems are not reported individually in Roskam [15], it is plausible that these cause a large discrepancy in the fuel system mass estimation. Since the mass of the propulsion system was already validated using a number of liquid-propellant rocket engines, no adjustments

to the model were made.

2.5.3. Validation of Aerodynamic Model

The validity of the aerodynamic model has been evaluated by comparing estimated values of lift and drag versus angle of attack, at various Mach numbers, to experimental data of similar reusable launching vehicles. This was done for three different cases of aircraft: The Orbital Sciences X-34, the PRORA-USV from the Italian Aerospace Research Center, and the Dawn Aerospace Mk-II sub-orbital spaceplane.

The results of the validation study on the X-34 vehicle are presented in the graphs of Figures A.1 and A.2. The validation data was obtained by digitizing the graphs presented in Weiland [22]. The geometric properties required for the analyses were obtained from technical drawings presented in the same work.

For the subsonic conditions, it can be observed that there is good agreement between estimated and validation results. As Figure 2.17 shows, the inclusion of the vortex drag correction based on the achievable leading-edge suction is very important for an accurate estimate of the aircraft's drag.

In the transonic conditions ($M = 0.9$ and $M = 1.05$), there are some discrepancies. However, given that the aircraft during its trajectory spends very little time in these conditions, should not make a large impact on the trajectory simulation. At supersonic conditions, the estimated lift coefficients match the experimental data closely again. The drag estimation of the X-34 in supersonic conditions, captures the general trend or shape of the curve that the experimental data shows, but there is a difference in the estimated zero-lift drag coefficient, which shifts the drag curve in vertical direction. A plausible explanation for these discrepancies may be that the base drag, which is taken into account by the model, is not present in the validation data, stemming from wind tunnel measurements. The wind tunnel model of the X-34 that is shown in Fig. 2.18, is attached to the sting at its base. The presense of the sting at the base should reduce the drag force acting on the base, and this may explain some of the differences with the estimated results.

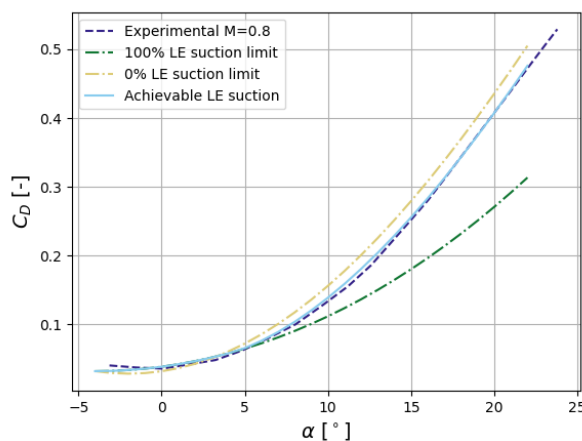


Figure 2.17: Drag estimation of X-34 at $M = 0.8$, including vortex drag estimation using leading-edge suction analogy.

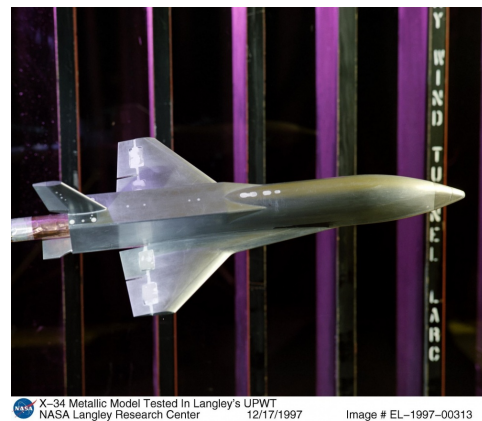


Figure 2.18: Wind tunnel model used for obtaining experimental data of Orbital Sciences X-34, attached to the sting at its base [23].

At very high Mach numbers (from $M = 4.0$) the bridging from the linear estimation method to the Newtonian theory seems to capture the non-linear behavior of the lift curve. This is shown in more detail in Figure 2.19, where both the linear arrow wing method, and the Newtonian impact theory are shown individually. The method of bridging between these models, using a Mach number-dependent logistic function, shows that the experimental lift coefficient can be closely approximated. The procedure of bridging between the models assumes that the actual lift force is the resultant or combination of different aerodynamic phenomena present at the same instance. The blending of the two different models is done using logistic functions, as described in Sec. 2.4, of which the coefficients are determined somewhat arbitrarily, but revolves around the fact that in the validation data, the non-linear lift curve behavior starts to become visible at $M = 4.0$ and becomes stronger as the Mach number further increases.

For the drag coefficient, there is only validation data available at $M = 6.0$. The base drag reduces to zero as the Mach number increases, and therefore no large differences can be observed anymore. Also here, the bridging to the Newtonian impact theory for the drag coefficients shows good approximation to the validation results, and this is shown in more detail in Fig. 2.20.

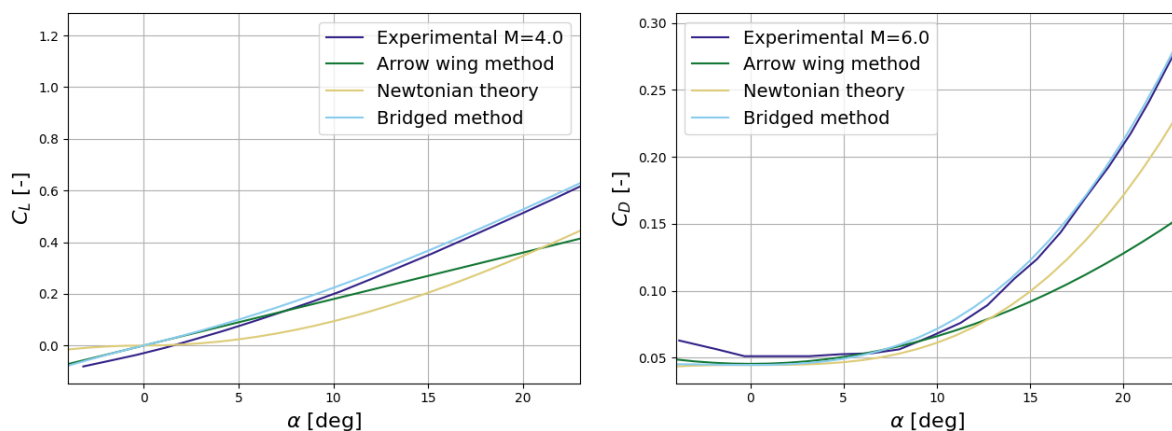


Figure 2.19: Lift curves of X-34 at $M = 4$, showing the bridging from Figure 2.20: Drag curves of X-34 at $M = 6$, showing the bridging from the linear arrow wing method to the non-linear Newtonian theory. the linear arrow wing method to the non-linear Newtonian theory.

The second validation case was performed on the PRORA-USV, shown in Fig. 2.21. Its geometry was derived from the drawings and information provided in Rufolo, Roncioni, Marini, *et al.* [24], even containing the airfoils of the wing. The comparison between estimated values and experimental data is shown in the graphs of Figures A.3 and A.4. It can be seen that for all Mach numbers, there is reasonable to good approximation for both the lift and the drag coefficients. The transonic Mach number of $M = 0.94$ shows the largest discrepancies, but again, this should have very little impact on the result of the trajectory simulation, as the vehicle spends very little time in the transonic regime.

Interestingly, the estimation of zero-lift drag in supersonic conditions is very close to the experimental results. This was achieved by omitting the base drag component and can be justified by looking at the wind tunnel model in Fig. 2.22, where the sting covers the base of the aircraft completely. The source of the validation results also states that this base drag is not included in their results, and that therefore the drag values of the actual vehicle must be higher [24].



Figure 2.21: PRORA Unmanned Space Vehicle developed by Italian Aerospace Research Center (CIRA) [25]. Figure 2.22: Schlieren image of wind tunnel model of the PRORA-USV. [24]

The third validation case that was performed on the aerodynamic model is using data on the Dawn Aerospace Mk-II aircraft. The exact geometry used for the analysis and the aerodynamic data were provided for by the company. The aerodynamic data was produced using CFD simulations, carried out by Dawn Aerospace. Figures A.5 and A.6 show the results of the validation comparison.

The lift coefficients show good agreement to the validation data, with the largest differences observed in the transonic Mach number of $M = 0.95$. The drag estimation in subsonic conditions also resembles the CFD

data well. From Fig. 2.23 it can be seen that the vortex drag can be accurately estimated, based on the leading edge suction that can be achieved. As the vortex drag becomes a significant part of the total drag, the drag estimations are also accurate at higher angles of attack.

In supersonic conditions there are only aerodynamic coefficients available for a small range of angles of attack. However, it can be seen that over this range the general shape of the drag curve is captured in the aerodynamic model. The discrepancy likely originates from the zero-lift drag estimation. The components contributing to the supersonic zero-lift drag estimation, as a function of Mach number, are plotted in Figure 2.24 and compared to reference values from CFD analyses, carried out by Dawn Aerospace. The total zero-lift drag decreases as the Mach number increases, and this trend is also present in the estimated values. However, the estimated values of zero-lift drag are generally underestimated. It is likely that one of the components of friction, wave or base drag is underestimated as the result of over simplifications in the model. For example, the equivalence of a Sears-Haack body for the wave drag estimation may not be as applicable to this particular aircraft geometry. The difference in total drag is highest for an angle of attack of zero, and decreases for higher angles. The impact of the discrepancy relies on the trajectory, i.e. at what range of angle of attack the aircraft will fly in the supersonic domain, and will be further investigated in the sensitivity analysis of Chapter 4.

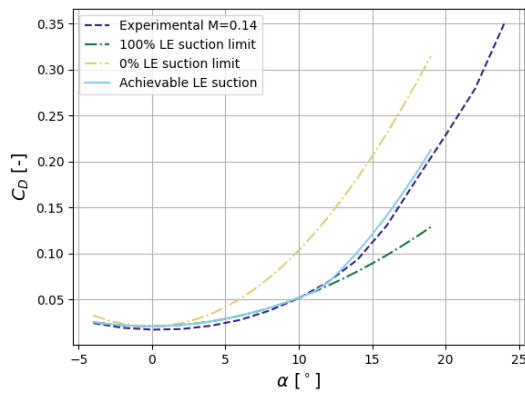


Figure 2.23: Drag estimation of the Dawn Aerospace Mk-II at $M = 0.14$, including vortex drag estimation using leading-edge suction analogy.

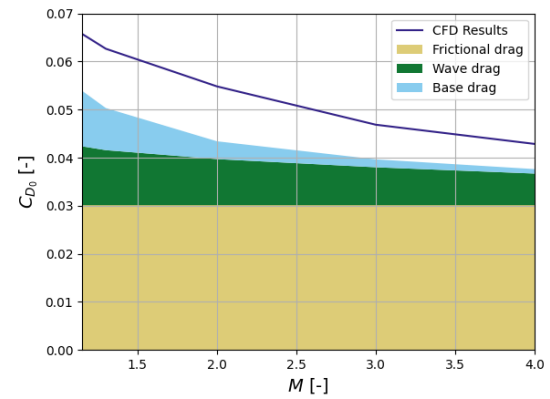


Figure 2.24: Components of supersonic zero-lift drag of the Dawn Aerospace Mk-II.

3

Trajectory Model

The trajectory model receives information on the launching vehicle's characteristics from the vehicle model, in the form of aerodynamic coefficients, masses, and propulsive forces. Using this information, the trajectory model simulates the path the vehicle travels. Since the vehicle consists of two stages, the trajectory of both stages has to be simulated. The first stage trajectory consists of an ascent and a return trajectory, while the upper stage only performs an ascent. The upper stage trajectory starts from the staging point, which is the end of the first stage ascent trajectory. The simulation trajectory of the first stage ascent and return trajectory is explained in Sec. 3.1, and Sec. 3.2 describes the model for the upper stage trajectory.

3.1. First stage trajectory model

The first stage trajectory model essentially has two goals. The first is to find the flight conditions at staging, which form the starting conditions for the second stage trajectory. Secondly, it simulates the vehicle's motion as it makes its way back to the take-off and landing site, and thus determines whether the vehicle is able to fully complete the mission profile. The simulation of the first stage was simplified by assuming a non-rotating earth and planar motion for the mission segments. This allows for the trajectory to be expressed in the two dimensions of downrange and altitude.

The trajectory is simulated by solving the equations of motion of Eq. 3.1 3.2 for the velocity V and flight path angle γ , respectively.

$$m \frac{dV}{dt} = T \cos \alpha - C_D \frac{1}{2} \rho V^2 S_{ref} - mg \sin \gamma \quad (3.1)$$

$$mV \frac{d\gamma}{dt} = T \sin \alpha + C_L \frac{1}{2} \rho V^2 S_{ref} - mg \cos \gamma \quad (3.2)$$

Using numerical integration, the position of the vehicle in terms of altitude h and downrange R is evaluated with Equations 3.3 and 3.4.

$$h(t) = \int_{h_0}^t V \sin \gamma dt \quad (3.3)$$

$$R(t) = \int_{R_0}^t V \cos \gamma dt \quad (3.4)$$

As shown by these equations, there are three kinds of forces acting on the vehicle: The thrust force T , the aerodynamic forces (lift and drag), and the gravitational force. For the thrust force, no throttling is implemented in the model, which means that the rocket engine is always thrusting at either 100% or 0%. The aerodynamic forces are found by taking the lift and drag coefficients and multiplying them with the dynamic pressure and

the wing reference area. As the vehicle reaches altitudes outside of the atmosphere, the dynamic pressure and the aerodynamic forces reduce to zero. The gravitational force mg depends on the vehicle's mass, which changes significantly over the course of the trajectory. Equation 3.5 describes the change of mass over time due to propellant mass flow \dot{m} , starting with the take-off mass m_{TO} . In addition to the propellant mass reduction, the first stage vehicle mass also reduces after staging, when the upper stage vehicle is ejected.

$$m(t) = m_{TO} - \int_{t_0}^t \dot{m} dt \quad (3.5)$$

Then to solve these equations, the angle of attack must be supplied, which is done differently for every mission segment. The approach to this is explained in the following subsections.

3.1.1. Take-off

The take-off maneuver consists of a ground run and an aerial phase, as is shown in Fig. 3.1. The take-off maneuver consists of a ground run and an aerial phase. For the ground run, the angle of attack is kept to zero until a velocity is achieved at which enough lift can be generated to lift off. This speed is the lift-off speed V_{LOF} , and corresponds with the lift coefficient $C_{L_{LOF}}$, according to equation 3.6. This lift coefficient is taken from the lift curve, estimated by the vehicle model, at the maximum angle of attack as constrained by the landing gear $\alpha_{max,LG}$.

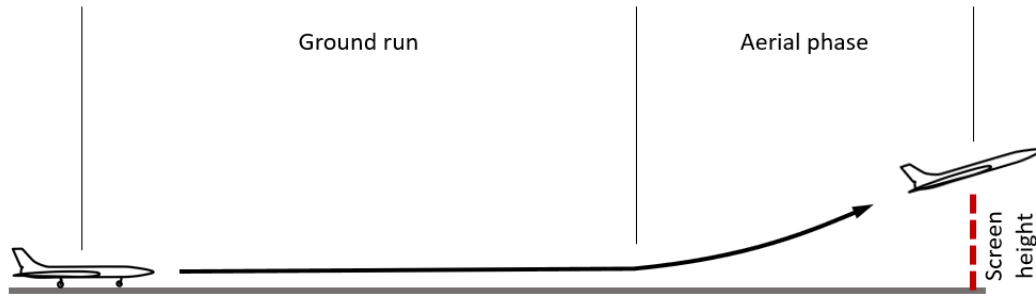


Figure 3.1: Schematic of take-off maneuver, comprising of ground run and aerial phase.

$$m_{TO} \cdot g = L = C_{L_{LOF}} \frac{1}{2} \rho V_{LOF}^2 S \quad (3.6)$$

As soon as the lift-off speed is achieved, the angle of attack is increased to the maximum value $\alpha_{max,LG}$, which for the analyses done in this research is set at 25° . As a result of this angle of attack, the vehicle's flight path angle and altitude increase, until a screen height is cleared of 50 ft above ground level. The angle of attack profile during the take-off is illustrated in Figure 3.2.

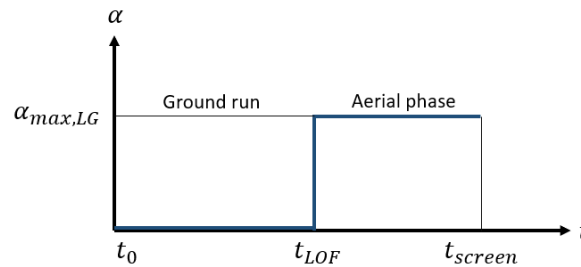


Figure 3.2: Angle of attack profile during take-off maneuver.

3.1.2. Powered ascent

After clearing the screen height, the vehicle enters the ascent phase and first assumes the angle of attack that yields the highest lift to drag ratio, which increase the flight path angle further to the target value at staging $\gamma_{staging}$. This is an important input parameter to the trajectory model, as it is the flight path angle at which

the upper stage is released, and the effect on the upper stage trajectory is further explained in Sec. 3.2. When the target flight path angle is reached it is maintained, and the model finds the angle of attack that yields the right hand side of Equation 3.2 to zero ($\frac{d\gamma}{dt} = 0$). The ascent phase ends when the propellant of the first stage vehicle is depleted, which is called the staging point. The angle of attack and flight path angle profiles are illustrated in Figure 3.3.

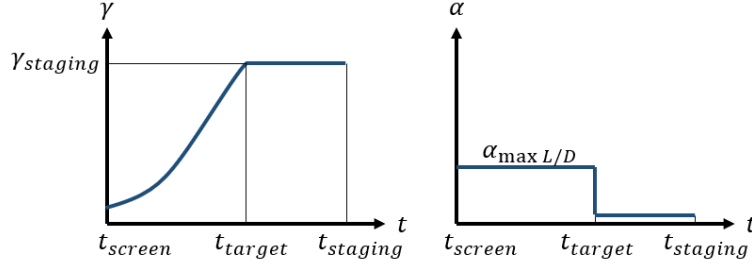


Figure 3.3: Illustration of angle of attack vs. time (left) and flight path angle vs. time (right) used to model first stage ascent segment.

3.1.3. Parabolic coast

The parabolic coast segment concerns the first stage vehicle only, starting at the instant that the first stage engines complete their burn and ending when the atmosphere is reached at $t = t_{entry}$. This is taken as reaching an altitude of 86 km, as it is the maximum altitude that the ISA includes, where the air density is less than 10^{-5} times the sea-level value. During the parabolic coast that follows the ascent phase, the aerodynamic forces are reduced to zero as the air density decreases to zero and the thrust force is no longer applied. The vehicle follows a ballistic arc until it reaches the atmosphere again.

3.1.4. Re-entry

The re-entry in the atmosphere starts when the vehicle reaches an altitude of 86 km in a high speed descending motion. The re-entry segment is harsh on the aircraft as its surface is heated by air friction. Although the effect of aerodynamic heating on the vehicle design is considered outside the scope of this study, it is used as a means to simulate the re-entry trajectory. The aerodynamic heating is modelled using the stagnation point heat flux $q_{c,s}$, which can be calculated relatively easy, using equation 3.7 [26]. In this equation, the factor k is a function of the nose radius R_n , as in Eq. 3.8. The value of the nose radius is taken from the leading edge radius of the wing's airfoil section. A sharper leading edge, thus smaller leading edge radius will lead to more heating. The parameter g_w is the ratio of wall temperature over adiabatic wall temperature. The factors N_1 and N_2 can be set to 0.5 and 3, and the parameter g_w to zero, as suggested by Dirkx and Mooij [26].

$$q_{c,s} = k \rho^{N_1} V^{N_2} \quad (3.7) \quad k = \frac{1.83 \cdot 10^{-4}}{\sqrt{R_n}} (1 - g_w) \quad (3.8)$$

The re-entry segment can be further split up into three phases. In the first phase, the angle of attack is maximized to generate as much drag as possible and start decelerating. This maximum angle of attack will be determined based on predicted stall angle, or on reference data of similar vehicles in [22]. As the air density is increasing in the descending motion, the stagnation point heat flux increases to a peak value. After the peak, the heat flux reduces to a reference value $q_{c,s,ref}$, which is supplied as an input to the trajectory model. In the second phase of the re-entry segment, the angle of attack is reduced to track the stagnation point heat flux at the reference value. A reference value of 90 kW/m² was suggested in [7]. If the maximum value in the first phase is lower than the reference value, this maximum value is maintained in phase two. The second phase ends when the angle of attack reaches a minimum value, which can be set based on the angle at which the lift to drag ratio is maximum. In the third phase, the angle of attack is kept at this minimum to let the aircraft pull out of the dive to a specified Mach number. The angle of attack and expected stagnation point heat flux over time for the three phases of the re-entry are illustrated in Fig. 3.4.

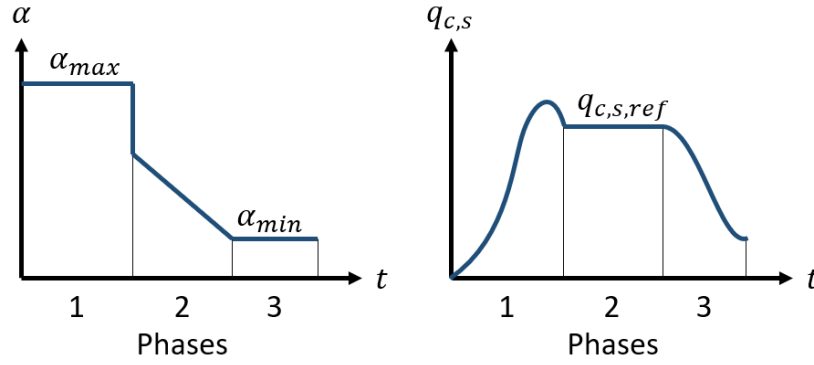


Figure 3.4: Profile of angle of attack and stagnation point heat flux vs. time. Phases of re-entry segment are indicated in graphs (1, 2, 3).

3.1.5. Turn

After the re-entry, the course of the aircraft has to be changed back towards the runway by doing an unpowered 180° turn. Since the turn is unpowered, but follows directly after the high-speed re-entry segment, the turn can be either in descending or ascending motion. For this motion, it is assumed that the sideslipping force is zero. Also, with the aircraft now having depleted all of its propellant it is much lighter, and since the aircraft structure is designed for the maximum take-off weight, it can sustain high accelerations during the turn maneuver. Therefore, a constant angle of attack of 25° (similarly as for the take-off segment) is used, in combination with a constant bank angle ϕ of 45° . To account for the turn maneuver, Equation 3.2 is rewritten to the form of Equation 3.9 (with the absence of the thrust force). The turning radius and rate can be evaluated using Equations 3.10 and 3.11. The turn maneuver ends when the heading of is turned 180° in negative downrange direction.

$$mV \frac{d\gamma}{dt} = L \cos \phi - mg \cos \gamma \quad (3.9)$$

$$m \frac{V^2}{r_{\text{turn}}} = L \sin \phi \quad (3.10)$$

$$\Omega = \frac{V}{r_{\text{turn}}} \quad (3.11)$$

3.1.6. Glideback

During the glideback the aircraft flies at the angle of attack that yields the maximum lift to drag ratio for its current Mach number. One might expect that this condition results in a constant flight path angle. However, the aircraft is still flying at high speeds, and the optimum lift-to-drag ratio yields such an amount of lift that the trajectory is curved upwards to the upper layers of the atmosphere. Here, the atmosphere's density is so low that the aerodynamic forces diminish and puts the aircraft again in a sort of parabolic arc, until the denser atmosphere is reached. During these 'skips', a lot of downrange is covered back to the take-off and landing site, at the expense of a relatively low amount of kinetic or potential energy. After a few skips, however, the velocity decreases to subsonic conditions and the oscillating trajectory motion is damped to the constant optimum flight path angle. An example of the skipping motion during the glideback is shown in Fig. 3.5.

The segment ends when the altitude is reduced to the screen height of 50 ft above ground level. At this point, a calculated downrange of smaller than or equal to zero indicates that the vehicle is capable of returning back to the take-off and landing site.

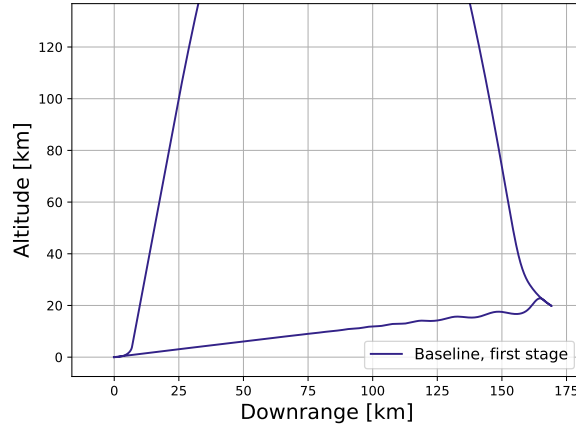


Figure 3.5: Simulated altitude vs. downrange profile of Dawn Mk-III concept, shown as an example of the oscillating gliding motion.

3.1.7. Landing

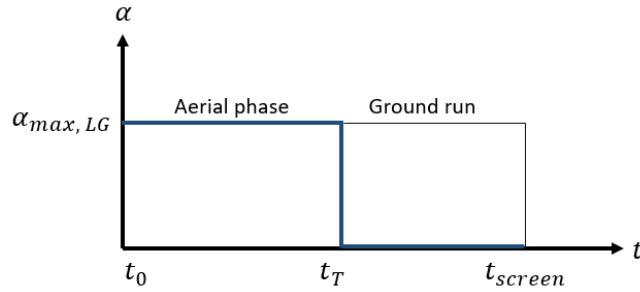


Figure 3.6: Angle of attack profile during landing segment, indicating ground run and aerial phase.

Finally, a landing maneuver is simulated in a similar way as the take-off maneuver, but with ground run and aerial phase in reverse order. A constant angle of attack is assumed for the aerial part, which pulls the aircraft up to a flight path angle of zero. This is followed by a ground run, where braking is applied. The equation of motion of Eq. 3.1 is rewritten to the form of Equation 3.12, to include the braking force D_B . This braking force is defined by Eq. 3.13, and is dependent on the achievable braking frictional coefficient μ_b . A value of 0.9 times the maximum frictional coefficient μ_{max} is suggested in Ruijgrok [27]. The value of μ_{max} depends on the condition of the runway surface, but for a dry runway a value between 0.7 and 0.9 can be taken [28]. Solving the equation of motion numerically yields the ground run distance of the landing maneuver. The angle of attack profile used during the landing maneuver is illustrated in Fig. 3.6

$$m \frac{dV}{dt} = -C_D \frac{1}{2} \rho V^2 S - D_b \quad (3.12)$$

$$D_b = \mu_b (mg - C_L \frac{1}{2} \rho V^2 S) \quad (3.13)$$

3.1.8. Environmental models

The air density ρ and gravitational acceleration g change during the ascent maneuver, and are a function of altitude. For the air density, the International Standard Atmosphere (ISA) model is used, which also yields the air temperature as a function of altitude to be used for calculation of the Mach number. For the change of gravitational acceleration, Eq. 3.14 is used, which corrects the value at sea level g_0 for the altitude h . The radius of Earth R_E is taken as 6371 km.

$$g = g_0 \left(\frac{R_E}{R_E + h} \right)^2 \quad (3.14)$$

3.1.9. Velocity losses

To deliver a payload to orbit an orbital velocity must be achieved. The change of velocity delivered by a rocket-propelled vehicle, without considering any losses, is defined by the Tsiolkovsky equation, given in Eq. 3.15. The velocity increment, or Delta-V is a function of the rocket's specific impulse and the ratio of initial over final vehicle mass $\frac{m_0}{m_f}$. In reality, the actual achieved Delta-V is lower due to losses from four sources: gravity, aerodynamics, steering and pressure.

$$\Delta V = I_{sp} g_0 \ln \frac{m_0}{m_f} \quad (3.15)$$

Gravity losses can be described as the deceleration of the vehicle's velocity due to the gravitational force, and is defined by the Eq. 3.16. As indicated by the term $\sin \gamma$, a high flight path angle inherently introduces a large amount of loss due to gravity.

$$\Delta V_g = \int_0^t g \sin \gamma dt \quad (3.16)$$

Aerodynamic losses are induced by the drag force, which always acts in the direction of the velocity vector. The definition is given in Eq. 3.17.

$$\Delta V_A = \int_0^t \frac{C_D \rho V^2 S_{ref}}{2m} dt \quad (3.17)$$

Steering losses are induced when the thrust vector is not aligned with the velocity vector, and thus are a function of the vehicle's angle of attack.

$$\Delta V_S = \int_0^t \frac{T(1 - \cos \alpha)}{m} dt \quad (3.18)$$

Finally, the pressure loss occurs due to a reduction of the rocket engine performance in ambient pressure. As the vehicle climbs out of the atmosphere, the ambient pressure reduces to zero and thus pressure losses only occur in the presence of the atmosphere. The pressure loss can be calculated using Eq. 3.19, where T is the vehicle's instantaneous thrust, and T_{vac} is the thrust value in vacuum.

$$\Delta V_P = \int_0^t \frac{T_{vac} - T}{m} dt \quad (3.19)$$

3.2. Upper stage trajectory model

The boundary conditions of the second stage trajectory are set by the top level requirements on the targeted orbit. The type of orbit has a large influence on the maneuver, as the vehicle is launched from a spinning earth. Although one of the main goals of launching a payload to orbit is achieving a certain velocity, the initial velocity given by the earth's rotation is not always beneficial. This is especially the case for the sun-synchronous orbit (SSO), as it is considered the most demanding in terms of delta-V.

The inclination angle of a sun-synchronous orbit can be derived from the orbital precession rate ω_p , which should be equal to $360^\circ/\text{year}$. The equation for the orbital precession for a circular orbit (i.e. zero eccentricity) is given in Eq. 3.20.

$$\omega_p = -\frac{3}{2} \frac{R_E^2 J_2}{a^2} \omega_O \cos i \quad (3.20)$$

In this equation, J_2 is the perturbation of the orbit due to the oblateness of the earth, a is the semi-major axis of the target orbit, ω_O is the orbit's angular velocity and i is the inclination angle. For a circular orbit, the semi-major axis a is equal to the sum of the earth's radius and the target altitude. Equation 3.21 then gives the orbital angular velocity, where μ_g is the standard gravitational parameter.

$$\omega_O = \sqrt{\frac{\mu_g}{a^3}} \quad (3.21)$$

This yields for a circular sun-synchronous orbit at an altitude of 600 km an inclination angle of approximately 97.8° . This means that the orbit is retrograde with respect to the rotation of the earth and thus the initial velocity is in opposite direction to the desired direction. This initial velocity V_E is a dependent on the latitude of the launch site and can be estimated using Eq. 3.22. Using spherical trigonometry, the inertial launch azimuth angle $\beta_{0,i}$ can be derived, as a function of the orbit's inclination angle and the launch site's latitude angle. This is given in equation 3.23.

$$V_E = \omega_E R_E \cos \lambda \quad (3.22)$$

$$\sin \beta_{0,i} = \frac{\cos i}{\cos \lambda} \quad (3.23)$$

Using simple velocity triangles expressed on a plane tangential to the earth's surface, the relative velocity ΔV that needs to be delivered by the launching vehicle to achieve the inertial orbital velocity $V_{O,i}$, which is illustrated in Fig. 3.7.

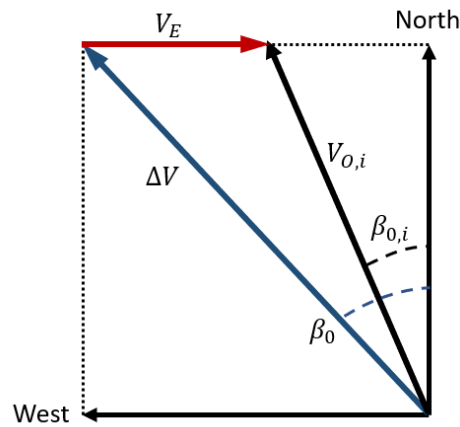


Figure 3.7: Velocity triangles used as relation between inertial orbital velocity and delta-V to be delivered by launching vehicle.

Now the total velocity to be delivered by the launching vehicle is determined, the upper stage trajectory is considered as planar motion in the equatorial plane. It is assumed that at staging the vehicle is already at an altitude close to or above 100 km, and therefore any aerodynamic force is neglected. The mass flow of the upper stage engine is assumed to be constant at its maximum value, as the type of engine is the same as in the first stage vehicle. As described in Subsec. 3.2, the upper stage vehicle performs a gravity turn maneuver to reach the orbit. It is thus assumed that the angle of attack is always zero, and that the only force steering the trajectory (i.e. with a component perpendicular to the velocity vector) is gravity. Although in principle the trajectory can to a degree be controlled by thrust vectoring or throttling, this is sort of guidance is considered to be outside of the scope of the proposed thesis research.

Starting with the staging velocity $V_{staging}$, flight path angle $\gamma_{staging}$ and altitude $h_{staging}$, the motion of the upper stage can be described by reducing Equations 3.1 and 3.2 to the following equations of motion:

$$m \frac{dV}{dt} = T - mg \sin \gamma \quad (3.24)$$

$$mV \frac{d\gamma}{dt} = -mg \cos \gamma \quad (3.25)$$

The upper stage trajectory is the result of the conditions at staging and any kind of steering. Steering of the upper stage is achieved through vectoring of the thrust at an angle of attack. This angling of the thrust

vector introduces losses in the amount of Delta-V that can be achieved. It is therefore important the amount of required steering is minimized, and therefore the staging flight path angle must be such that the upper stage can reach orbit using a gravity turn, with minimum steering. A flight path angle at staging that is out of bounds, either too small or too large, causes the upper stage to fail to reach orbit, as is illustrated by Fig. 3.8.

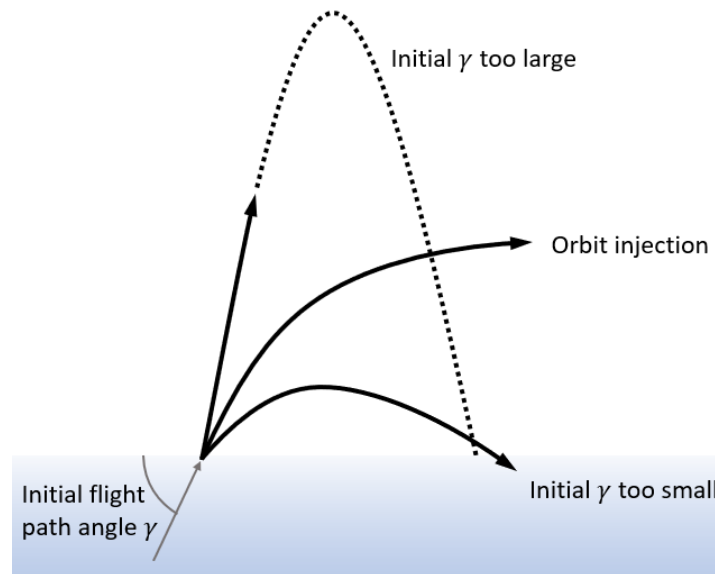


Figure 3.8: Illustration indicating the importance of flight path angle parameter at the begin of the upper stage burn.

Similar as for the first stage trajectory an angle of attack profile must be supplied to the upper stage trajectory model. This was done by specifying angles of attack held constant for a specific duration. An example of a specified angle of attack profile for the upper stage is illustrated in Figure 3.9.

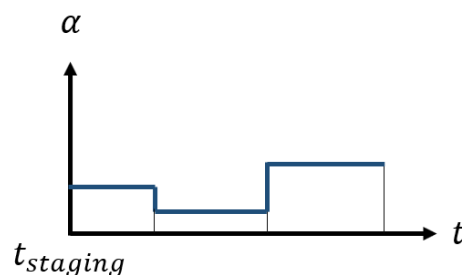


Figure 3.9: Illustration of angle of attack profile that must be specified for upper stage trajectory.

The upper stage performs two burns. The first burn increases the velocity, such that the apogee of a ballistic arc following the this burn reaches the targeted orbit altitude. The second burn is initiated when the vehicle has reached the apogee, and circularizes the orbit by raising the perigee to the targeted orbit altitude.

3.3. Trajectory model validation

A similar concept of a reusable launching vehicle was investigated by Maddock, Toso, Ricciardi, *et al.* [29], where also a vehicle and a trajectory model were constructed. The vehicle in the study is a two-stage-to-orbit vehicle, launched from an aircraft over Prestwick Airport (Scotland), rather than from a runway. The first stage is reusable and designed as a winged vehicle to perform a horizontal landing at an unspecified runway downrange of the launch location, thus not requiring a turn maneuver. The vehicle model developed by [5] is very similar to the model described in this thesis, containing a propulsion, mass and aerodynamics model. However, it is more elaborate in the trajectory simulation, which is determined by solving an optimal control problem, whereas the model described in this thesis requires direct inputs from the user to perform the trajectory simulation.

The mass of both vehicle stages were published, as well as their thrust levels. These values were replicated

using the vehicle model's mass and propulsion elements, as described in Chapter 2. The mass and propulsion parameters of both the validation case as from the model described in this thesis are presented in Table 3.1, showing good agreement. Since the aerodynamic shape of the vehicle in Maddock, Toso, Ricciardi, *et al.* [29] was based on the Orbital Sciences X-34, the planform parameters of the X-34 were used as inputs to the analysis.

As the validation case describes a vehicle air-launched from a carrier aircraft, the trajectory simulation omits the take-off segment and starts with the launch altitude and velocity as described in Table 3.2. The table also includes the targeted orbit parameters in terms of altitude and inclination angle, which were direct inputs to the simulation. The flight path angle at staging, which is an important input parameter to the trajectory model was set to 27°, as this value was found to best replicate the staging conditions published by [5].

Finally, an angle of attack profile for the upper stage ascent was applied. While for the validation case this was the result of an optimization problem, the angle of attack profile must be specified for the trajectory simulation of this thesis. A constant angle of attack of 13° was used for a duration of 400 s was used to approximate the angle of attack profile resulting from the simulation of Maddock, Ricciardi, West, *et al.* [5].

Table 3.1: Comparison of the vehicle characteristics of the Maddock, Toso, Ricciardi, *et al.* [29] study and results of the vehicle model, used for the trajectory validation case.

| Stage | Parameter | Validation case | Model result | Unit |
|-------------|------------------|-----------------|--------------|------|
| First stage | Total mass | 70872 | 70225 | kg |
| | Dry mass | 11343 | 11960 | kg |
| | Total thrust | 1164 | 1167 | kN |
| | Specific impulse | 330 | 332 | s |
| Upper stage | Total mass | 12996 | 12395 | kg |
| | Dry mass | 1853 | 1752 | kg |
| | Total thrust | 129.6 | 129.8 | kN |
| | Specific impulse | 352 | 354 | s |

Table 3.2: Orbit and trajectory parameters used as inputs for the trajectory model.

| Parameter | Value | Unit |
|---------------------------|-------|------|
| Orbit altitude | 600 | km |
| Orbit inclination | 88.2 | ° |
| Launch altitude | 11 | km |
| Launch latitude | 58.8 | ° |
| Launch velocity | 250 | m/s |
| Staging flight path angle | 27 | ° |
| Upper stage AoA | 18 | ° |
| Upper stage AoA duration | 200 | s |

The results of the trajectory simulations from Maddock, Toso, Ricciardi, *et al.* [29], from the model presented in this report, and from the work of Haex [7], which performed the same validation case, are plotted in Figures 3.10 to 3.12. Some observations can be made from the comparison between the different results. Overall, it can be said that the conditions at staging are very similar. At the time of staging, only small deviations in velocity and altitude are present: Approximately 1.8% difference in velocity and 2.9% difference in altitude.

The upper stage ascent, following the staging event, shows some discrepancies. In the altitude versus time profile, it can be seen that the modeled trajectory increases in altitude faster than the validation case. Also the result from Haex [7] shows this behavior. This is likely caused by the difference in angle of attack profile used in each study. While for the Maddock, Toso, Ricciardi, *et al.* [29] and Haex [7] simulations, the angle of attack profile is a result of an optimization process, a more simplified constant angle of attack is specified as input for the trajectory model. By tuning this profile, a closer match with the validation case can be achieved.

From the velocity versus time profile, it is visible that all simulations achieve the orbital velocity in two burns: the first burn to reach an elliptical orbit with an apogee at 600 km, and a second orbit to circularize the orbit. In case of the model presented in this report, as well as in the work of Haex [7], no throttling of the propulsion was implemented. In the validation case, a more smooth change of velocity is visible in the velocity profile due to the fact that the propulsion is gradually throttled up or down. The moments in time when the first

burns end and the second burns start differ for the model result and the Haex [7] validation case, and can be explained by the small discrepancies in upper stage dry mass, which can have a large impact on the velocity profile.

The first stage return trajectories show some differences between the various studies. First of all, some discrepancies are visible in the parabolic arc, in terms of the apogee altitude, time and downrange. During this segment, only gravitational forces are present and therefore it seems that small variations in the staging conditions can have a somewhat larger impact on the parabolic arc, and thus also on the point of re-entry. Although the point in time where the vehicle re-enters the atmosphere differs, the re-entry and glide maneuver of the model result and the Haex [7] study show very similar behavior. The Maddock, Toso, Ricciardi, *et al.* [29] case shows a less steep change in velocity during re-entry, and since deceleration during re-entry is only caused by aerodynamic forces, the difference can only be caused by different aerodynamic characteristics. This hypothesis cannot be confirmed, as the aerodynamic coefficients of the Maddock, Ricciardi, West, *et al.* [5] vehicle were not published.

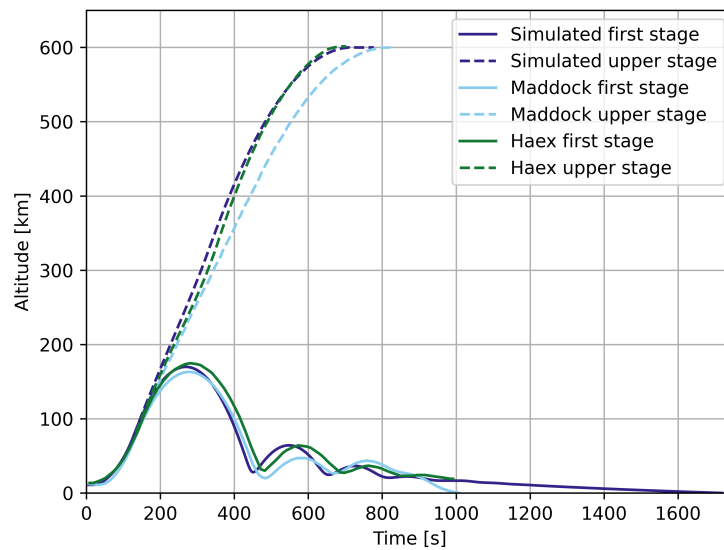


Figure 3.10: Comparison of altitude over time between the simulated result, the Maddock *et al.* validation case, and the Haex validation case.

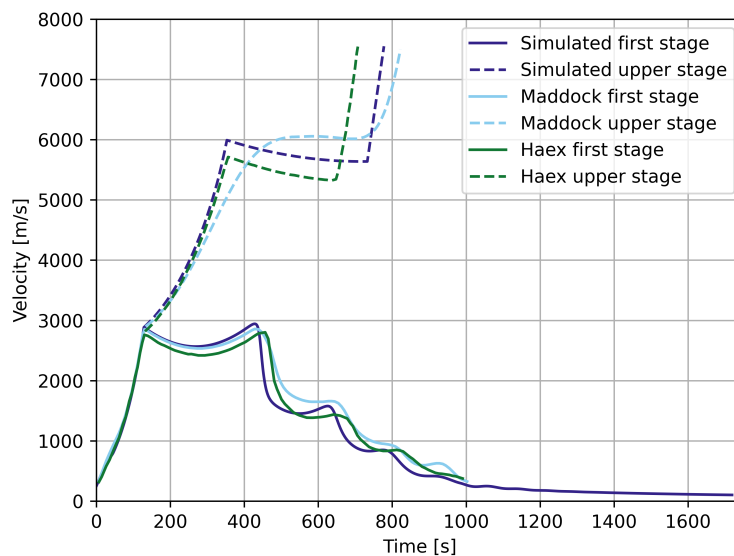


Figure 3.11: Comparison of velocity over time between the simulated result, the Maddock et al. validation case, and the Haex validation case.

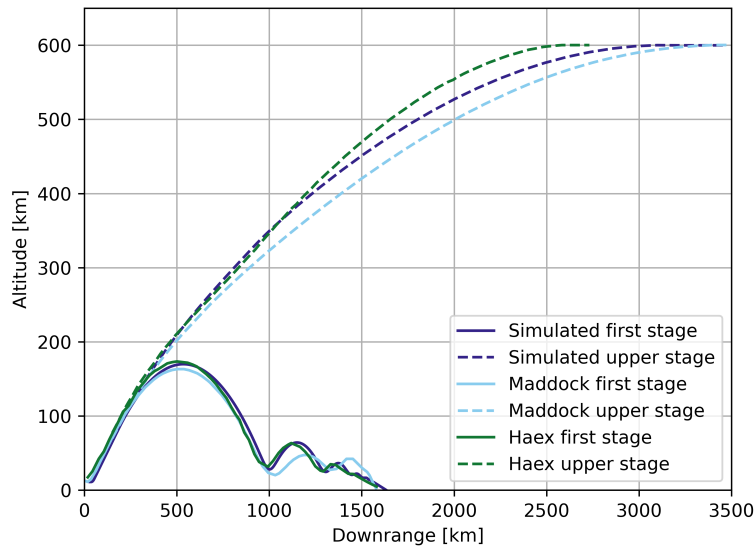


Figure 3.12: Comparison of altitude versus downrange between the simulated result, the Maddock et al. validation case, and the Haex validation case.

4

Sensitivity analysis

To investigate what design parameters are most relevant to influence the mission performance of the launching system, a sensitivity analysis was performed. In this analysis, vehicle and trajectory design parameters were varied and the effect on the mission performance monitored. Sections 4.2 and 4.3 discuss the sensitivity to vehicle design and trajectory parameters, respectively. The analysis also provided an opportunity to investigate the effects of uncertainties in parts of the vehicle model, which is described in Sec. 4.4. However, first a baseline needed to be established, from which design parameters were varied, explained in Sec. 4.1.

4.1. Baseline design

To establish a starting point for sensitivity analyses and case studies, the baseline design presented in Table 4.1 was used, resulting in the trajectory as shown in the graphs of Figures 4.1 to 4.3.

The baseline design was inspired from the design described by Haex [7]. The reported design parameters on the rocket engines, amount and type of propellant, as well as the planform parameters of the X-34 aircraft were used as inputs to the developed vehicle model of Chapter 2. Also the targeted orbit, in terms of altitude, and inclination angle as reported in Haex [7] were used as inputs to the trajectory model of Chapter 3. The trajectory model then produced a simulation of the trajectory, from which the mission performance can be deduced. Most importantly, from the simulation it can be inferred whether the two most important requirements can be met. Namely, reaching the targeted orbit with the upper stage, and reaching the same runway for landing.

However, it was found that by using the same vehicle parameters as in Haex [7], the mission could not meet both of two requirements. This was in contrast to the results of the study by Haex [7], in which simply the aerodynamic performance of the X-34 aircraft was assumed. It appeared that the launching vehicle used in the developed model of this report, with a scaled version of the X-34 planform, did not have the same gliding performance and therefore was not able to make it back to the runway.

To solve this for the baseline design, the planform was modified from the original X-34 planform, with the goal of increasing the gliding performance. Also, the amount of delta-V delivered by the first stage was decreased, and that delivered by the upper stage was increased, by decreasing the amount of propellant put in the first stage and increasing the amount of propellant for the upper stage.

Furthermore, the flight path angle at staging was increased to a fairly high value of 79° . While a higher staging flight path angle causes the first stage vehicle to re-enter the atmosphere closer to the take-off and landing runway, reducing the gliding distance, it has the adverse effect that it causes high gravity losses for the upper stage trajectory. These high gravity losses were also the case for Haex [7], with an approximate flight path angle at staging of 70° .

To counteract the gravity losses, an angle of attack profile was applied to the upper stage trajectory, with first a period of negative angle of attack, followed by a period with positive angle of attack, as displayed in Figure 4.4. This angle of attack profile was already used by a numerical optimization scheme in [7], but the effect of this

was not properly understood. In this study, it was found that the angle of attack profile effectively reduces the time spent at a high flight path angle, and consequently reduces gravity losses, while the steering losses associated with the thrusting at a nonzero angle of attack were acceptable. Although one might intuitively expect that a minimum amount of steering yields the most efficient trajectory, steering is a very important tool reduce gravity losses, especially in case of a high staging flight path angle.

The resulting design does feature an upper stage dry mass fraction, of which the feasibility is questionable. Because of the relatively large portion of the delta-V to be delivered by the upper stage, the ratio of upper stage propellant over dry mass is very large, which was also shown by Haex [7]. It was identified that without the requirement of landing at the same runway as take-off, the design would not be driven to such extreme proportions. The design case studies that were done in Chapter 5, revolve around identifying the design parameters that are most relevant to influence the feasibility of the design.

Table 4.1: Vehicle design and trajectory parameters of the baseline design.

| Parameter | Value | Unit | Stage | Parameter | Value | Unit |
|---------------------------|-------|----------------|-------------|------------------|-------|------|
| Orbit altitude | 600 | km | First stage | Total mass | 43556 | kg |
| Orbit inclination | 97.8 | ° | | Dry mass | 6998 | kg |
| Launch altitude | 0 | km | | Propellant mass | 30000 | kg |
| Launch latitude | 44 | ° | | Total thrust | 531 | kN |
| Staging flight path angle | 79 | ° | | Specific impulse | 302 | s |
| Wing span | 11.35 | m | Upper stage | Total mass | 6558 | kg |
| Wing root chord | 5.72 | m | | Dry mass | 308 | kg |
| Wing tip chord | 1.45 | m | | Propellant mass | 6000 | kg |
| Wing LE sweep angle | 45 | ° | | Payload mass | 250 | kg |
| Wing reference area | 40.7 | m ² | | Total thrust | 39.8 | kN |
| Wing aspect ratio | 3.16 | - | | Specific impulse | 338 | s |
| Fuselage diameter | 2.4 | m | | | | |
| Fuselage length | 15.6 | m | | | | |

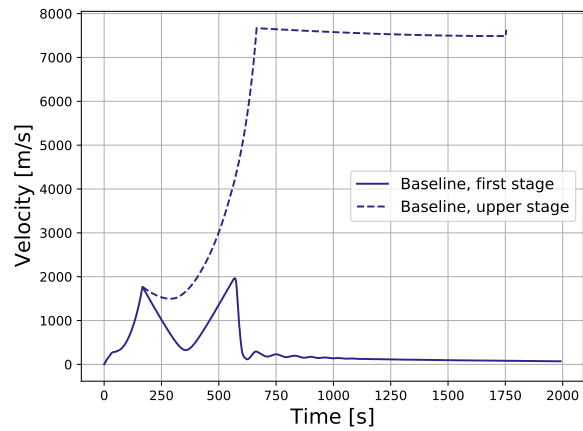
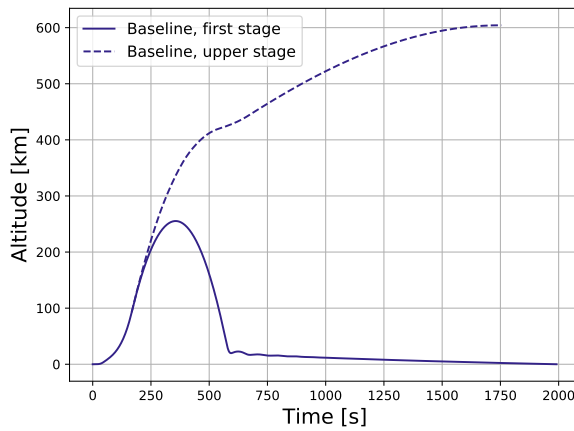


Figure 4.1: Simulated first and upper stage trajectories of the baseline design, in altitude vs. time.

Figure 4.2: Simulated first and upper stage trajectories of the baseline design, in velocity vs. time.

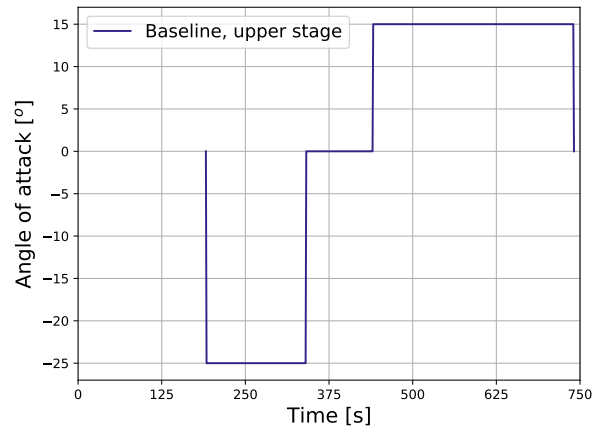
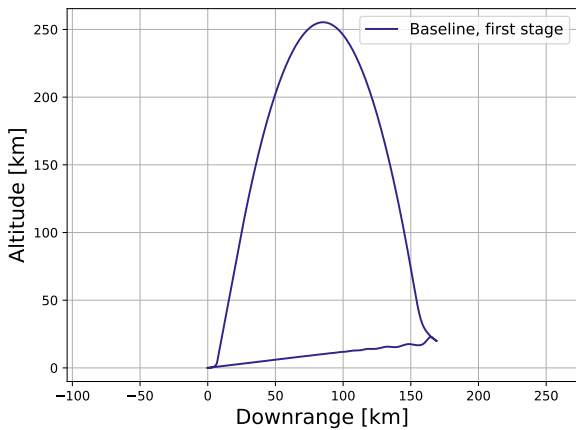


Figure 4.3: Simulated first stage trajectories of the baseline design, in altitude vs. downrange.

Figure 4.4: Angle of attack profile applied to upper stage trajectory.

4.2. Sensitivity to planform parameters

By changing the input parameters that define the wing planform, one can generate an understanding of the way the mission performance is influenced by the wing design. Three different characteristics of the wing design have been changed individually, while keeping the others constant, which are the wing aspect ratio AR , the wing surface area S_{wing} and the leading edge sweep angle Λ_{LE} .

4.2.1. Wing aspect ratio

Variations in wing aspect ratio were achieved by changing the wing span and chords, while keeping the total surface area and the sweep angle constant. The resulting trajectories are shown in Figures 4.5 to 4.7. With an increase in aspect ratio, the mass of the wing is increased, and this has the result that less delta-V is delivered by the first stage vehicle. Because of this, the upper stage vehicle for the increased aspect ratios does not reach orbital velocity. The delta-V budgets of the first stage vehicles is visualized in Figure 4.8 and tabulated in Table 4.2. It can be seen here that the increased aspect ratio reduces the aerodynamic losses experienced by the first stage vehicle.

The return trajectory of the first stage vehicle seems to benefit from the increased aspect ratio, as the increased gliding distance makes it easier to reach the take-off and landing runway.

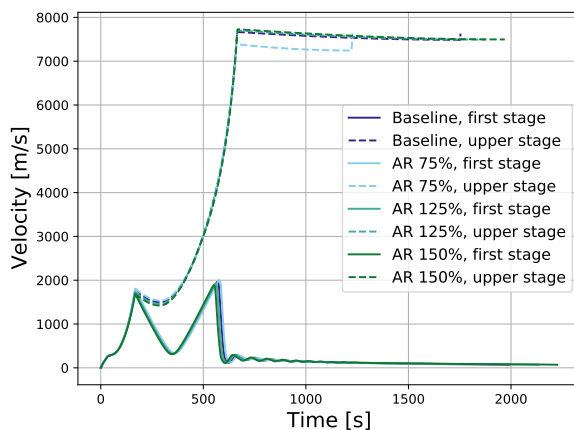
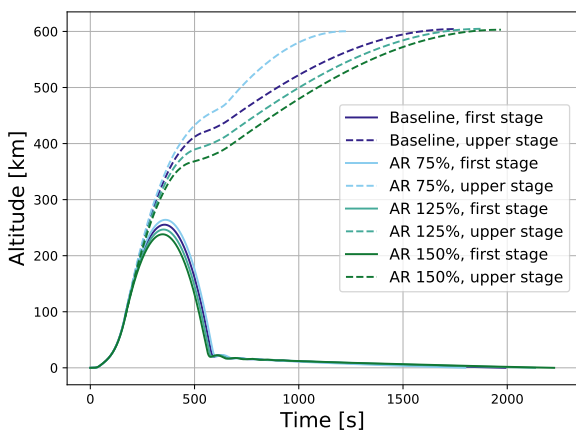


Figure 4.5: Altitude vs. time for four different values of wing aspect ratio.

Figure 4.6: Velocity vs. time for four different values of wing aspect ratio.

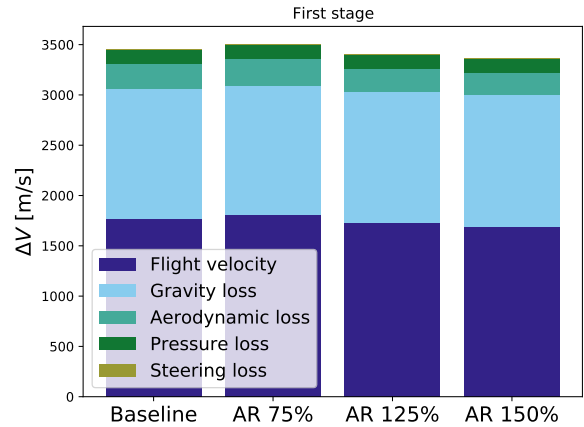
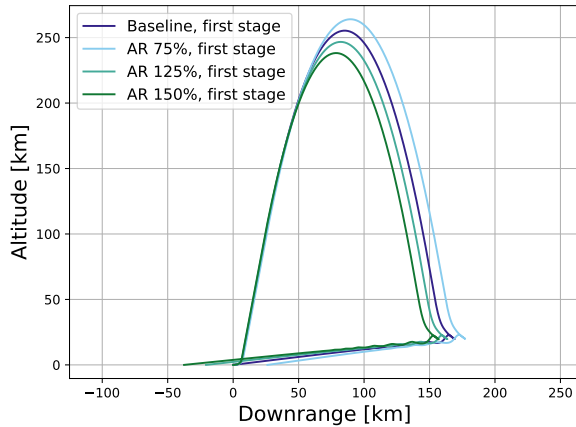


Figure 4.7: Velocity vs. time for four different values of wing aspect ratio. Figure 4.8: Delta-V budget of first stage vehicle for four different values of wing aspect ratio.

Table 4.2: Delta-V budget of first stage vehicle for four different values of wing aspect ratio.

| | | Baseline | AR 75% | AR 125% | AR 150% | | | |
|------------------|-------|----------|--------|---------|---------|-------|--------|-------|
| Flight velocity | [m/s] | 1768.3 | 1808.3 | 2.3% | 1729.5 | -2.2% | 1690.5 | -4.4% |
| Gravity loss | [m/s] | 1297.9 | 1285.1 | -1.0% | 1304.4 | 0.5% | 1308.6 | 0.8% |
| Aerodynamic loss | [m/s] | 243.7 | 263.1 | 8.0% | 230.0 | -5.6% | 219.9 | -9.8% |
| Pressure loss | [m/s] | 138.7 | 141.8 | 2.2% | 136.7 | -1.5% | 135.2 | -2.5% |
| Steering loss | [m/s] | 7.1 | 7.5 | 4.9% | 7.0 | -1.8% | 6.9 | -3.1% |
| Total ΔV | [m/s] | 3455.8 | 3505.8 | 1.4% | 3407.6 | -1.4% | 3361.2 | -2.7% |

4.2.2. Wing surface area

Two cases of either decreased or increased wing surface area have been analysed, whilst keeping the aspect ratio constant. The results of these analyses are shown in Figures 4.9 to 4.11. Again, increased wing surface area increases the wing mass, and therefore, makes it more difficult for the upper stage to reach orbit. From the delta-V budget in Figure 4.12, it can be observed that increasing the wing surface area reduces the aerodynamic losses, meaning that this did not lead to reduced flight velocity. Also, the wing surface area influences the amount of gliding range available after re-entry.

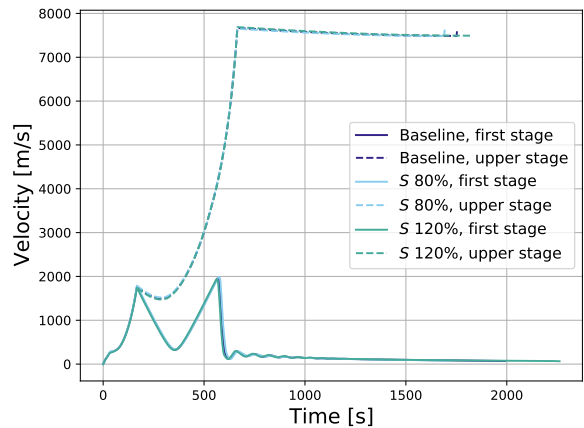
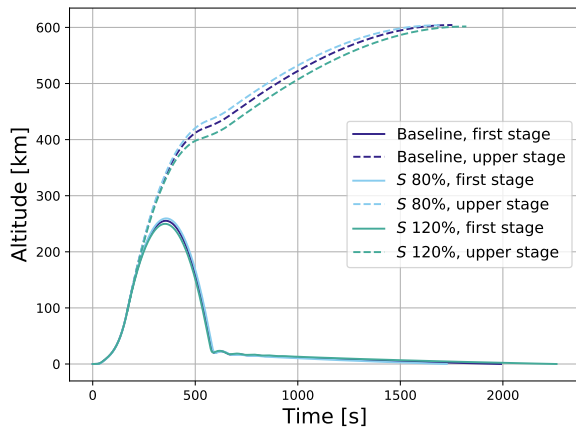


Figure 4.9: Altitude vs. time for three different values of wing surface area. Figure 4.10: Velocity vs. time for three different values of wing surface area.

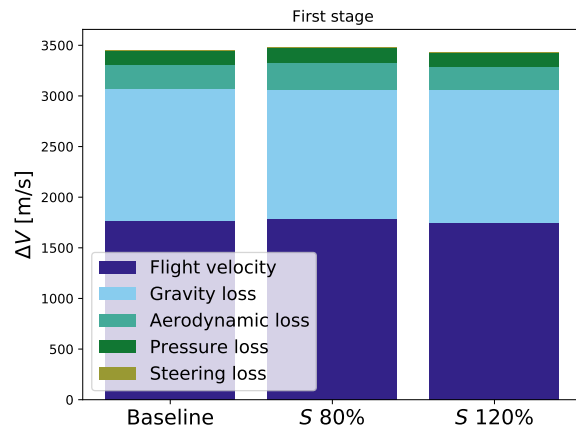
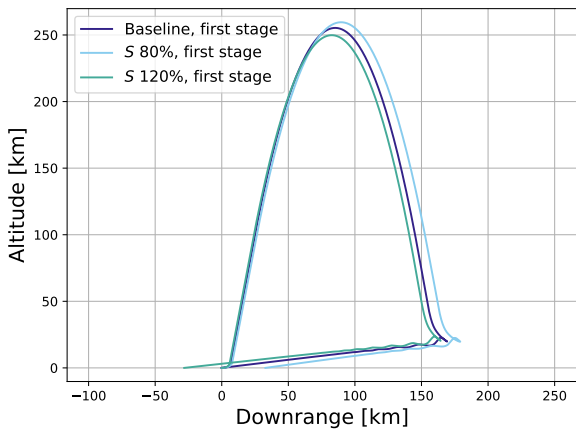


Figure 4.11: Velocity vs. time for three different values of wing surface area. Figure 4.12: Delta-V budget of first stage vehicle for three different values of wing surface area.

Table 4.3: Delta-V budget of first stage vehicle for three different values of wing surface area

| | | Baseline | S 80% | S 120% |
|------------------|-------|----------|--------|--------|
| Flight velocity | [m/s] | 1768.3 | 1790.4 | 1.2% |
| Gravity loss | [m/s] | 1297.9 | 1271.8 | -2.0% |
| Aerodynamic loss | [m/s] | 243.7 | 269.6 | 10.6% |
| Pressure loss | [m/s] | 138.7 | 143.3 | 3.3% |
| Steering loss | [m/s] | 7.1 | 7.7 | 8.1% |
| Total ΔV | [m/s] | 3455.8 | 3482.8 | 0.8% |

4.2.3. Leading edge sweep angle

The variation of sweep angle shows similar responses in trajectory, as shown in Figures 4.13 to 4.15. An increase of sweep angle produces a heavier wing, which reduces the flight velocity delivered by the first stage. As a result of this, the vehicle re-enters the atmosphere at a lower downrange, and therefore has to glide back to the runway a smaller distance. As can be seen from the fact that the slope of the gliding segment in Fig. 4.15 is equal for all cases of sweep, the glide ratio is not sensitive to changes in sweep angle in the analysed range.

However, a vehicle with lower sweep angle retains more altitude after re-entry, and therefore can glide back a longer distance, even though the glide ratio is the same. For this reason, the three compared are all able to glide back to the take-off and landing runway. In contrast to the two sensitivity analyses on aspect ratio and wing surface area, it seems that both increasing and decreasing the wing sweep angle seems to increase the aerodynamic losses, as shown in the delta-V budget of Figure 4.16 and Table 4.4.

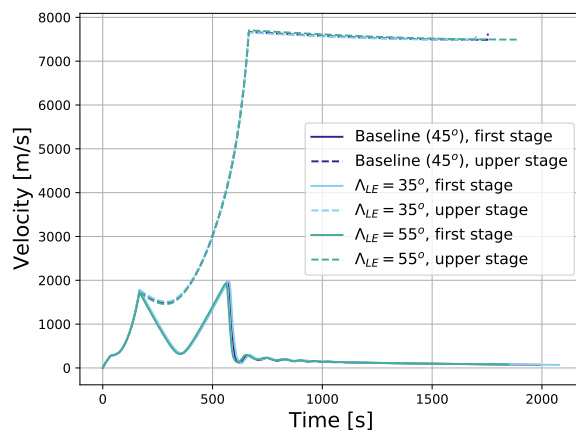
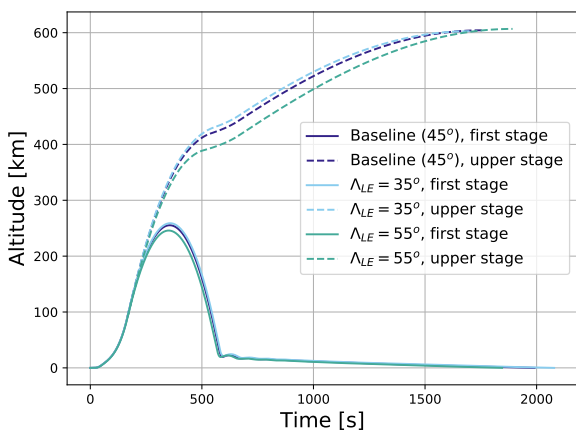


Figure 4.13: Altitude vs. time for three different values of sweep angle. Figure 4.14: Velocity vs. time for three different values of sweep angle.

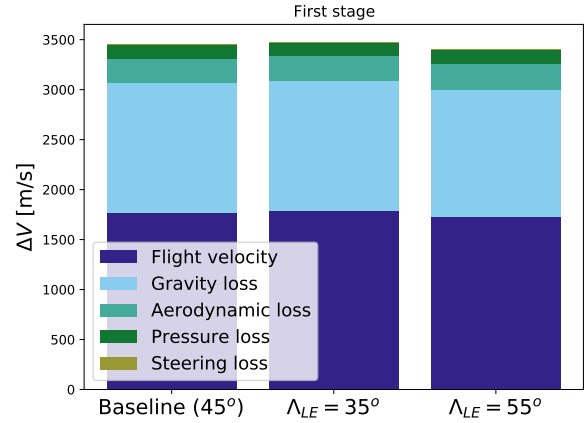
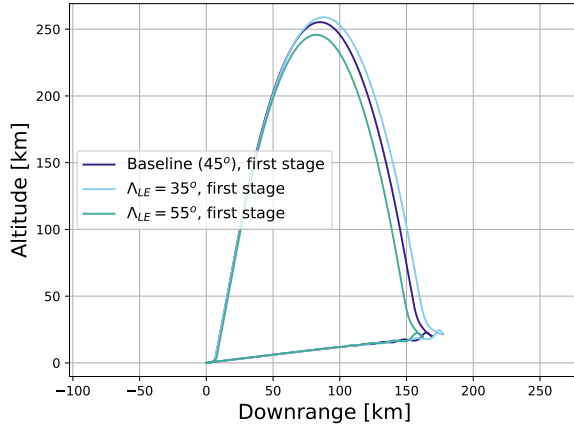


Figure 4.15: Velocity vs. time for three different values of sweep angle. Figure 4.16: Delta-V budget of first stage vehicle for three different values of sweep angle.

Table 4.4: Delta-V budget of first stage vehicle for three different values of sweep angle

| | | Baseline | $\Lambda_{LE} = 35^\circ$ | | $\Lambda_{LE} = 55^\circ$ | |
|------------------|-------|-----------------|---------------------------|-------|---------------------------|-------|
| Flight velocity | [m/s] | 1768.3 | 1785.7 | +1.0% | 1727.4 | -2.3% |
| Gravity loss | [m/s] | 1297.9 | 1302.1 | +0.3% | 1277.0 | -1.6% |
| Aerodynamic loss | [m/s] | 243.7 | 245.1 | +0.6% | 253.7 | +4.1% |
| Pressure loss | [m/s] | 138.7 | 138.5 | -0.2% | 141.0 | +1.6% |
| Steering loss | [m/s] | 7.1 | 7.1 | -0.1% | 7.4 | +2.9% |
| Total ΔV | [m/s] | 3455.8 | 3478.6 | +0.7% | 3406.4 | -1.4% |

4.3. Sensitivity to trajectory parameters

The trajectory model requires inputs on the orbit to be targeted, the conditions at staging and the location of the take-off and landing runway. Of these input parameters, the flight path angle at staging and the location of take-off and landing are varied in this sensitivity analysis.

4.3.1. Flight path angle at staging

The baseline scenario features a trajectory with a flight path angle of 79° at staging. This parameter has been varied to 75° and 70° , and the resulting trajectories are shown in Figures 4.17 and 4.18. As can be expected, reducing the flight path angle results in a less steep first stage trajectory, and a re-entry into the atmosphere at a point further away from the take-off and landing distance. Since the vehicle's gliding capabilities are unaffected, it is now not able to glide back all the way to the runway.

On the other hand, improvements can be observed for the upper stage vehicle, as shown by the delta-V budget of Figure 4.19. The trajectories with lower staging flight path angle spend less time at a high flight path angle and ultimately experience lower gravity losses. As a result, the total required delta-V is slightly reduced, which reduces the ratio of upper stage propellant to dry mass.

This sensitivity analysis highlights the conflict between the requirements of putting the payload in the target orbit, and the first stage that must land at the same take-off and landing runway. Improved gliding performance of the first stage vehicle can thus result in reduced gravity losses of the upper stage.

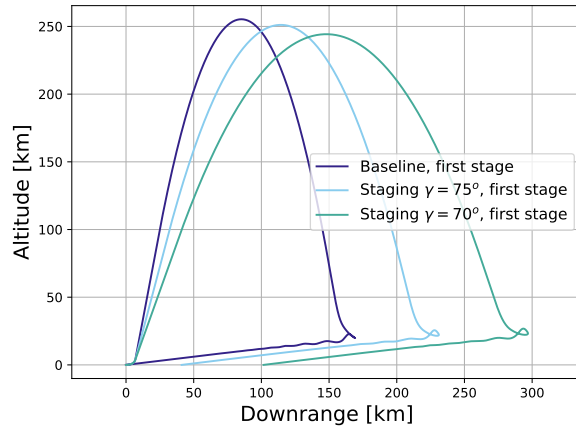
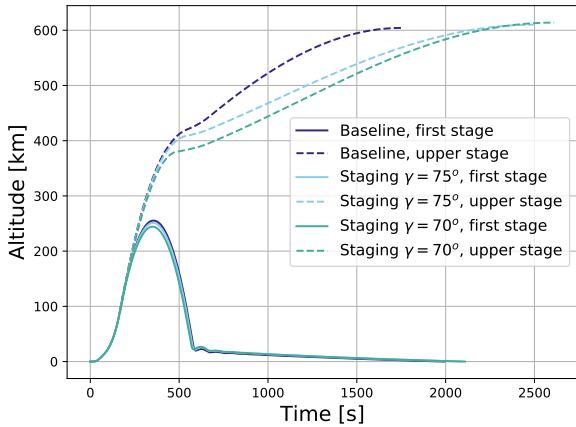


Figure 4.17: Altitude vs. time for three different values of staging flight path angle.

Figure 4.18: Velocity vs. time for three different values of staging flight path angle.

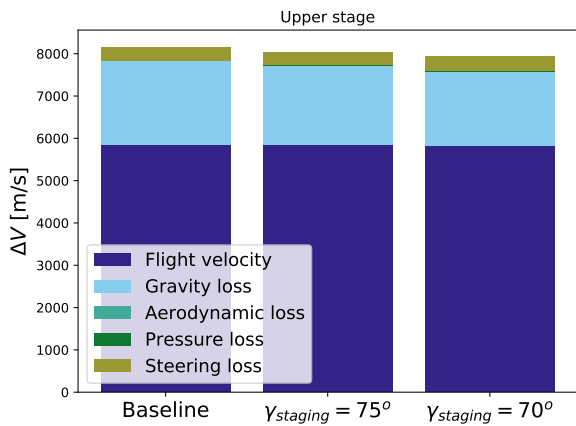


Figure 4.19: Delta-V budget of upper stage vehicle for three different values of staging flight path angle.

Table 4.5: Delta-V budget of upper stage vehicle for three different values of staging flight path angle

| | | Baseline | $\gamma_{\text{staging}} = 75^\circ$ | | $\gamma_{\text{staging}} = 70^\circ$ | |
|------------------|-------|----------|--------------------------------------|-------|--------------------------------------|--------|
| Flight velocity | [m/s] | 5860.9 | 5847.2 | -0.2% | 5828.7 | -0.5% |
| Gravity loss | [m/s] | 1971.8 | 1883.9 | -4.5% | 1761.4 | -10.7% |
| Steering loss | [m/s] | 318.4 | 290.6 | -8.7% | 351.2 | 10.3% |
| Total ΔV | [m/s] | 8151.1 | 8021.7 | -1.6% | 7941.2 | -2.6% |

4.3.2. Spaceport location

The second sensitivity analysis to trajectory model parameters is the variation of the spaceport location, i.e. where the take-off and landing runway is located on Earth. Five locations were selected, spread over various latitudes on both the northern and southern hemisphere, and at various elevations. These locations determine the starting condition for the launching vehicle in terms of the experienced atmosphere and the experienced inertial velocity, due to rotation of the earth. The five selected spaceport locations are listed in Table 4.6, along with their respective values of latitude and elevation.

Table 4.6: Spaceport locations used in sensitivity analysis.

| Location | Latitude [°] | Elevation [m] |
|-------------------------------|--------------|---------------|
| Oamaru Airport (New-Zealand) | -45 | 30 |
| Pukaki Airport (New-Zealand) | -44.2 | 1575 |
| Rostock-Laage (Germany) | 53.9 | 42 |
| Spaceport Colorado (USA) | 39.8 | 1680 |
| Midland Air & Spaceport (USA) | 31.9 | 875 |

The resulting trajectories from these locations are shown in the graphs of Figures 4.20 to 4.22. It shows that the elevation has an effect on the trajectories. Launching from an elevated spaceport, means that the vehicle experiences less of the atmosphere and thus lower aerodynamic losses. This causes a larger velocity to be achieved at staging, and therefore the first stage vehicle re-enters the atmosphere at a larger downrange. Because of this, the vehicles cannot make it completely back to the take-off and landing runway.

The variations of latitude seem to have very little effect, when targeting polar orbits. The variation of initial inertial velocity due to the changed latitude thus has little consequence to the trajectories, and is likely because this variation in velocity is small compared to the velocity of the target orbit.

First stages that are launched from elevated spaceports thus have lower aerodynamic losses and deliver more delta-V to the upper stage. These upper stages have to deliver less delta-V, as can be seen by the delta-V budget of Figure 4.23 and Table 4.7. This means that the propellant to dry mass ratio of the upper stage can be reduced to reach the same orbit.

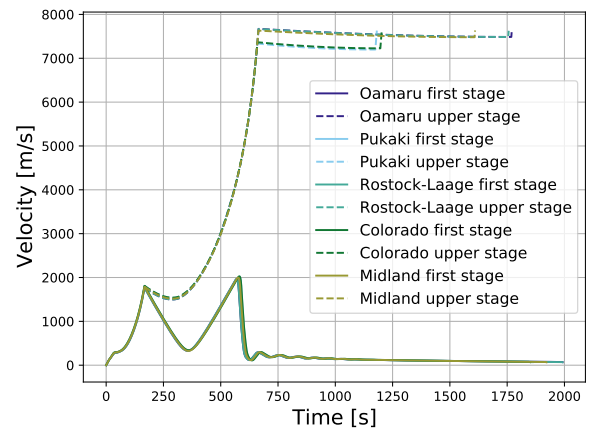
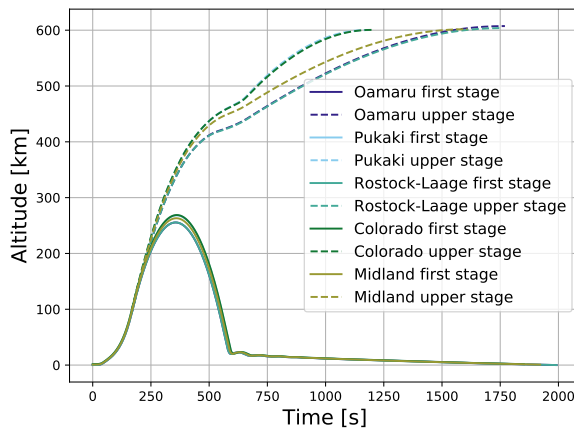


Figure 4.20: Altitude vs. time for five different spaceport locations.

Figure 4.21: Velocity vs. time for five different spaceport locations.

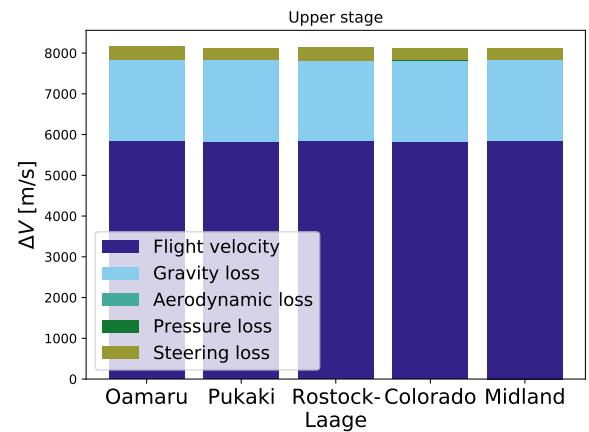
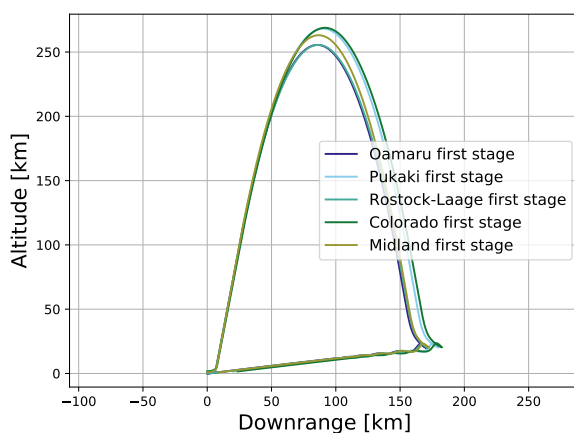


Figure 4.22: Velocity vs. time for five different spaceport locations.

Figure 4.23: Delta-V budget of upper stage vehicle for five different spaceport locations.

Table 4.7: Delta-V budget of upper stage vehicle for five different spaceport locations.

| | | Oamaru | Pukaki | Rostock-Laage | Colorado | Midland |
|------------------|-------|---------------|---------------|----------------------|-----------------|----------------|
| Flight velocity | [m/s] | 5858.0 | 5823.0 | 5857.3 | 5821.1 | 5841.7 |
| Gravity loss | [m/s] | 1972.6 | 2008.6 | 1964.2 | 2001.0 | 2002.1 |
| Steering loss | [m/s] | 319.7 | 292.9 | 322.9 | 293.6 | 271.4 |
| Total ΔV | [m/s] | 8150.2 | 8124.5 | 8144.3 | 8115.7 | 8115.2 |

4.4. Sensitivity to model uncertainty

Validation of the separate parts of the vehicle model, as described in Section 2.5, has shown that uncertainty in the estimated performance or characteristics of the vehicle may be present. This was mainly the case for the vehicle dry mass estimation and in the sub- and supersonic drag estimation. Therefore, a sensitivity analysis has been performed to investigate the effects of these modelling uncertainties. This indicates where more effort should be done in improving the developed model and reducing the uncertainty.

4.4.1. Uncertainty in mass model

In the validation process of the mass model (Subsec. 2.5.2), it was found that the estimation of the stage dry mass has a mean relative error of -4%, i.e. underestimation of the vehicle stage dry mass. Therefore, in this sensitivity analysis, the calculated dry mass has been both increased and decreased by 4%. Since the launching vehicle consists of two stages, the analysis has been done on both stages separately.

The resulting trajectory of the vehicle, of which the first stage dry mass has been varied, is shown in Figures 4.24 to 4.26. The analysis of the variation of upper stage dry mass is shown in Figures 4.27, to 4.29.

An increased first stage dry mass results in a lower achieved flight velocity at staging. This means a lower starting velocity of the upper stage trajectory and causes the upper stage to fail to achieve orbital velocity. In case of the lower flight velocity at staging, the re-entry into the atmosphere occurs at a lower downrange. One might expect that in this case it becomes easier for the vehicle to glide back to the runway. However, the heavier vehicle retains less altitude after re-entry, and the gliding segments of the individual cases end at approximately the same location.

When the dry mass of the upper stage vehicle is increased by 4%, smaller variations are observed in the upper stage trajectory. The first stage trajectory in this case, as can be seen in Figure 4.29, is hardly affected by the variations in upper stage dry mass.

From this analysis it may be concluded that it is particularly important to have a low uncertainty in the dry mass estimation of the first stage vehicle, as it has an effect on both the success of reaching the target orbit, as well as on the gliding range.

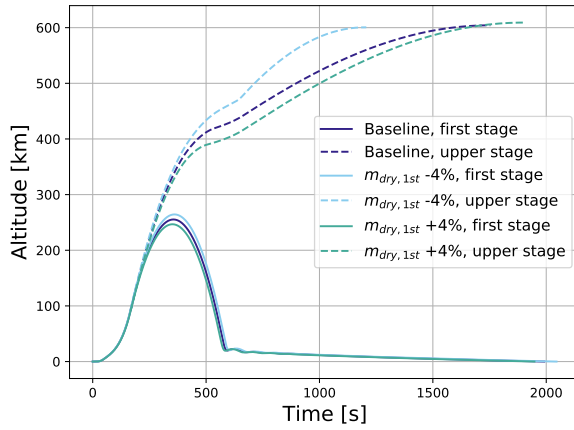


Figure 4.24: Altitude vs. time for variations of first stage dry mass.

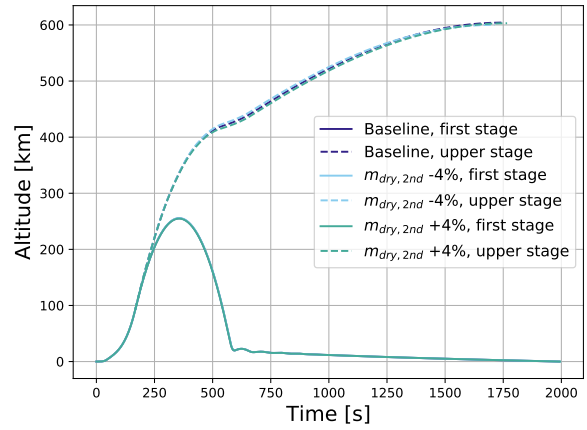


Figure 4.27: Altitude vs. time for variations of upper stage dry mass.

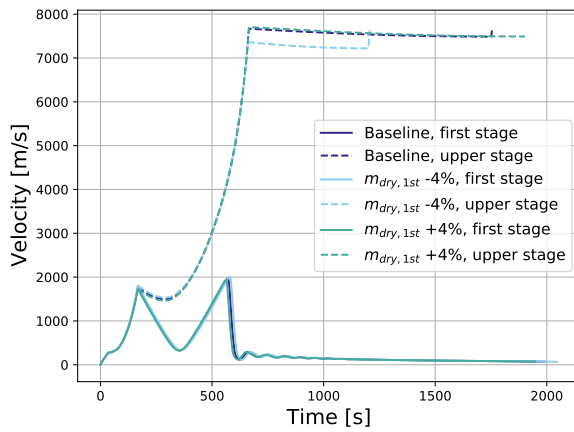


Figure 4.25: Velocity vs. time for variations of first stage dry mass.

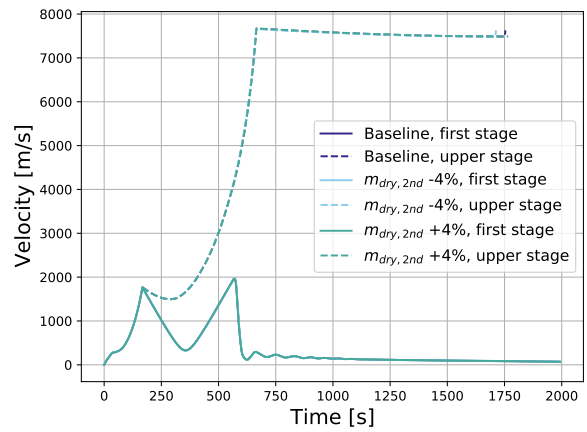


Figure 4.28: Velocity vs. time for variations of upper stage dry mass.

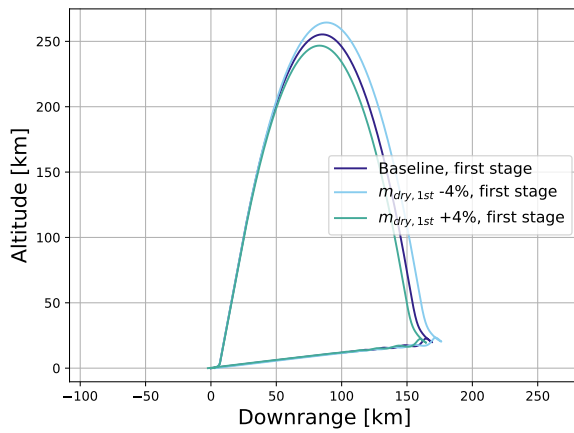


Figure 4.26: Altitude vs. downrange for variations of first stage dry mass.

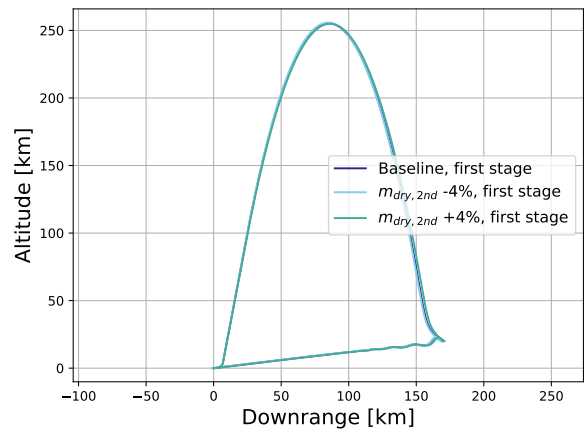


Figure 4.29: Altitude vs. downrange for variations of upper stage dry mass.

4.4.2. Uncertainty in subsonic drag estimation

To emulate variations in the estimation of the subsonic aerodynamic performance of the vehicle, correction factors have been introduced on the estimated drag values. Since the estimated drag is built up with a zero-lift and a lift-induced component, each using their respective modelling methods, they have been amplified individually. Figures 4.30 to 4.32 show the results of the analyses, where the subsonic zero-lift component is varied, while Figures 4.33 to 4.35 contain the simulations with sensitivities to the lift-induced drag.

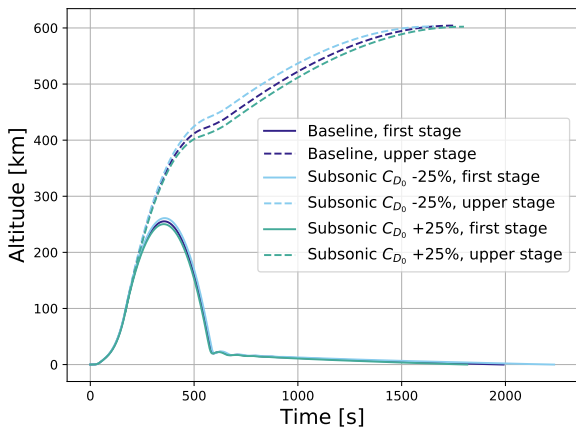


Figure 4.30: Altitude vs. time for variations of subsonic zero-lift drag coefficient.

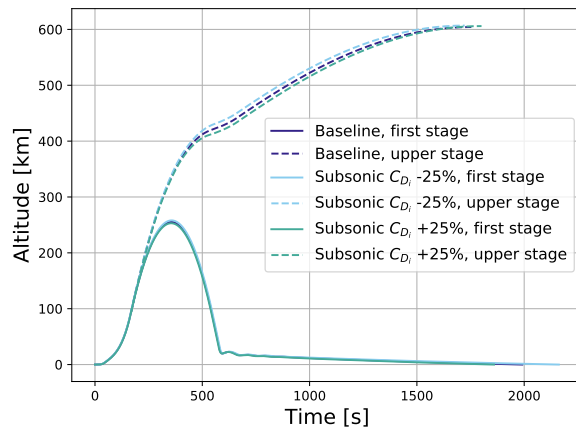


Figure 4.33: Altitude vs. time for variation of subsonic lift-induced drag.

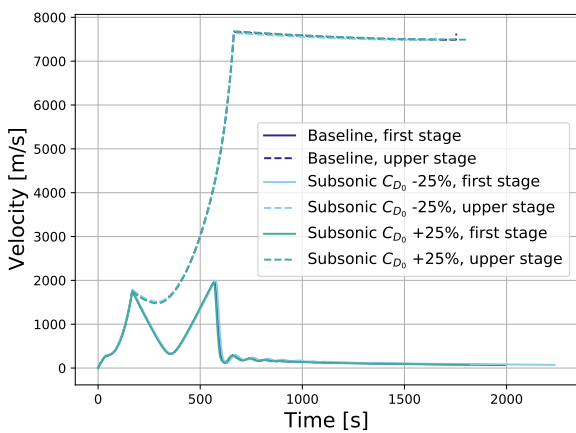


Figure 4.31: Velocity vs. time for variation of subsonic zero-lift drag coefficient.

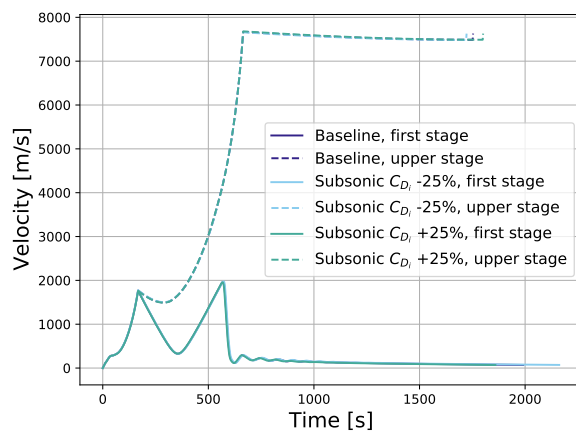


Figure 4.34: Velocity vs. time for variation of subsonic lift-induced drag.

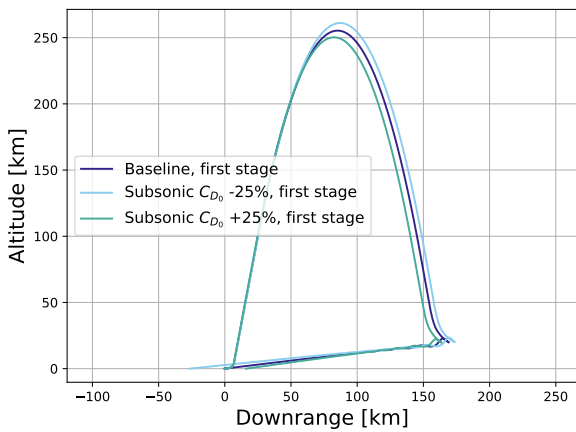


Figure 4.32: Altitude vs. downrange for variation of subsonic zero-lift drag coefficient.

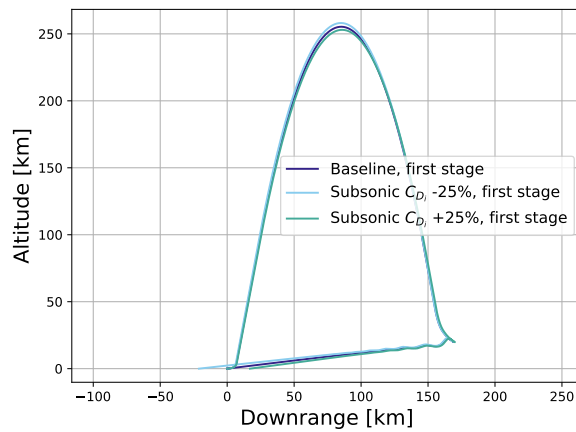


Figure 4.35: Altitude vs. downrange for variation of subsonic lift-induced drag.

It can be observed that the variations in zero-lift drag experienced by the first stage vehicle has some effect on the upper stage trajectory, which fails to reach orbital velocities with increased drag. It also has an effect on the first stage return trajectory, as the changes in zero-lift drag have both an effect on the downrange at atmospheric re-entry and on the gliding ratio.

The lift-induced drag estimation seems to be lower consequence to the ascent trajectory, which can be explained by the fact that during ascent the vehicle flies only for a short duration at subsonic speeds and also

at a relatively low angles of attack. During the return trajectory, the lift-induced drag is more important as it directly influences the glide ratio that can be achieved.

4.4.3. Uncertainty in supersonic drag estimation

Also for the supersonic drag estimation, factors have been introduced on the zero-lift and the lift-induced drag individually, to investigate the response of the trajectory to these parts of the aerodynamic model. The results of the supersonic zero-lift drag sensitivity analysis are shown in Figures 4.36, 4.37 and 4.40. For the lift-induced drag, the results can be found in Figures 4.38, 4.39 and 4.41.

One can observe that the supersonic zero-lift drag estimation is mainly important for the ascent trajectory. It does also affect the return trajectory, but interestingly, variation of downrange at re-entry is compensated by the variation of altitude retained after re-entry.

As for the ascent trajectory, it seems that it is not sensitive to changes in supersonic lift-induced drag. This type of drag does affect the return trajectory. Although the gliding occurs at mostly subsonic speeds, the supersonic lift-induced drag does play a role in the amount of altitude available for gliding after re-entry.

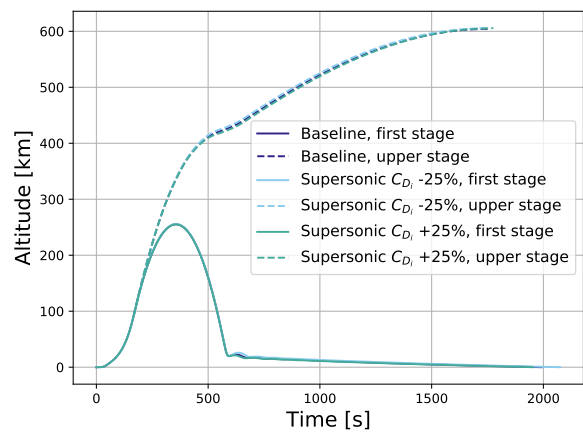
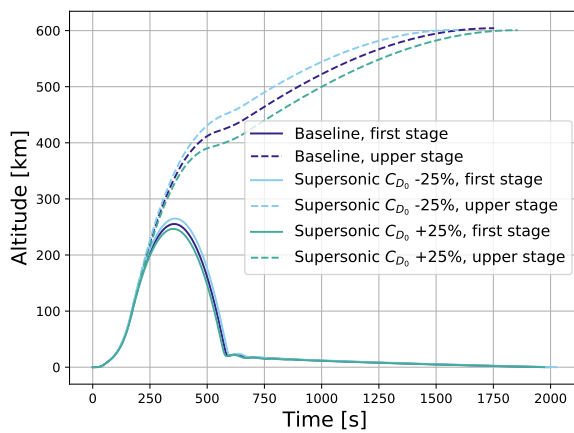


Figure 4.36: Altitude vs. time for variations of supersonic zero-lift drag coefficient.

Figure 4.38: Altitude vs. time for variation of supersonic lift-induced drag.

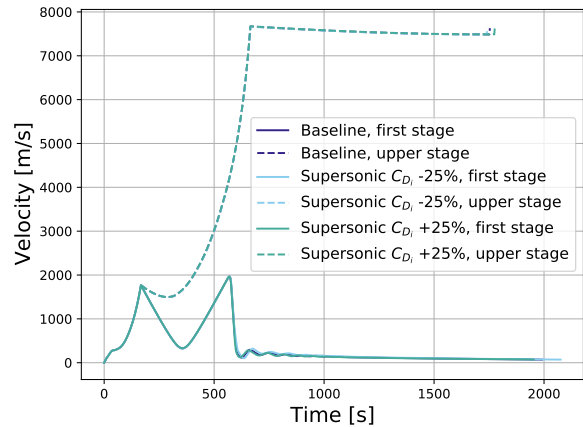
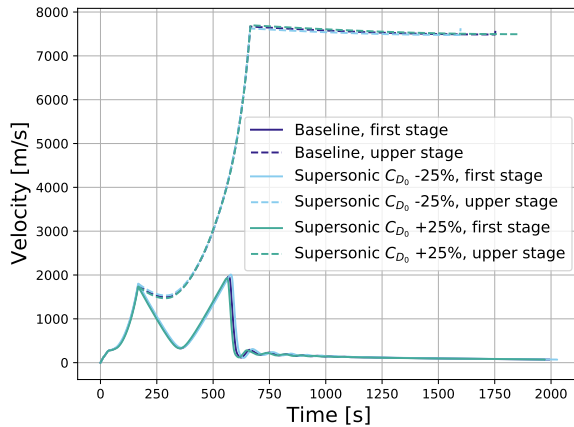


Figure 4.37: Velocity vs. time for variation of supersonic zero-lift drag coefficient.

Figure 4.39: Velocity vs. time for variation of supersonic lift-induced drag.

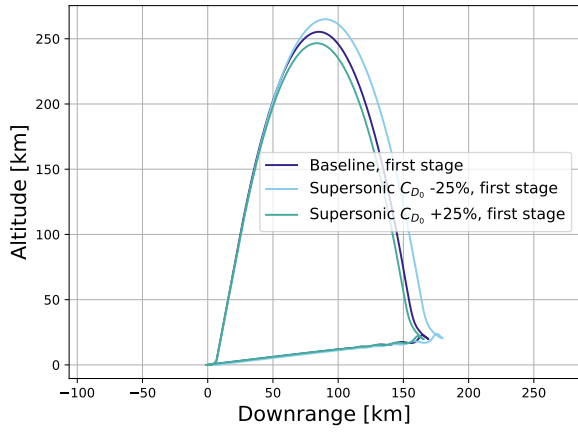


Figure 4.40: Altitude vs. downrange for variation of supersonic zero-lift drag coefficient.

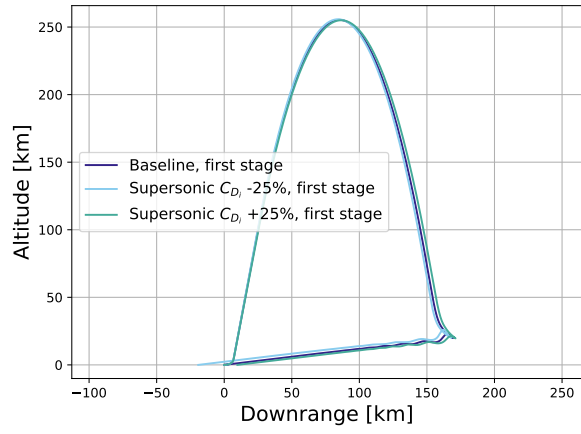


Figure 4.41: Altitude vs. downrange for variation of supersonic lift-induced drag.

5

Case studies

To identify areas in the vehicle design that have a significant impact on the mission performance, a number of case studies have been performed. By looking into the different disciplines within the vehicle model (described in Ch. 2), the mechanisms in which the mission performance is affected by the design parameters can be recognized. In doing so, also cross-coupling between the design of the first and upper stage and their trajectories can be examined. Four case studies were considered and described in this chapter, which are an alternative wing design in Sec. 5.1, an alternative fuselage design and internal arrangement in Sec. 5.2, a differently shaped first stage ascent trajectory in Sec. 5.3 and finally, a rocket-propelled return trajectory in Sec. 5.4.

5.1. Alternative Wing Concept

In the process of establishing a baseline design and the sensitivity analyses in Chapter 4, it was found that gliding range of the first stage vehicle is constraining the design of the upper stage vehicle. The gliding range constrains the maximum amount of delta-V that can be delivered by the first stage vehicle. If the first stage vehicle delivers more velocity to the upper stage, the first stage re-enters the atmosphere at such a distance from the runway that it simply cannot glide back. The upper stage must deliver the remaining delta-V, and thus the gliding range also dictates the minimum upper stage delta-V. The gliding range is driven by the aircraft's glide ratio, and thus it can be said that there is a link between the aerodynamic efficiency and the upper stage propellant mass fraction. The large quantity of delta-V that must be delivered by the upper stage drives the design of the upper stage vehicle to infeasible proportions, in terms of the propellant mass fraction.

The purpose of this case study is to improve on the gliding performance with an alternative wing planform. The improved gliding range should allow the first stage vehicle to deliver more velocity, and the upper stage less velocity. The planform used in this case study is altered from the baseline design, and inspired by the modified arrow wing proposed by Mason [30]. Although the modified arrow wing was proposed in the context of supersonic transport aircraft, it is also relevant for winged reusable launching vehicles, as it seeks to balance between low speed and high speed performance. In principle, two modifications are added to the baseline wing planform. The first is that an outboard section is added to the wing, with a lower leading edge sweep angle compared to the rest of the wing. This should increase the subsonic aerodynamic efficiency. The second modification is that the inboard section at the trailing edge is 'filled in', such that the trailing edge of this section is unswept. This should increase the structural root chord, and, although stability and trim is outside the scope of this research, should be beneficial for the performance of flaps or control surfaces.

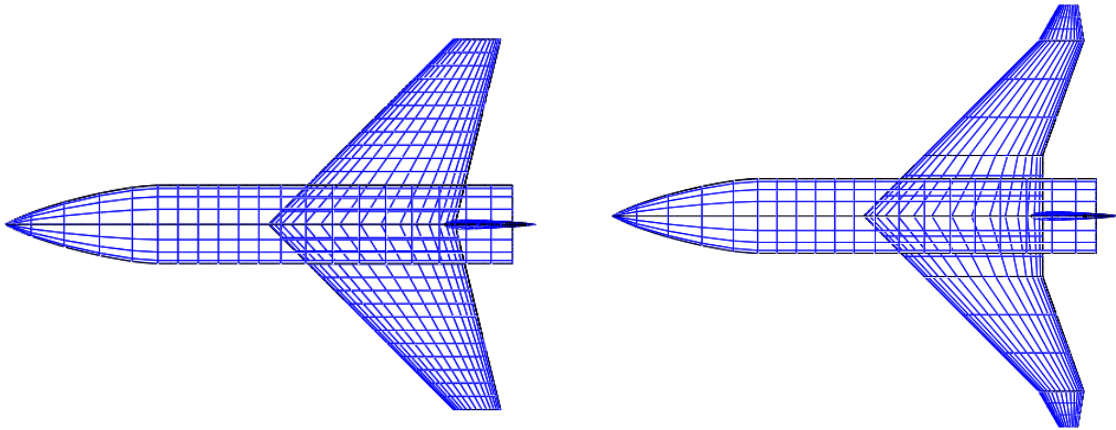


Figure 5.1: Wing planform of baseline design

Using this alternative wing design, a different trajectory was found to meet both the requirements of putting the payload into the required orbit, as well as returning the first stage vehicle to the take-off and landing runway. This trajectory is shown in Figures 5.3 to 5.5. It can be seen that the first stage vehicle is able to glide back from a downrange of roughly 225 km, instead of 170 km. This improved gliding range allowed to increase the flight velocity delivered by the first stage vehicle (Figure 5.6), while the upper stage was required to deliver less flight velocity. This was achieved by increasing the amount of propellant for the first stage, and decreasing for the upper stage, as can be seen in the mass distribution of Table 5.1.

Furthermore, the flight path angle at staging was decreased to 77° and this had a beneficial impact on the gravity losses experienced by the upper stage vehicle, as shown by Figure 5.7. The fact that the vehicle spends less time in a steep trajectory causes a reduction in the amount of potential delta-V lost to counteract gravity.

The upper stage design thus benefits from the first stage design, having increased gliding performance through wing design, in two ways: The division of total required delta-V is spread more evenly over the two stages, and secondly, the upper stage trajectory being less steep results in lower gravity losses. Both mechanisms result in a lower propellant mass fraction of the upper stage, which was reduced from 91.5% to 90.3%.

Table 5.1: Mass distribution of alternative wing concept.

| Stage | Parameter | Baseline | Alternative |
|-------|------------|----------|-------------|
| First | Total mass | 43556 kg | 45266 kg |
| | Dry mass | 6998 kg | 7730 kg |
| | Propellant | 30000 kg | 32000 kg |
| Upper | Total mass | 6558 kg | 5536 kg |
| | Dry mass | 308 kg | 286 kg |
| | Propellant | 6000 kg | 5000 kg |
| | Payload | 250 kg | 250 kg |

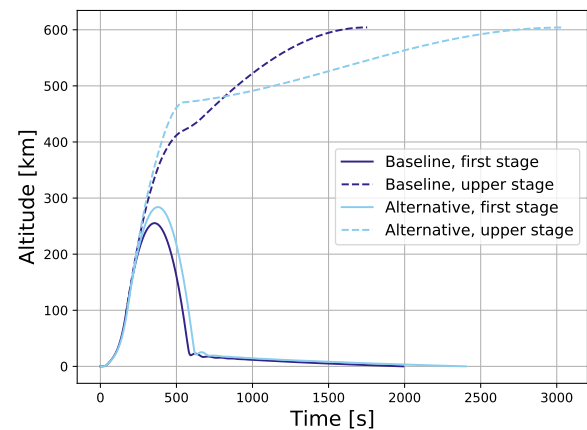


Figure 5.3: Altitude vs. time of alternative wing concept.

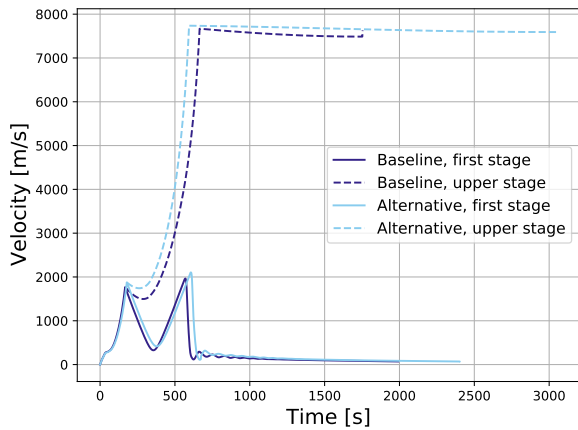


Figure 5.4: Velocity vs. time of alternative wing concept.

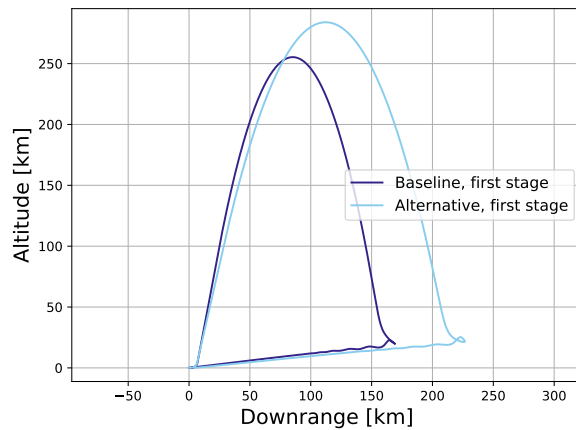


Figure 5.5: Altitude vs. downrange of alternative wing concept.

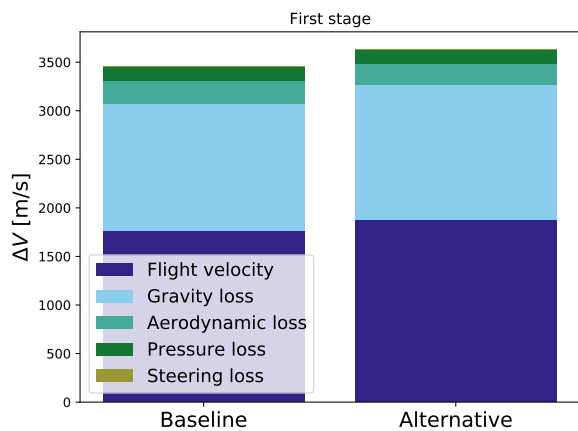


Figure 5.6: First stage Delta-V budget of alternative wing concept.

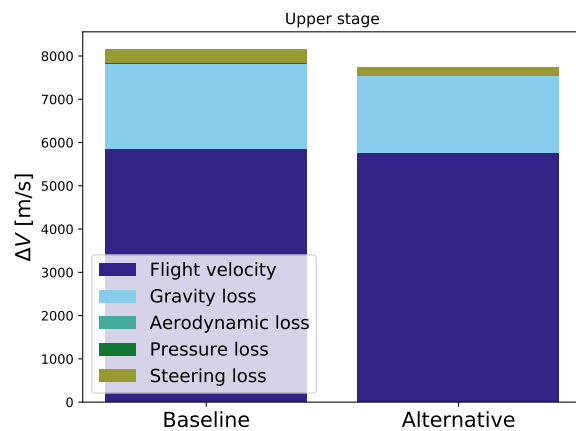


Figure 5.7: Upper stage Delta-V budget of alternative wing concept.

5.2. Alternative Fuselage Concept

Inspired by FESTIP concept, presented by Spies and Kuczera [3] and already shown in Chapter 1, where the upper stage was packaged in the fuselage on top of the first stage propellant tanks, a case study was done on an alternative fuselage concept. This concept, with the upper stage positioned in parallel with the first stage propellant elements, should achieve a lower length to diameter ratio of the fuselage, potentially reducing the structural weight of the fuselage. This packaging should also provide benefits for the in-flight operation of releasing the upper stage from the first stage vehicle, although this is considered outside the scope of this study.

Not only does this change in concept have an effect on the fuselage structural mass, but also on the aerodynamic performance. The change in length to diameter ratio should have an effect on the estimated wave drag due to volume, and the increased base area should increase the experienced base drag.

The build-up of the baseline fuselage package and the parallel fuselage layout were already shown in Figure 2.4 and 2.5, respectively.

Due to the alternative fuselage concept, an increase of drag was expected, which is confirmed by the fact that the aerodynamic losses of the first stage vehicle have increased, shown by the delta-V budgeted in Fig. 5.11. However, the graph of Fig. 5.10 shows that the glide ratio is not significantly affected by the changed fuselage design, as can be deduced from the slopes of the gliding segments being equal. This suggests that primarily the supersonic drag is affected, and the subsonic drag is not sensitive to the alternative fuselage design, which was also seen in the sensitivity analysis of Sec. 4.4.

The mass distribution of the concept with parallel fuselage, compared to the baseline design, is shown in

Table 5.2. It can be seen that the dry mass of the first stage vehicle is reduced significantly. This is caused by the reduction fuselage structural mass, due reduced length to diameter ratio, but also due to the fact that the propellant mass could be reduced, which transfers into more reduction of the dry mass. It should be noted that the mass savings indicated by the vehicle model may be exaggerated. That is because the mass estimating relations, described in Sec. 2.3, were intended for conventional launchers, having each tank connected in series. In other words, potential penalties in weight from stacking the upper stage on top of the first stage propellant tanks are not modelled. Still, the changed fuselage design yields a large reduction in mass and it is worthwhile to investigate the effect of this on the mission performance.

For the return trajectory, shown in Figure 5.10, it can be seen that the vehicle is able to glide back from a larger downrange than the baseline design. Since the glide ratio is not increased, the larger gliding range is not actually caused by improved gliding performance. However, a lower dry mass allows the vehicle to retain more altitude after re-entry, and thus more potential energy is available for the gliding segment.

Because of the improved gliding range, a higher velocity could be delivered by the first stage, and the upper stage was required to deliver less flight velocity. Also the flight path angle at staging was decreased to 76° , as a result of the increased gliding range, and this in turn caused a reduction of the gravity losses of both stages. These two effects have allowed the propellant mass fraction to be reduced from 91.5% to 90.4%.

Table 5.2: Mass distribution of parallel fuselage concept.

| Stage | Parameter | Baseline | Parallel |
|-------|------------|----------|----------|
| First | Total mass | 43556 kg | 32763 kg |
| | Dry mass | 6998 kg | 5234 kg |
| | Propellant | 30000 kg | 22000 kg |
| Upper | Total mass | 6558 kg | 5529 kg |
| | Dry mass | 308 kg | 279 kg |
| | Propellant | 6000 kg | 5000 kg |
| | Payload | 250 kg | 250 kg |

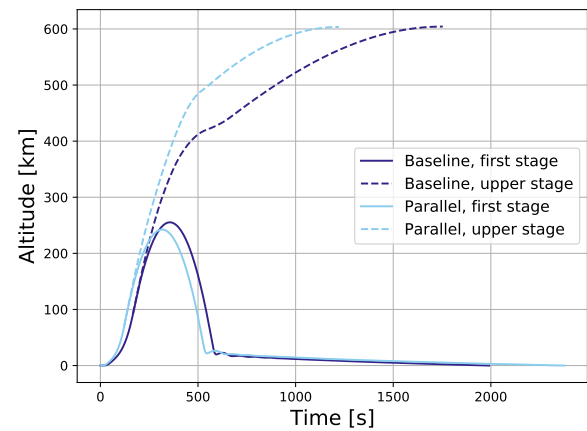


Figure 5.8: Altitude vs. time of parallel fuselage concept.

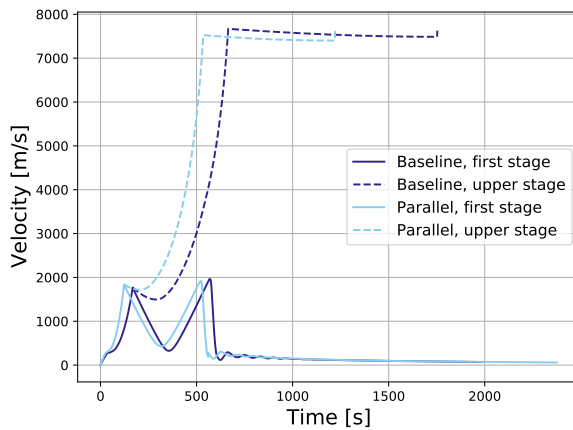


Figure 5.9: Velocity vs. time of parallel fuselage concept.

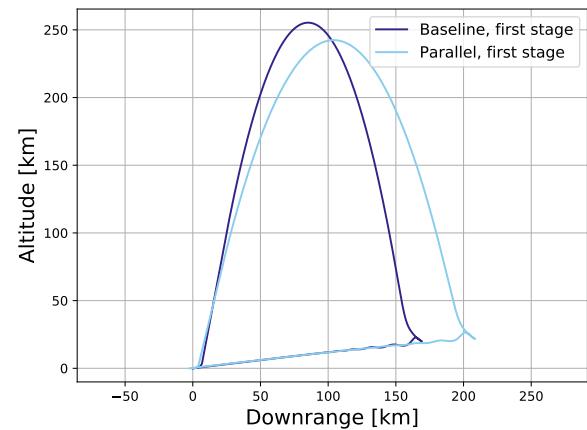


Figure 5.10: Altitude vs. downrange of parallel fuselage concept.

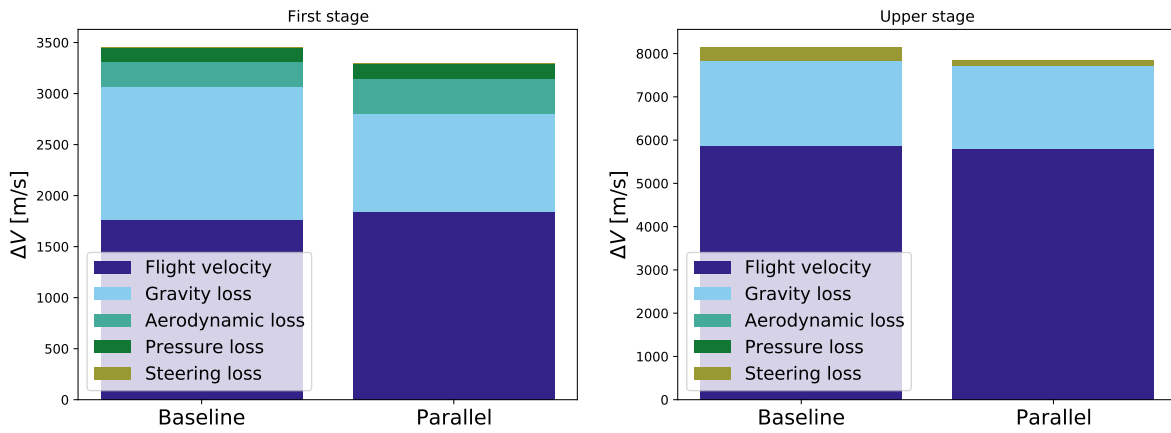


Figure 5.11: First stage Delta-V budget of parallel fuselage concept. Figure 5.12: Upper stage Delta-V budget of parallel fuselage concept.

5.3. Reverse take-off

The purpose of this case study is to reduce the amount of downrange covered by the first stage vehicle, before it can perform a glideback maneuver. Although most of the downrange is covered during the parabolic coast, also the ascent maneuver produces approximately 25 km of downrange. The direction of the ascent maneuver was reversed, such that there is a negative downrange after ascent. The ascent is initially done at a low flight path angle of 35°, until it reaches a certain altitude, in this case study selected as 16 km. It then pitches up over vertically, until it reaches a steeper flight path angle of 76°, but now in positive downrange direction. To understand the concept of reverse take-off better, one can observe the simulated trajectory in Figure 5.13.

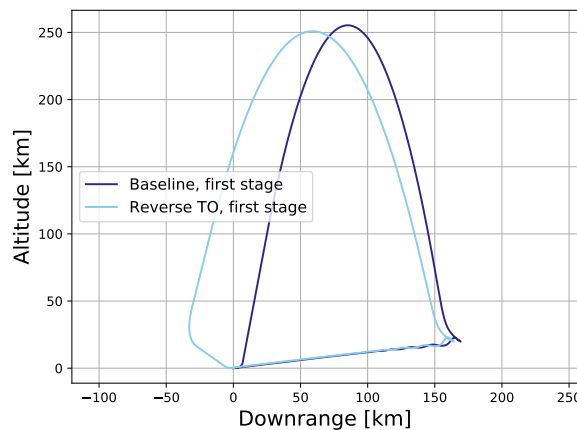


Figure 5.13: Altitude vs. downrange of reverse take-off concept.

Although this case study also does not include any engineering optimization, it proved to be difficult to find significant savings of downrange. The reversing of the take-off direction did not offer benefits in terms of downrange without the shallow initial ascent at approximately 35° flight path angle. The shallow initial ascent resulted in a longer path through the thicker atmosphere, which caused a high aerodynamic loss of delta-V, which can be seen in Fig. 5.16. The pitching over also caused relatively high steering losses for the first stage vehicle. This all caused the propellant mass and the total mass of the first stage vehicle to be increased significantly. Despite all this, a small improvement was gained for the upper stage vehicle, due to the fact that a lower flight path angle at staging of 76° resulted in reduced gravity and steering losses, as shown in Fig. 5.17. This allowed the propellant mass fraction of the upper stage to be reduced slightly, from 91.5% to 91.0%.

Table 5.3: Mass distribution of reverse take-off concept.

| Stage | Parameter | Baseline | Reverse TO |
|-------|------------|----------|------------|
| First | Total mass | 43556 kg | 50098 kg |
| | Dry mass | 6998 kg | 7851 kg |
| | Propellant | 30000 kg | 36200 kg |
| Upper | Total mass | 6558 kg | 6047 kg |
| | Dry mass | 308 kg | 297 kg |
| | Propellant | 6000 kg | 5500 kg |
| | Payload | 250 kg | 250 kg |

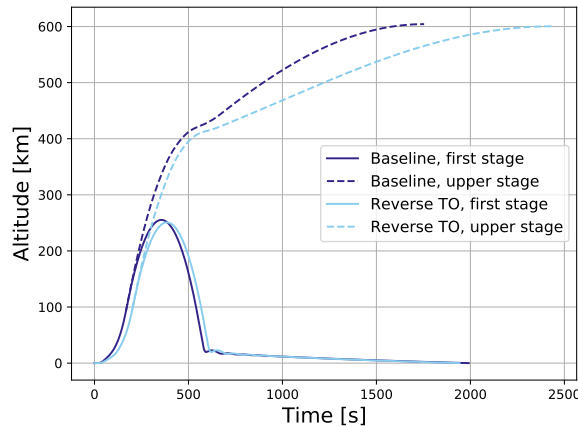


Figure 5.14: Altitude vs. time of reverse take-off concept.

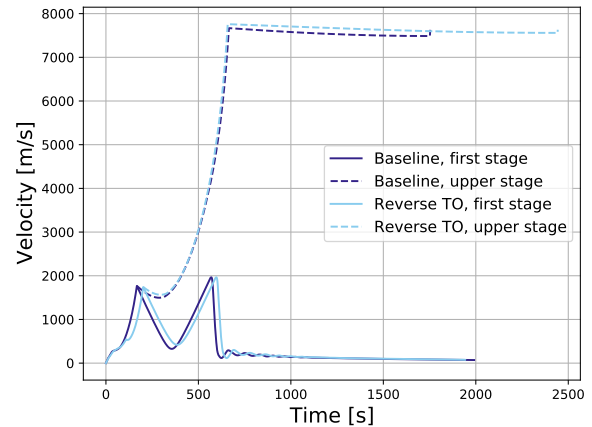


Figure 5.15: Velocity vs. time of reverse take-off concept.

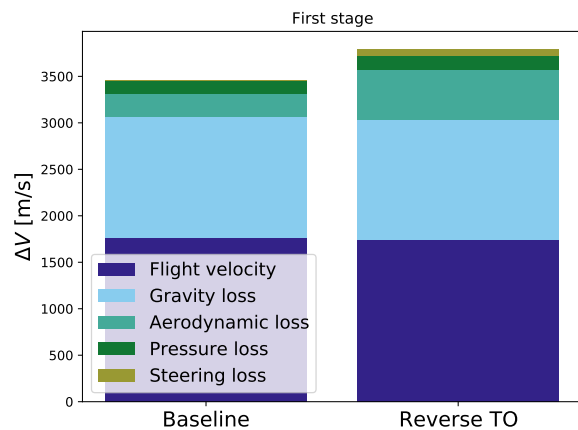


Figure 5.16: First stage Delta-V budget of reverse take-off concept.

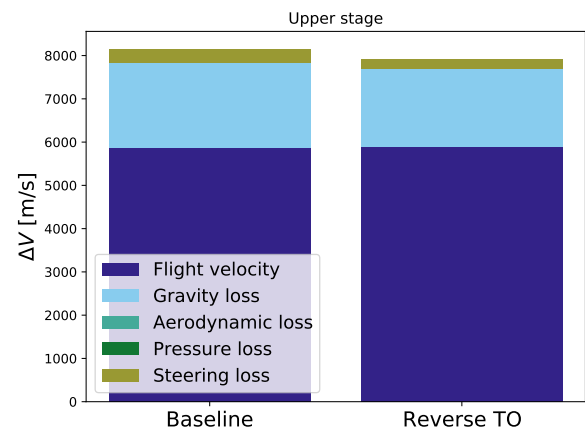


Figure 5.17: Upper stage Delta-V budget of reverse take-off concept.

5.4. Boostback

In the final case study a boost from the rocket engines is applied to the first stage at the beginning of the glide segment. The boost should increase the effective 'gliding' range and is applied at the beginning of the gliding segment, when the aircraft is still at high speed, skipping on the atmosphere. The boost should enhance these skips, during which a lot of downrange is recovered. Two cases were analysed, with 2% and 4% of the first stage propellant reserved for this boost in the return trajectory.

Because propellant is reserved for the return, the total amount of propellant is increased, such that the velocity achieved at staging remains approximately the same for all cases, as can be seen from Figure 5.21. The flight path angle at staging was reduced to 76° for 2% of reserve propellant, and to 73° for 4% reserve. The apogee of the first stage trajectory is therefore lower, and results in a higher downrange at re-entry. The boosting during the glide segment allows to overcome this increase in downrange, with 2% of propellant reserve yielding approximately 40 km of extra gliding range.

The lower flight path angles also resulted in lower gravity and steering losses of the upper stage trajectory, as can be seen in Figure 5.23. This gave the possibility to reduce the amount of propellant for the upper stage, despite delivering the same flight velocity, and gave a reduction of the upper stage propellant mass fraction from 91.5% to 90.3% (in case of a propellant reserve of 4%).

Table 5.4: Mass distribution of boostback concept.

| Stage | Parameter | Baseline | 2% Reserve | 4% Reserve |
|-------|------------|----------|------------|------------|
| First | Total mass | 43556 kg | 44355 kg | 46415 kg |
| | Dry mass | 6998 kg | 7108 kg | 7379 kg |
| | Propellant | 30000 kg | 31200 kg | 33500 kg |
| Upper | Total mass | 6558 kg | 6047 kg | 5536 kg |
| | Dry mass | 308 kg | 297 kg | 286 kg |
| | Propellant | 6000 kg | 5500 kg | 5000 kg |
| | Payload | 250 kg | 250 kg | 250 kg |

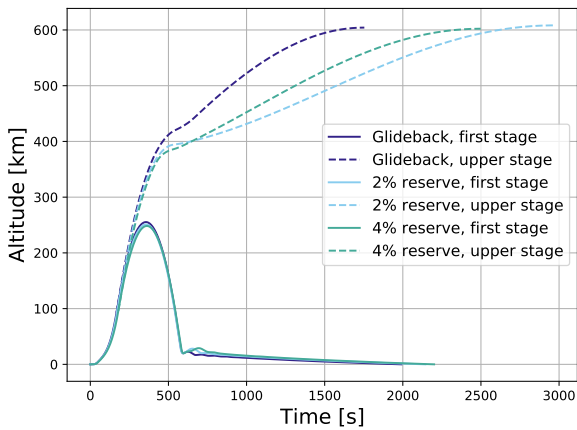


Figure 5.18: Altitude vs. time of boostback concept.

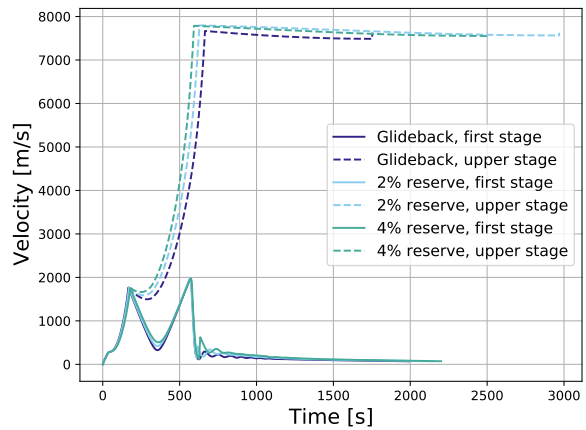


Figure 5.19: Velocity vs. time of boostback concept.

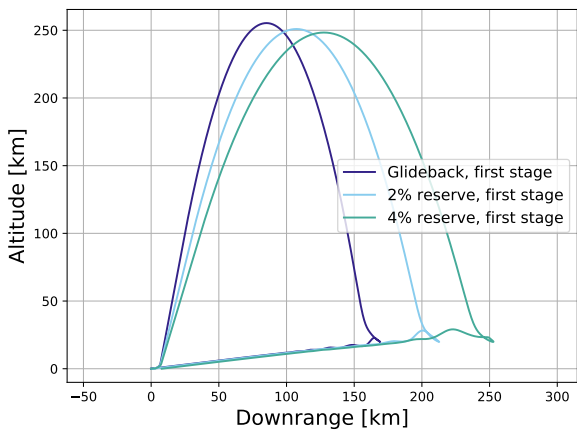


Figure 5.20: Altitude vs. downrange of boostback concept.

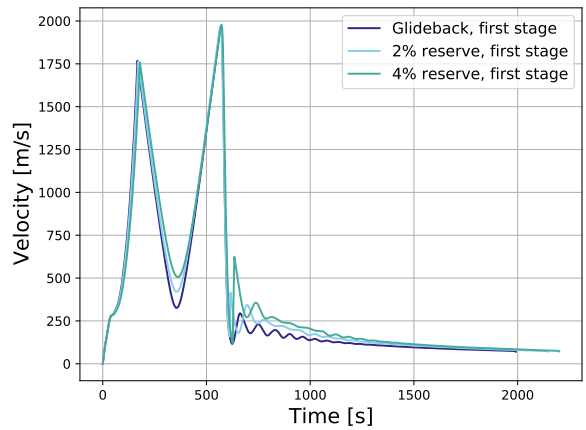


Figure 5.21: Velocity vs. time of first stage vehicle of boostback concept.

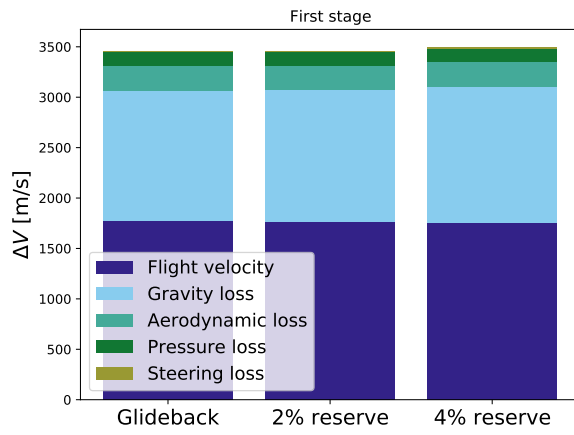


Figure 5.22: First stage Delta-V budget of boostback concept.

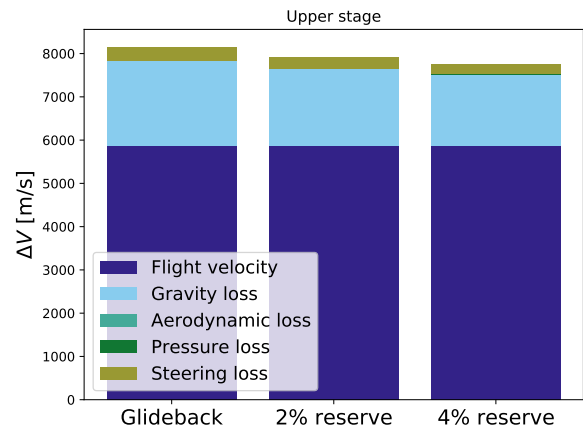


Figure 5.23: Upper stage Delta-V budget of boostback concept.

6

Conclusions and Recommendations

For the conceptual design of the Dawn Aerospace Mk-III concept, a two stage to orbit, winged semi-Reusable Launching Vehicle with horizontal take-off and landing capabilities, an integrated aerodynamic model has been developed. Using this model, sensitivity analyses and case studies have been performed, which form the results of this thesis research. From these results, conclusions were drawn to formulate an answer to the research questions in Section 6.1. Finally, recommendations for further research and development of the integrated aerodynamic model were listed in Section 6.2.

6.1. Conclusions

The conclusions discussed in this section form the answers to the primary research question and the sub-questions. These conclusions were based on the results of the sensitivity analysis and case studies, compared to a baseline design. The changes in performance, resulting from changes to the vehicle or trajectory design, are expressed relative to the baseline design. In establishing the baseline design, also relevant observations were made from which conclusions were drawn.

Primary Research Question: *What is the performance and design impact of wing planform changes to a reusable launch vehicle with horizontal take-off and landing capability?*

In establishing the baseline design of the reusable launching vehicle, it was found that two top-level requirements conflict with each other: the requirement of putting a payload in orbit, by reaching orbital velocity, and the requirement of performing a landing at the same runway as the take-off.

The amount of orbital velocity, or delta-V, delivered to the payload is distributed over the two stages of the system. However, the amount of delta-V delivered by the first stage vehicle is limited by its gliding range. In other words, if the velocity delivered by the first stage vehicle would be increased, the first stage vehicle will not be able to glide back to the take-off and landing runway. As the gliding range essentially sets an upper bound to the first stage delta-V, it also yields a lower bound to the upper stage delta-V, which has consequences to the design of the upper stage vehicle. While ideally the amount of delta-V is equal for all stages, for the baseline design of the Dawn Mk-III concept, the upper stage delivers roughly three quarters of the total flight velocity. The large amount of delta-V to be delivered by the upper stage drives the propellant mass fraction to 91.5%.

In a case study with changed wing design, described in Sec. 5.1, aimed at improving the gliding performance, glide ratio in subsonic conditions was increased from approximately 7.8 to 9.0. This in turn increased the effective gliding range from 170 km to 225 km, and allowed the flight velocity delivered by the upper stage to be decreased by 1.8%.

Furthermore, the improved gliding range resulting from the changed wing design, also decreased the flight path angle at the staging point from 79° to 77°, which reduces the amount delta-V losses due to gravity by 8.9%. This, reduction of delta-V loss, in combination with the reduction of delivered upper stage velocity, resulted in an improvement of the upper stage vehicle propellant mass fraction from 91.5% to 90.3%. The

design of the wing planform thus has an impact on the gliding performance of the first stage vehicle, as well as on the design of the upper stage vehicle.

Sub-Question 1: *What areas in the vehicle design have a significant impact on the mission performance?*

A case study has been performed with an altered fuselage design, discussed in Sec. 5.2, which indicates that also the fuselage design has an impact on the mission performance. The upper stage, which is stored in the fuselage of the first stage vehicle, was packaged in such a way that the fuselage was decreased in length, and increased in diameter.

As expected, the aerodynamic drag of the first stage vehicle was increased due to the changed fuselage design, and resulted in an increase of delta-V loss due to aerodynamic drag by 39.7%. The altered fuselage design also resulted in a lower estimated first stage dry mass by 25%. The reduced dry mass of the first stage has benefits for the return trajectory, as the altitude retained after re-entry was increased from approximately 22 km to 25 km. Without increasing the first stage aircraft's glide ratio, the effective gliding range is increased from 170 km to 210 km. Similar as for the alternative wing design, the increased gliding range reduces the amount of delta-V delivered by the upper stage by 1.2%. It also reduces flight path angle at staging from 79° to 76°, which causes a reduction of the upper stage gravity losses by 2.1%. Ultimately, the changed fuselage design in this case study allowed for a reduced propellant mass fraction from 91.5% to 90.4%.

Sub-Question 2: *How does the trajectory design impact the mission performance?*

As already explained in the answers to the primary research question, the baseline design of the Dawn Mk-III concept features a steep trajectory with a flight path angle at staging of 79°. While this steep flight path angle results in large gravity losses of the upper, it was found that steering of the upper stage trajectory is an effective means to decrease these gravity losses.

A simple angle of attack profile was applied to the upper stage trajectory with first a period of negative angle of attack, followed by a period of positive angle of attack. This profile flattens the upper stage ascent trajectory and because of this the gravity losses experienced by the upper stage are significantly reduced. Although the steering of the upper stage trajectory introduces steering losses of delta-V, greater reductions of gravity losses can be achieved with adequate steering. Results of trajectory simulations of the Dawn Mk-III by Haex [7] already showed a similar angle of attack profile, but the effect of the applied steering on the gravity losses and the mission performance were not understood.

Two case studies were performed to further identify the impact of trajectory design on the mission performance. In the first of these, the first stage trajectory was altered with the take-off performed in negative downrange direction, after which the vehicle pitches over vertically to continue its ascent again in positive downrange direction. The maneuver is further described in Sec. 5.3, and was aimed at reducing the downrange covered in the ascent trajectory, such that a smaller gliding range is required for the return trajectory. Although a small reduction of upper stage propellant mass fraction could be achieved (from 91.5% to 91.0%), the first stage vehicle experiences increased aerodynamic losses by 122%. Because of the increased losses, the propellant mass fraction of the first stage was increased from 68.9% to 72.3%.

The second case study regarding the trajectory design revolved around the application of a boost from the rocket-engines in the return trajectory of the first stage vehicle. For this boost, a portion of the propellant must be reserved. The results of this case study indicates that a 4% reservation of propellant for the return trajectory can increase the gliding range from 170 km to 250 km. This in turn allows the upper stage propellant mass fraction to be reduced from 91.5% to 90.3%, through the mechanisms of reduced upper stage delta-V and reduced staging flight path angle and associated gravity losses.

6.2. Recommendations

During the development of the integrated performance model of the Dawn Mk-III concept interesting areas for further research were identified. Also from the performed sensitivity analyses and case studies recommendations can be formulated, regarding the development of the model or the design of the launching vehicle concept. The recommendations listed in this section are grouped per topic.

Planform design

A sensitivity analysis was performed on the parameters defining the planform, and one case study was done

with an alternative wing concept. However, more designs should be analysed and aimed at improving the subsonic glide ratio, while minimizing the impact on the supersonic drag. Inspiration can be drawn from supersonic transport aircraft, and military aircraft, for which also always a balance is sought between high speed and low speed performance.

The wing planform design is important as it also impacts the structural mass of the first stage vehicle. Also stability and control are influenced by the wing planform design, which was not taken into account in this research, but is still important as also large angles of attack are required during the return trajectory.

First stage trajectory design

The analysed designs of the Dawn Mk-III concept feature steep first stage trajectories, which inherently lead to large gravity losses. In this research, a simple method was employed to model the trajectory. The trajectory can be optimized by designing it such that the sum of the delta-V losses, with in particular the gravity losses, are minimized.

Upper stage trajectory design

It was found that for steep upper stage trajectories, steering can be an effective means to reduce gravity losses. In the developed methodology, the steering was applied using a simple predefined angle of attack profile. Using numerical optimization techniques, this angle of attack profile can be optimized to ensure an upper stage trajectory with minimum gravity and steering losses.

Aerodynamic modelling

In the developed aerodynamic model, uncertainty remains in the supersonic zero-lift drag estimation, and the lift and lift-induced drag estimation at high supersonic and hypersonic conditions. The sensitivity analysis on model uncertainty has indicated what effect these uncertainties have on the simulated trajectories and estimated mission performance. In order to advance the design of the Dawn Mk-III, or similar concepts, more fidelity in the developed analysis model is required and more effort should be done to decrease the uncertainties in the aerodynamic model by either different methodologies, or more elaborate validation efforts.

In addition, during re-entry aerodynamic heating is a significant factor that must be accounted for in the structural design of the wing. In the developed trajectory model, the stagnation point heat flux was only used as a guidance method for the atmospheric re-entry. More effort should be put in the estimation of aerodynamic heating in order to identify how this impacts the vehicle design.

Mass modelling

In the validation process of the mass model, statistical analysis pointed out that there is uncertainty in the estimation of the launching vehicle dry mass. As the sensitivity analysis has pointed out that over- or under-estimation of the dry mass has significant impacts on the simulated trajectory and the mission performance, more certainty in the estimation method is required.

Furthermore, the case study on the alternative fuselage configuration has pointed out that the design offers significant benefits in terms of the fuselage mass. However, no weight penalty was taken into account for the alternative way of packaging the upper stage vehicle in the fuselage, and in future research on the design configuration this should be investigated.

Bibliography

- [1] K. Russell, *Calculating the Economics of Reusable Launch Vehicles*, May 2018. [Online]. Available: <http://interactive.satellitetoday.com/via/may-2018/calculating-the-economics-of-reusable-launch-vehicles/>.
- [2] ISSET Space & STEM, *Simultaneous SpaceX Falcon Heavy Side Booster Landing @ KSC*, Apr. 2020. [Online]. Available: <https://www.youtube.com/watch?v=WLidfyD4eUM>.
- [3] J. Spies and H. Kuczera, "The sub-orbital hopper - One of FESTIP's preferred concepts," in *9th International Space Planes and Hypersonic Systems and Technologies Conference*, 1999. DOI: [10.2514/6.1999-4945](https://doi.org/10.2514/6.1999-4945).
- [4] T. Tsuchiya and T. Mori, "Optimal conceptual design of two-stage reusable rocket vehicles including trajectory optimization," *Journal of Spacecraft and Rockets*, vol. 41, no. 5, 2004, ISSN: 15336794. DOI: [10.2514/1.1082](https://doi.org/10.2514/1.1082).
- [5] C. A. Maddock, L. Ricciardi, M. West, J. West, K. Kontis, S. Rengarajan, D. Evans, A. Milne, and S. McIntyre, "Conceptual design analysis for a two-stage-to-orbit semi-reusable launch system for small satellites," *Acta Astronautica*, vol. 152, Nov. 2018, ISSN: 00945765. DOI: [10.1016/j.actaastro.2018.08.021](https://doi.org/10.1016/j.actaastro.2018.08.021).
- [6] T. Rogoway and J. Trevithick, *The Tragic Tale Of How NASA's X-34 Space Planes Ended Up Rotting In Someone's Backyard*, Feb. 2019. [Online]. Available: <https://www.thedrive.com/the-war-zone/26546/the-tragic-tale-of-how-nasas-x-34-space-planes-ended-up-rotting-in-someones-backyard>.
- [7] T. Haex, *Dawn Aerospace Mk-III An exploration of cost driven mission scenarios of a winged Two Stage to Orbit semi-Reusable Launch Vehicle integrated in the common airspace*. Delft University of Technology, 2020. [Online]. Available: [http://repository.tudelft.nl/..](http://repository.tudelft.nl/)
- [8] B. McBride and S. Gordon, *Chemical Equilibrium with Applications*. [Online]. Available: <https://www1.grc.nasa.gov/research-and-engineering/ceaweb/>.
- [9] B. T. C. Zandbergen, "Simple mass and size estimation relationships of pump fed rocket engines for launch vehicle conceptual design," 6th European Conference For Aeronautics and Space Sciences (EU-CASS), Tech. Rep., 2015. [Online]. Available: <https://www.researchgate.net/publication/279711349>.
- [10] D. Mages, "ESPA User's Guide," Moog Space and Defense Group, Tech. Rep., Nov. 2018.
- [11] D. Akin, *Launch and Entry Vehicle Design: Mass Estimating Relations*, 2016. [Online]. Available: <https://spacecraft.ssl.umd.edu/academics/791S16/791S16L08.MERsx.pdf>.
- [12] F. Castellini, "Multidisciplinary Design Optimization for Expendable Launch Vehicles," Ph.D. dissertation, Politecnico di Milano, 2012.
- [13] G. Sutton and O. Biblarz, *Rocket Propulsion Elements 7th*. 2001.
- [14] H. Schlingloff, *Astronautical Engineering: An introduction to the Technology of Spaceflight*. Ingenieurbüro Dr. Schlingloff Publications, 2005.
- [15] J. Roskam, *Airplane Design V: Component Weight Estimation*. DARcorporation, 1999.
- [16] E. C. Polhamus, "A Concept of the Vortex Life of Sharp-Edge Delta Wings Based on a Leading Edge Suction Analogy," *NATIONAL AERONAUTICS AND SPACE ADMINISTRATION For*, 1966, ISSN: 0027-8424.
- [17] H. Carlson, R. Mack, and R. Barger, "Estimation of Leading-Edge Thrust for Supersonic Wings of Arbitrary Planform," National Aeronautics and Space Administration, Tech. Rep., 1979.
- [18] E. Torenbeek, *Essentials of Supersonic Commercial Aircraft Conceptual Design*. John Wiley & Sons Ltd., 2020. DOI: [10.1002/9781119667063](https://doi.org/10.1002/9781119667063).

- [19] A. M. Abdalla, F. d. C. Baraky, and M. Urzedo Quirino, "Conceptual design analysis of a variable swept half-span wing of a supersonic business jet," *CEAS Aeronautical Journal*, vol. 11, no. 4, Dec. 2020, ISSN: 1869-5582. DOI: [10.1007/s13272-020-00457-8](https://doi.org/10.1007/s13272-020-00457-8).
- [20] D. Cohen and R. T. Jones, *High speed wing theory*. Princeton University Press, 2015. DOI: [10.1515/9781400874941](https://doi.org/10.1515/9781400874941).
- [21] P. Krus and A. Abdallah, "Modelling of Transonic and Supersonic Aerodynamics for Conceptual Design and Flight Simulation," in *Proceedings of the 10th Aerospace Technology Congress, October 8-9, 2019, Stockholm, Sweden*, vol. 162, 2019. DOI: [10.3384/ecp19162003](https://doi.org/10.3384/ecp19162003).
- [22] C. Weiland, *Aerodynamic data of space vehicles*. Springer, 2014, vol. 9783642541681. DOI: [10.1007/978-3-642-54168-1](https://doi.org/10.1007/978-3-642-54168-1).
- [23] NASA Langley Research Center, *X-34 Metallic Model Tested In Langley's UPWT*, Dec. 1997. [Online]. Available: <https://www.dvidshub.net/image/689299/x-34-metallic-model-tested-langleys-upwt>.
- [24] G. C. Rufolo, P. Roncioni, M. Marini, R. Votta, and S. Palazzo, "Experimental and numerical aerodynamic data integration and aerodatabase development for the PRORA-USV-FTB_1 reusable vehicle," *A Collection of Technical Papers - 14th AIAA/AHI International Space Planes and Hypersonic Systems and Technologies Conference*, vol. 2, 2006. DOI: [10.2514/6.2006-8031](https://doi.org/10.2514/6.2006-8031).
- [25] StratoCat, *USV (UNMANNED SPACE VEHICLE) - POLLUCE*, Nov. 2010. [Online]. Available: <http://stratocat.com.ar/fichas-e/2010/TOR-20100411.htm>.
- [26] D. Dirx and E. Mooij, *Conceptual Shape Optimization of Entry Vehicles*. Cham: Springer International Publishing, 2017, ISBN: 978-3-319-46054-3. DOI: [10.1007/978-3-319-46055-0](https://doi.org/10.1007/978-3-319-46055-0).
- [27] G. J. J. Ruijgrok, "Elements of Airplane Performance," *VSSD*, vol. 2, no. 2, 2009.
- [28] J Gerthoffert, V Cerezo, M Bouteldja, and M.-T. Do, "Modeling aircraft braking performance on wet and snow/ice-contaminated runways," *Proceedings of the Institution of Mechanical Engineers, Part J: Journal of Engineering Tribology*, vol. 229, no. 9, Sep. 2015, ISSN: 1350-6501. DOI: [10.1177/1350650115572450](https://doi.org/10.1177/1350650115572450).
- [29] C. Maddock, F. Toso, L. Ricciardi, A. Mogavero, K. H. Lo, S. Rengarajan, K. Kontis, A. Milne, D. Evans, M. West, and S. McIntyre, "Vehicle and Mission Design of a Future Small Payload Launcher," in *21st AIAA International Space Planes and Hypersonics Technologies Conference*, Reston, Virginia: American Institute of Aeronautics and Astronautics, Mar. 2017, ISBN: 978-1-62410-463-3. DOI: [10.2514/6.2017-2224](https://doi.org/10.2514/6.2017-2224).
- [30] W. H. Mason, "Chapter 10: Supersonic Aerodynamics," Virginia Tech Aerospace Engineering, Tech. Rep., 2016.

A

Aerodynamic validation results

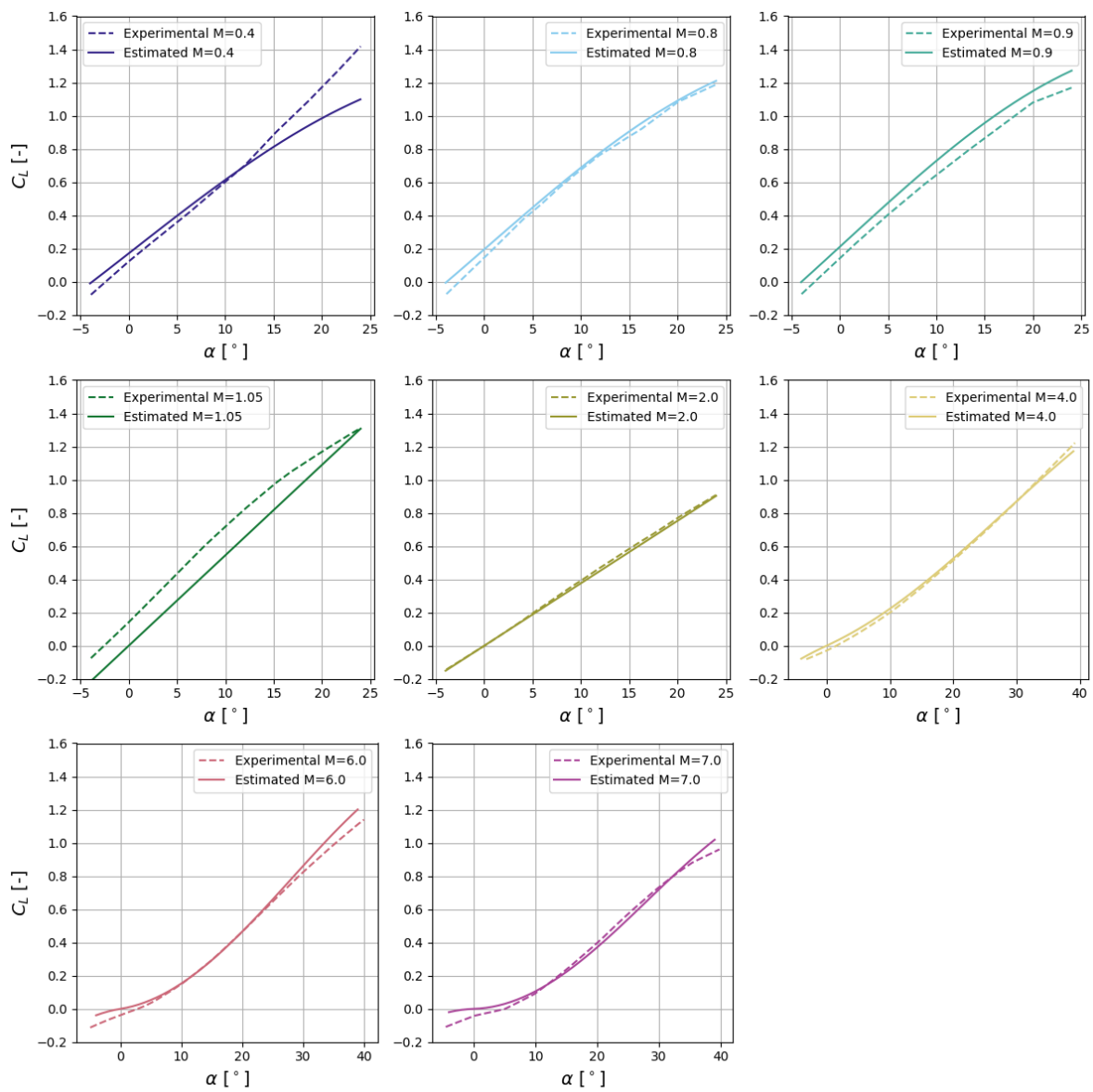


Figure A.1: Aerodynamic model validation results of the Orbital Sciences X-34 lift coefficients.

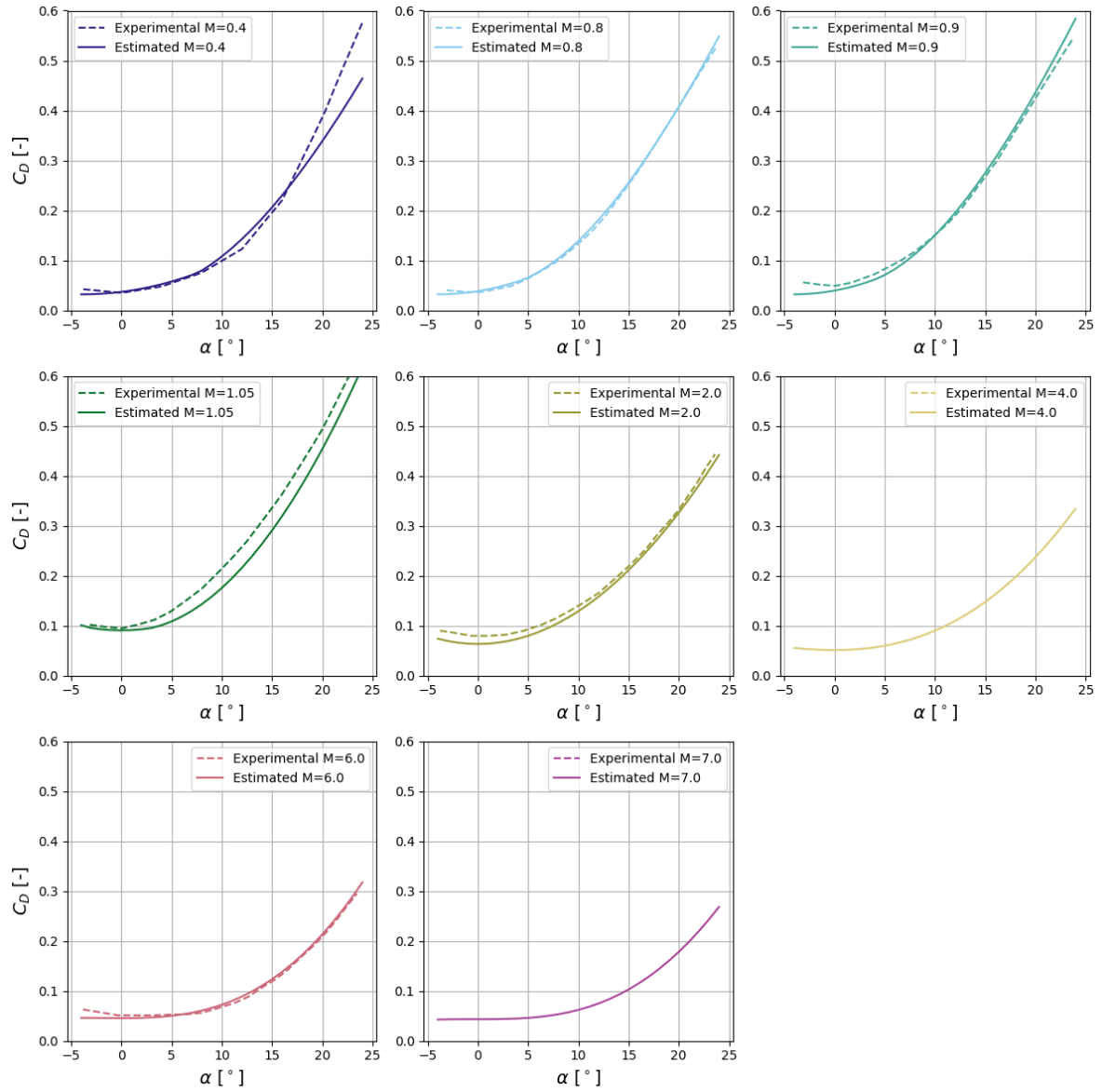


Figure A.2: Aerodynamic model validation results of the Orbital Sciences X-34 drag coefficients.

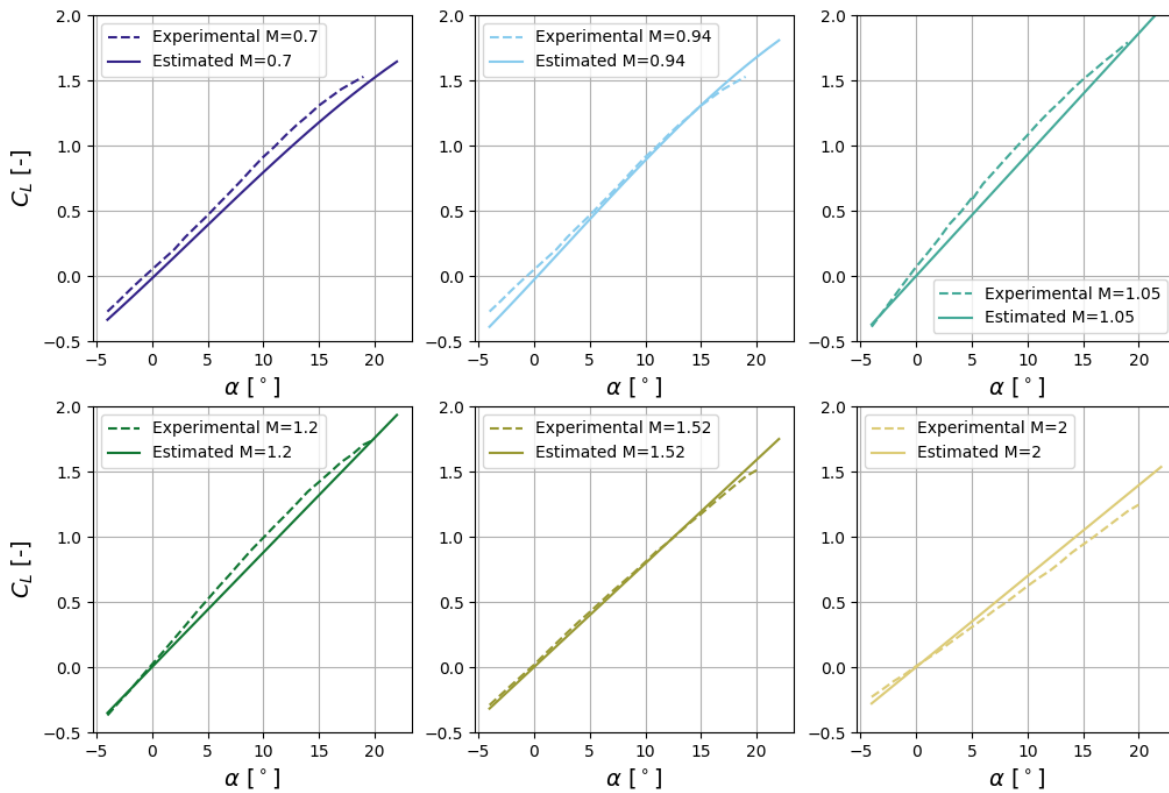


Figure A.3: Aerodynamic model validation results of the PRORA-USV lift coefficients.

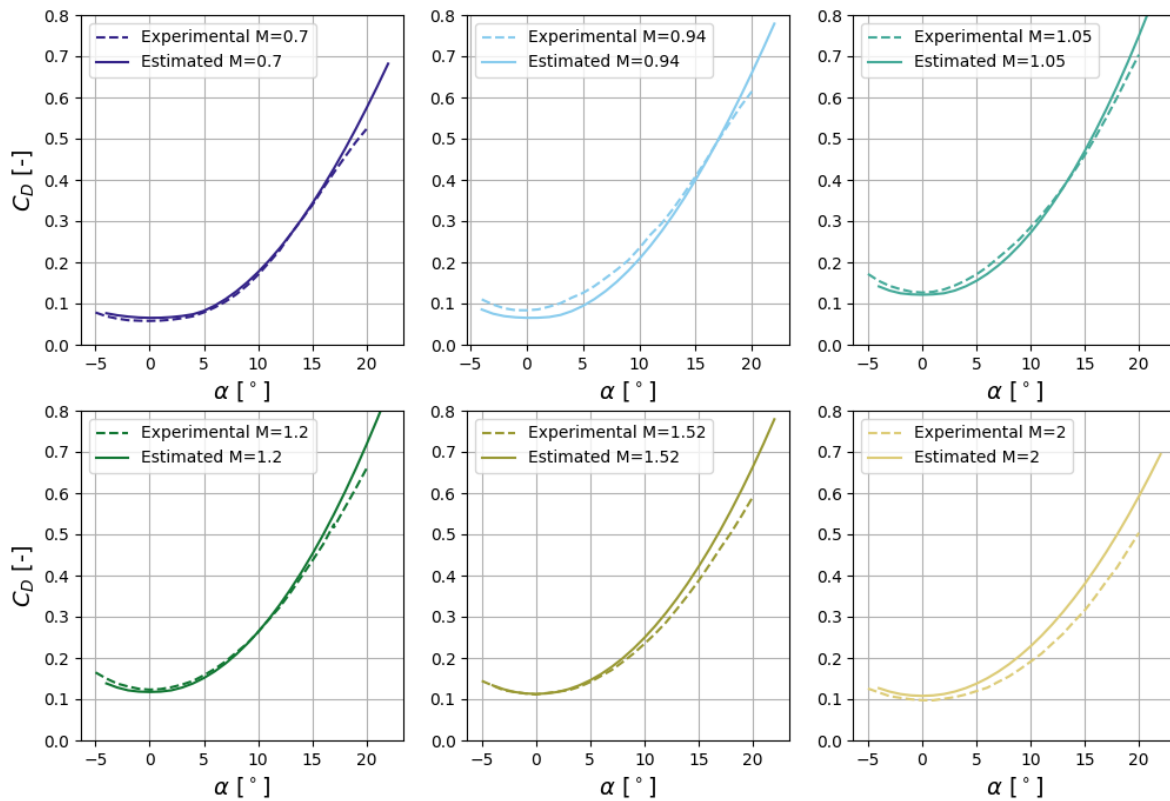


Figure A.4: Aerodynamic model validation results of the PRORA-USV drag coefficients.

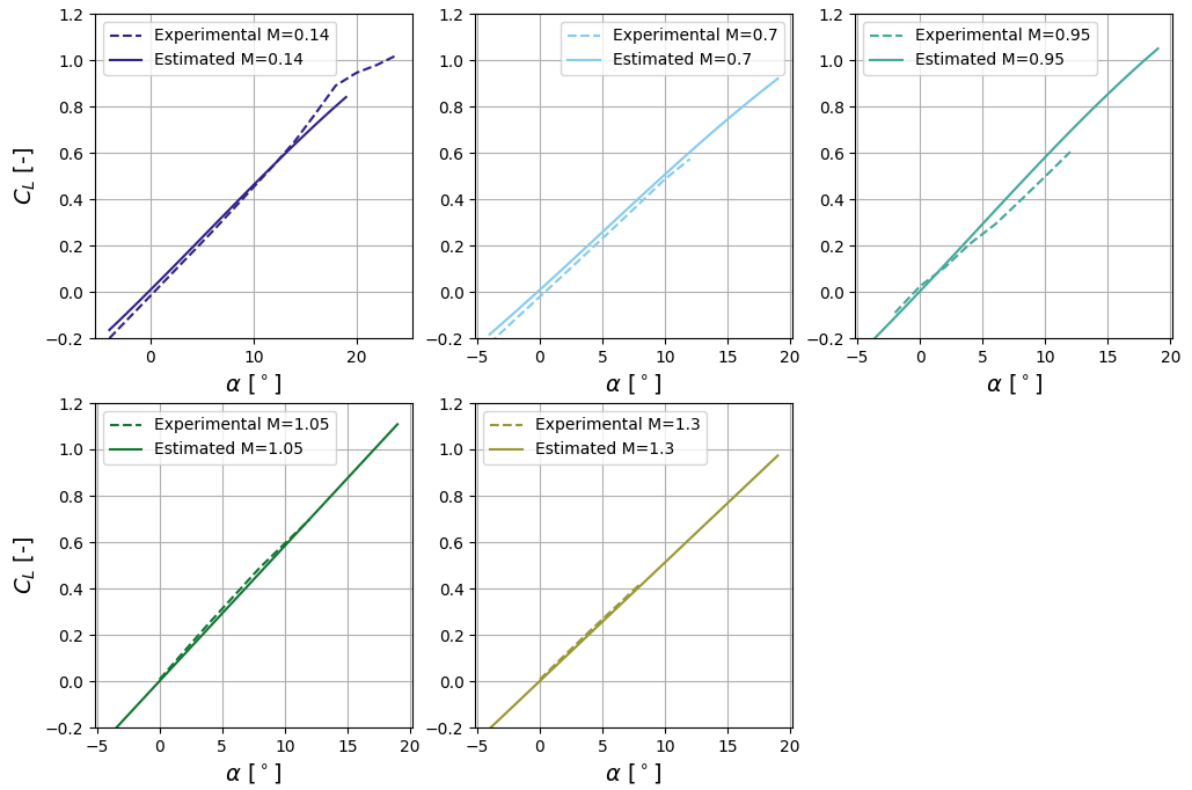


Figure A.5: Aerodynamic model validation results of the Dawn Aerospace Mk-II lift coefficients.

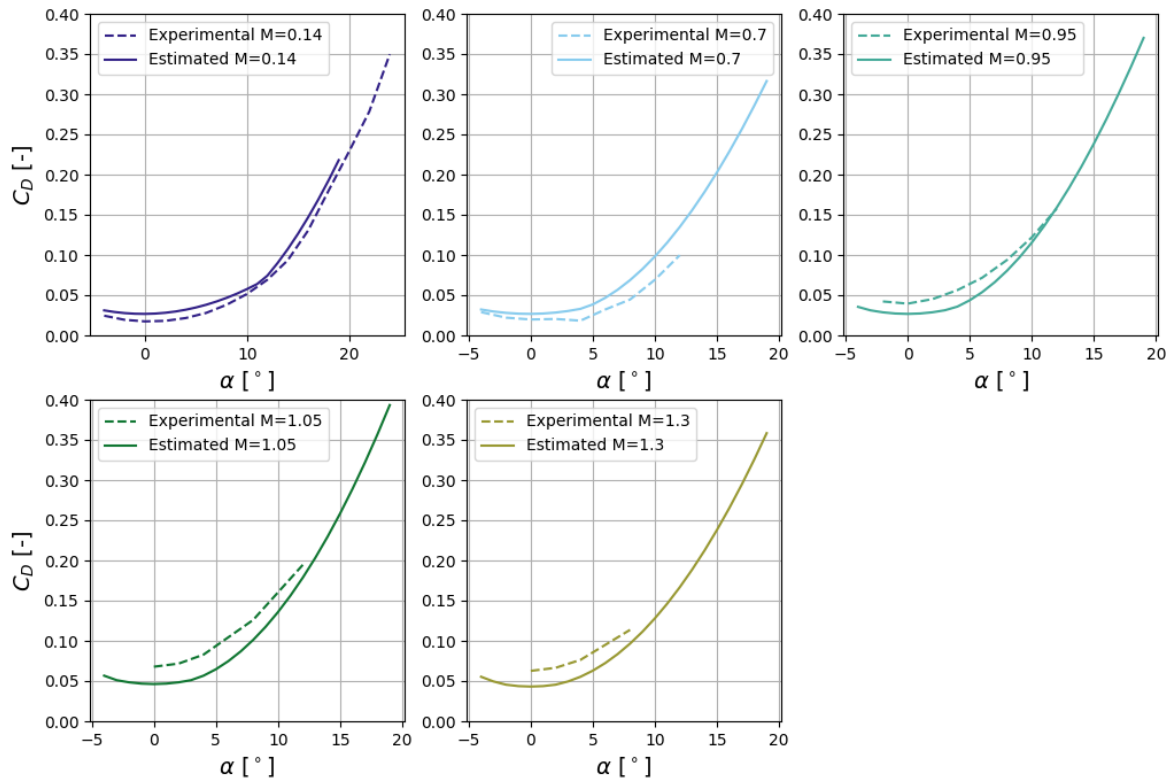


Figure A.6: Aerodynamic model validation results of the Dawn Aerospace Mk-II drag coefficients.